MODELING OF NON-NEWTONIAN BLOOD RHEOLOGY WITH APPLICATIONS TO ARTERIAL FLOW SIMULATIONS

by

Alex J. Apostolidis

A dissertation submitted to the Faculty of the University of Delaware in partial fulfillment of the requirements for the degree of Doctor of Philosophy in Chemical Engineering

Summer 2015

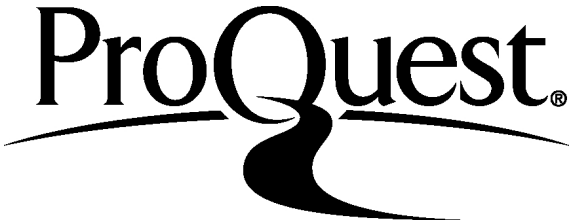

MODELING OF NON-NEWTONIAN BLOOD RHEOLOGY WITH APPLICATIONS TO ARTERIAL FLOW SIMULATIONS

by

Alex J. Apostolidis

Approved: _____

Abraham M. Lenhoff, Ph.D.
Chair of the Department of Chemical and Biomolecular Engineering

Approved: _____

Babatunde A. Ogunnaike, Ph.D.
Dean of the College of Engineering

Approved: _____

James G. Richards, Ph.D.
Vice Provost for Graduate and Professional Education

I certify that I have read this dissertation and that in my opinion it meets the academic and professional standard required by the University as a dissertation for the degree of Doctor of Philosophy.

Signed: _____

Antony N. Beris, Ph.D.
Professor in charge of dissertation

I certify that I have read this dissertation and that in my opinion it meets the academic and professional standard required by the University as a dissertation for the degree of Doctor of Philosophy.

Signed: _____

Babatunde A. Ogunnaike, Ph.D.
Member of dissertation committee

I certify that I have read this dissertation and that in my opinion it meets the academic and professional standard required by the University as a dissertation for the degree of Doctor of Philosophy.

Signed: _____

Eric M. Furst, Ph.D.
Member of dissertation committee

I certify that I have read this dissertation and that in my opinion it meets the academic and professional standard required by the University as a dissertation for the degree of Doctor of Philosophy.

Signed: _____

Arthur W. Etchells, Ph.D.
Member of dissertation committee

I certify that I have read this dissertation and that in my opinion it meets the academic and professional standard required by the University as a dissertation for the degree of Doctor of Philosophy.

Signed: _____

David A. Johnson, Ph.D.
Member of dissertation committee

ACKNOWLEDGMENTS

I would like to express my deepest appreciation to my committee chair Professor, Dr. Antony Beris. It has been a privilege to be supervised by such a knowledgeable, intelligent, and humble person with a strong technical expertise. His guidance has been central to the completion of this dissertation. I am grateful to him for helping me grow as a person, under his guidance, throughout the past four years.

I would also like to thank my committee members, Professor Babatunde Ogunnaike, Professor Eric Furst, Professor Art Etchells, and Dr. David Johnson. Discussing my research with them has helped me gain a better understanding of my work. Special thanks goes to Dr. Johnson who was always available for discussions on the in-house developed blood flow model, which was also used in my work.

In addition, a thank you to my colleagues and friends who have always been there when needed. Thank you Dr. Gou for being such an excellent example to follow. Many thanks to Dr. Armstrong, Paul Mwasame, and Ru Chen. It would have been a lonely office without you.

Finally, I would like to thank my parents, and two elder brothers, for their patience, their support and their encouragement.

TABLE OF CONTENTS

Appendix

LIST OF TABLES

LIST OF FIGURES

ABSTRACT

This thesis aims at improving the accuracy of blood flow simulations by offering a faithful representation of the human blood rheology. A central component of this work has been the establishment of a connection between the physiological conditions in blood and the exhibited rheology. This connection, along with the macroscopic approach which is adopted so as to describe the structural changes within blood that dictate the key rheological properties, namely the viscosity and yield stress, can be a powerful tool in the hands of physicians and medical scientists who might require detailed and reliable information of the exhibited hemodynamics in the arterial network. Thus, this work can be potentially used for the improvement of diagnostic methods in cardiovascular-related diseases.

Throughout this thesis particular emphasis has been placed on adhering to a systematic approach, a practice that is warranted for the modeling of systems as complex, and highly coupled, as the flow of blood in the human arterial network. The first step has been the development of a parametric model for the description of the steady state rheology in simple shear flows. Under physiological conditions, we have shown that the Casson constitutive equation describes best the rheology of blood. The proposed model connects the involved parameters, the Casson viscosity and yield stress, to the physiological conditions, the hematocrit, temperature and fibrinogen concentration. Yield stress has been modeled as critical, percolation type phenomenon with an onset that corresponds to a critical hematocrit. The highlight of this work has been the quantification of the dependence of yield stress, and the critical hematocrit, on the fibrinogen concentration.

Following the development of the parametric Casson model for physiological conditions we extended our analysis to pathological cases, whereby we examined the effect of both high and low values of cholesterol and triglycerides to the steady shear flow properties. We showed that while the Casson model continues to describe well the blood rheology, its model parameters, i.e. the yield stress and model viscosity, need to be significantly modified from their physiological expressions. The new parametrization involves indices, formed from the supplied cholesterol and triglycerides information. Namely, we found that the indices of interest are all ratios: total cholesterol to high density lipoproteins (HDL), low density lipoproteins (LDL) to HDL, and total triglyceride to HDL. While these indices arose naturally in the fitting of the data, they all have been previously identified as important in medical evaluations of CVDs.

Upon completion of the steady state analysis, we focused on the modeling of blood in transient shear flows. We have developed a scalar, structural, parameter thixotropic model capable of describing the transient shear rheology. The thixotropic model introduces only three additional parameters, with a specific physical meaning (a zero shear rate maximum strain, and two kinematic coefficients) and a known order of magnitude. Even more importantly, at steady state the thixotropic model reduces to the parametric Casson for low and moderate shear rates, therefore ensuring the previously emphasized systematic analysis, while at high shear rates it reduces to a Newtonian model, which is consistent with data from literature that have, however, never been predicted theoretically. The thixotropic model has been extensively validated against triangular step-change, rectangular step-change, and large amplitude oscillatory (LAOS) data, and it offers, at a minimum, a reasonable, semi-quantitative fit.

Finally, we have examined the impact of the described rheology on simulations of arterial flow. Namely, we have carried out CFD simulations of blood flow in the left coronary artery (LCA), considering two separate cases: a healthy LCA artery, and a pathological one with a stenosis causing ~82% blockage in the left anterior descending (LAD) branch of the LCA. In this study we further developed a previously proposed methodology for the proper implementation of outflow boundary conditions (OBCs) in simulations of arterial flow, while also applying a numerical analysis technique which accelerated significantly the convergence rate of the proposed scheme. The results were presented via two comparative cases. For the healthy LCA artery, we compared the predictions of a Newtonian-based simulation to those that resulted from the application of the Casson parametric model. The obtained pressure and flow profiles, as well as the wall shear stress (WSS), which is the most important parameter in CVD related hematological studies, were shown to be significantly different in the two cases. This highlights the importance of incorporating the rheology of blood in CFD simulations. Then, for the pathological geometry we compared the results obtained with and without the application of the proposed scheme for the proper implementation of OBCs. Again, the marked differences in the simulation output in the two cases highlights the need for adopting the proposed methodology in arterial flow simulations.

Chapter 1

INTRODUCTION

1.1 Motivation

Cardiovascular diseases (CVDs) are the leading cause of death in the US, and contribute more than three hundred billion dollars annually to the national health care cost (American Heart Association 2014). This explains the enormous interest and number of research activities centered today on the investigation of blood flows, as can be inferred from the many books that have been dedicated partly or fully to this subject (Pedley 1980; Cheer and van Dam 1993; Fung 1997; Nichols and O'Rourke 1998; Drzewiecki and Li 1998; Li 2000; 2004; Zamir, 2000; 2005; Waite and Fine 2007; Batzel *et al.* 2007; Galdi *et al.* 2008; Truskey *et al.* 2009; Formaggia *et al.* 2009; Chandran *et al.* 2012; Peattie *et al.* 2013).

Atherosclerosis, the most typical precursor of CVDs, can be seen as a flow problem developing in the closed network flow field of the cardiovascular system. A fluid mechanics analysis of the flow can potentially improve the understanding of the mechanisms under which these pathologies develop. A case in point is the investigation of Malek et al. (1999) which showed that low and oscillatory shear regions (below 0.4 Pa) can favor the development of atherogenesis, the initial stage of atherosclerosis. From this work and various others [Ku et al. (1985); Levesque et al (1986); Nemerson and Turrito (1991); Ku (1997); Wooten and Ku (1999); Younis et al. (2004)] there has been a consistent trend of atherosclerosis being associated with local fluid dynamics

inside the vessels. A popular means of obtaining detailed information about the flow is computational fluid mechanics (CFD).

1.2 Background

CFD has been increasingly used for modeling blood flow in arteries and has gained favor as a tool for understanding and predicting CVDs. Three-dimensional (3D) simulations have been performed on various vascular regions, ranging from the carotid [Rindt and van Steehoven (1996); Milner et al. (1998), Gijsen *et al.* (1999a); Steinman *et al.* (2002); Kato *et al.* (2003); Valencia *et al.* (2006); Nguyen *et al.* 2008; Gay and Zhang 2009; Wake *et al.* (2009); Bevan *et al.* (2010); Morbiducci *et al.* (2011); Kamenskiy *et al.* (2012)], to the coronary (Hutchins *et al.* (1976); Nissen *et al.* (1991); Brinkman *et al.* (1994); Friedman *et al.* (1996); Perktold *et al.* (1998); Changizi and Cherniak (2000); Seron *et al.* (2003); Ramaswamy *et al.* (2004); Frauenfelder *et al.* (2007); Johnson *et al.* (2011a); Apostolidis *et al.* (2014)], the abdominal aorta [Taylor *et al.* (1998); Trushar *et al.* (2011)], the cerebral [Moore *et al.* (2006); Alastruey *et al.* (2007); Alastruey *et al.* (2008); Passerini *et al.* (2009); Reymond *et al.* (2012); Fahy *et al*. (2014)], and the pulmonary [Spilker *et al.* (2007); Clipp and Steele (2009)] arteries to name a few. However, despite the significant number of cardiovascular-related CFD investigations, the clinical impact of these studies on the medical field is limited, as the physiological relevance of hematological data acquired from simulations can be questionable [Byoung-Kwon (2011)].

The limiting factors that decide the accuracy of blood flow simulations are the precision of the geometrical model, the complexity of fluids in the human body, and the imposed boundary conditions (BCs). State-of-the-art technologies have offered

significant improvements in overcoming some of these limitations. Medical imaging techniques, such as computed tomography, ultrasound imaging, and magnetic resonance imaging offer very detailed, personalized geometrical models that are used for CFD simulations. Therefore, the geometric representation of vascular components no longer constitutes a significant limitation in simulations of arterial flow. The same cannot be claimed for the remaining limiting factors, the fluid complexity and the boundary conditions.

Being a dense suspension of cells in plasma, blood exhibits a complex non-Newtonian rheology. It has a shear thinning and viscoplastic behavior (exhibits a yield stress), while its deformation dependence on the history of the flow means it is also thixotropic. The rheology of blood is often neglected, or at best severely simplified, in simulations of arterial flow. Characteristically, non-Newtonian blood rheology effects are at best approximated through generalized Newtonian models (Gijsen *et al.* 1999a; 1999b; Valencia *et al.* 2006; Lee and Steinman 2007; Yilmaz and Gundogdu 2008; Wang *et al.* 2010; Morbiducci *et al.* 2011; Seo 2013). However, as we know from theory (Bird *et al.* 1987), and given the history-dependence of blood rheology (Bureau *et al.* 1980), such a description is only valid for steady shear flows which are fundamentally different from the pulsatile, Poiseuille type of flows occurring in the human body. Most importantly, even when a phenomenological generalized Newtonian model is employed to represent the most important non-Newtonian characteristic of blood, namely the shear-thinning property, the model parameter values are not directly connected to the physiological conditions. This limits significantly the application of blood flow simulations; in order to incorporate the rheology of blood, one would be required to obtain rheological measurements of the respective blood sample.

Another issue associated with capturing the *in vivo* nature of the fluid dynamics comes from the specification of appropriate boundary conditions. These conditions need to be specified for every computational domain of the system, which includes the arterial vessel walls and the inlet(s)/outlet(s). For the first type of BCs, those corresponding to the vessel wall, the most typical approach, and the one that is also adopted in our investigation, is to apply the no-slip and no-penetration conditions. However, for a more faithful representation of the *in vivo* conditions, the mechanical properties of the arterial wall would have to be taken into consideration. This requires the application of fluid-structure interaction (FSI) modeling, in order to account for the impact of the vessel compliance on the arterial pressure and/or the pressure wave propagation [Campo-Deaño *et al*. (2015); Dong *et al*. (2015)]. However, the inclusion of FSI adds significant complexity, and therefore increased computational demands, to the problem of blood flow modeling. While the importance of FSI is recognized, the focus of this project, as will be further discussed in the current section, is on improving the rheological description of blood flow.

The proper specification of the outflow boundary conditions is an equally complicated task. The complexity rises due to the closed network condition that characterizes the arterial system, which dictates that the outflow BCs in simulations of flow in specific vascular components (such as the coronary artery) should represent information of the downstream network, which extends beyond the limits of the simulated geometry. Similarly to the case of the vessel wall BC, the various methodologies that are employed here involve different levels of accuracy.

One of the sensible ways that have been followed to address this issue involves the use of existing, non-invasive technologies, such as the Doppler ultrasound and the

3D MRI that can provide pressure and velocity profiles (Milner *et al.* 1998; Xu *et al.* 1999; Frauenfelder *et al.* 2007; Boutsianis *et al.* 2008; Torii *et al.* 2009; Wake *et al.* 2009). These are very accurate and detailed data, but, in addition to requiring the use of expensive and time-consuming techniques, they can only be used to reproduce the existing flow. In other words, such techniques cannot be utilized for modeling practices or to examine what-if scenarios.

The most widely used type of outflow boundary conditions in arterial flow simulations is the zero pressure outlet BC [Galindo-Rosales *et al*. (2014)]. This type of conditions are not suitable for hematological studies, as they neglect any changes in the pressure and flow rate as a consequence of the influence of the downstream vessels. Moreover, their application can only be justified in symmetric geometrical models, which constitute a strongly idealized representation of vessels. Another type of BCs typically employed in blood flow simulations is the resistance BC [Vignon- Vignon and Taylor (2004); Figueroa *et al*. (2006); Clementel *et al*. (2006)]. This methodology considers a linear relationship between flow rate and pressure at the outlets, and it is equivalent to imposing a constant pressure gradient across the downstream network. The resistance BCs cannot describe *in vivo* conditions either, as they are very approximate and they can only be applied to steady flow conditions.

More sophisticated methodologies for the description of the outflow conditions have also been employed. These methods typically involve the description of outlet conditions through a correlation between outlet flow and pressure, as opposed to assigning absolute values to a computational outlet domain. This is based on information of the arterial network dynamics, which extend beyond the limits of the simulated geometry. Such information is obtained from more generic 0D or 1D network

models which, unlike the 3D simulations, can cover an extended part of the arterial network. Since this approach involves the passing of information from the more approximate, but also generic, 0D or 1D models to the more detailed, but also computationally expensive, 3D simulations, the methodology can be described as hybrid. The various hybrid models that have been proposed are mainly distinguished from the complexity of the developed network model.

The more simplistic cases of network models regard the use of lumped parameter models, the most common of which is the three-element Windkessel model [Taylor and Draney (2004); Grinberg and Karniadakis (2008)]. These models try to truncate the subnetwork resistance and pressure/flow relationships by using a lumped (0D) and regressed parameter set, which in consequence may be limited in its predictive capability, and by necessity involves parameters lacking a physiological meaning. The more rigorous approaches aim at matching the outflow BCs of 3D simulations to the predictions of 1D impedance models of the whole arterial network [Quarteroni and Veneziani (2003); Formaggia *et al*. (2009); Bernabeu *et al*. (2013)]. These models approximate the arterial network as a 1D treelike structure with linearized flow equations that can be solved analytically, and incorporate time-periodicity of the flow. Such a network model has been previously developed within our group [Johnson et al. (2011b)] and it is used for the scope of the present work.

The developed impedance model covers the entire arterial network, from the aorta all the way down to the smallest capillary level. Furthermore, it solves for the time-periodic pulsatile flow profile as a combination of a steady state solution, which is obtained through a lubrication-type approximation for flow through tapered tubes, and a linear superposition of principal and higher harmonic modes, which are obtained

through a Womersley-type linear approximation of viscous pulsatile flow within thin-walled elastic vessels [Johnson et al. (2011b)]. However, while the developed network model has been effective in capturing the extended vasculature of the human body, it has only accommodated a very basic and outdated description of the non-Newtonian rheology, limited only to the steady flow component of the model. In order to closely imitate the in vivo outflow conditions in blood flow simulations, a faithful description of the non-Newtonian characteristics of blood needs to be implemented in the network model.

The use of hybrid models to describe the cardiovascular dynamics of blood flow highlights, implicitly, the importance of accounting for the rheology of blood. On one hand, as described earlier in the text, there are efforts to account for the rheology of the fluid in CFD simulations, even with a simplistic way of introducing generalized Newtonian models which cannot predict the history-dependent effects. On the other hand, a faithful rheological description needs to be included in the 1D network model to ensure realistic output of *in vivo* conditions that can be used as BCs in the CFD simulations. Thus, an explanation of the non-Newtonian phenomena in the blood circulation is warranted.

The complex rheology of blood is attributed to its constituents. The red blood cells (RBCs), which greatly outnumber the rest of the suspended in plasma cells (leucocytes and platelets), form aggregate structures (rouleaux) by connecting to each other via the bridging of plasma proteins, such as the fibrinogen [Merrill (1969)]. These structures develop further into a network at very low shear rates, which explains the yield stress characteristic, while at higher shear rates the rouleaux disintegrate, explaining the shear-thinning properties of blood. The thixotropy and viscoelasticity

exhibited by blood are attributed to the elasticity of the formed structures, as well as the elasticity exhibited by the individual RBCs [Merrill (1969); Merrill et al. (1963, 1967, 1965); Apostolidis and Beris (2014, 2015)].

The complex rheology of blood can be exhibited at different parts of the circulation system, and under a variety of conditions. The non-Newtonian properties are primarily manifested at low shear rates (~ 0.01-50 sec^{-1}). This has lead researchers to ignore the rheology of blood in simulations of flow in large arteries, where the shear rates are typically high, by assuming a Newtonian behavior of blood [Sochi (2014)]. Although this assumption is justified to an extent, as indeed the low shear regions are primarily met at the smallest vessels such as the arterioles and the capillaries, such flow conditions can also develop even in large arteries, as, for instance, near bifurcation junctions or, for pathological cases, near aneurysms or close to the stenosis sites (occluded regions) of the diseased artery. In addition, a factor that further perplexes the understanding of flow deformation in the circulatory system, and therefore any attempt to model the respective phenomena based on first principles, is the reported sensitivity of the rheology on pathological conditions invoked from abnormal levels of plasma proteins, such as hypefibrinogenemia, anemia, polycythemia, hyperlipemia and others [Merrill (1969)].

The complex rheology of blood, coupled with the numerous, in most cases unidentified, interactions between the plasma proteins and the suspended cells, suggest a problem of such complexity that the accurate modeling of the system, based on first principles, becomes an immense challenge. Although several efforts have been made to reconstruct the blood flow non-Newtonian characteristics from first principles micromechanical models [Fedosov *et al*. (2010; 2011; 2014); Li *et al*. 2014], the issue

remains that, due to so far poorly understood biological interactions between its ingredients, this full a-priori construction remains elusive and adjustable parameters are needed to describe the red blood cell behavior. Thus, it is our perspective that an alternative approach should be adopted in order to improve the status quo of blood flow modeling, in CFD.

1.3 Objectives

The objective of this work is to improve the quality of blood flow simulations by offering a better representation of the involved rheology. A more faithful description of the involved hemodynamics in the arterial network can improve the accuracy of blood flow simulations and get us closer to physiologically accurate results. Most importantly, however, it is the objective of improving the connection of the rheology models to blood physiology that we want to achieve. A side benefit, potentially of high significance to the medical field, is the use of blood rheology as a tool to improve diagnostic capabilities. Furthermore, by adopting a macroscopic approach, whereby we capture phenomenologically the structural changes within blood that dictate the rheological response, we ensure that the computational demands for incorporating these models into CFD are moderate. This facilitates the end goal of a rheology-based diagnosis being adopted by physicians, as it would constitute an affordable means of establishing a connection between the in vivo measurements at the physician's office and, through the connection of rheology to physiology, the medical diagnosis. A final objective of this thesis is therefore to show the influence of rheology in actual CFD blood flow simulations in selected arterial vessels, which presupposes the fine-tuning, further development and implementation of the appropriate outlet boundary conditions.

1.4 Thesis Outline

The rest of the dissertation is organized as follows: in Chapter 2 we focus on the steady state shear flows, and we develop a parametric model that can describe the rheology of physiological blood under such conditions. Then, in Chapter 3 we try to model the impact of specific pathological conditions, namely the effect of high and low cholesterol and triglyceride levels, on the key rheological properties. Chapter 4 regards the extension of the parametric steady state model to a thixotropic model, which can be used to describe the rheology of blood in transient shear conditions. Finally, in Chapter 5 we undertake a CFD investigation, whereby we simulate the flow of blood in the left coronary artery, and we emphasize the impact of the non-Newtonian rheology on the simulation output. The conclusions of this work and the future directions of it are discussed in Chapter 6.

Chapter 2

MODELING OF BLOOD RHEOLOGY IN STEADY-STATE SHEAR FLOWS

2.1 Introduction

Blood is a complex fluid with non-Newtonian characteristics. It has a shear-thinning behavior [Merrill (1969)] and often exhibits a yield stress (viscoplasticity) [Cokelet *et al*. (1963); Merrill *et al*. (1966, 1969)] with potential history effects (thixotropy) [Dintenfass (1962)]. The rheological complexity of blood is attributed to its constituents. Rheologically, blood is primarily characterized as a concentrated suspension of elastic, deformable, red blood cells (RBCs). However, it also contains other ingredients such as leukocytes and platelets within plasma. Plasma itself contains proteins, of which fibrinogen is known to affect the rheological properties of blood by promoting the aggregation of RBCs at low shear rates [Merrill (1963b, 1966, 1969); Morris *et al*. (1989)]. This complexity makes the modeling of blood rheology from first principles very challenging.

Despite the tremendous amount of efforts in blood flow simulations [Shi *et al*. (2011)], a prominent drawback is in the description of the non-Newtonian rheology. In many simulations it is neglected outright and blood is treated as a Newtonian fluid [Olufsen *et al*. (2000); Cebral *et al*. (2002); Lee and Xu (2002); Tang *et al*. (2003)], while in others it is simplistically represented by accounting only for the shear-thinning behavior [Gijsen *et al*. (1999); Jung and Hassanein (2008)]. In the recent review, Yilmaz and Gundogdu (2008) present an extended list of generalized Newtonian and non-Newtonian macroscopic models that have been used to describe blood flow. On the other hand, considerable efforts have been placed to use detailed microscopic mechanical models [Tanaka and Takano (2005); Fedosov *et al*. (2011)], or even multi-

scale approaches [Fedosov *et al*. (2010)], for better capturing the blood rheology. However, the resulting models (a) require a substantial time to run even for simple flow cases and (b) still fail to incorporate all relevant physics, such as the role of fibrinogen.

The pulsatile flow conditions that are met in the human vascular network necessitate a blood flow model capable of representing time-dependent flows. Such a model should predict both the viscoplastic and the thixotropic properties of blood. Some of the most sophisticated, non-Newtonian, blood flow models in literature able to show (at least implicitly) thixotropy and viscoelasticity were developed by Owens and co-workers [Owens (2006); Moyers-Gonzalez *et al*. (2008)]. In the first of these models [Owens (2006)] an attempt was made to take into account, through a set of viscoelastic phenomenological equations extracted from a polymer network theory analog, the aggregation and disaggregation of the erythrocytes. Moyers-Gonzalez *et al.*(2008) developed a further refinement of that model to account for the inhomogeneous erythrocyte concentrations in the blood stream. However, these models fail to account explicitly for yield stress and viscoplasticity.

Yield stress is an important characteristic of blood rheology and an essential component of its non-Newtonian nature. Experimental evidence for its association with blood has been provided in many investigations [Cokelet *et al*. (1963); Merrill *et al*. (1963, 1965, 1966, 1967, 1969); Chien *et al*. (1966)] and with different experimental techniques, as described by Picard *et al*. (1998). From a modeling point of view, the role of yield stress is most clearly evaluated under steady-state shear flow conditions. This is where we focus our attention in the present work. Furthermore, due to the steady-state restriction, we investigate here viscoplastic models with no time-dependent

(i.e. thixotropic or viscoelastic) characteristics. These features can be added and be separately addressed in a future publication.

The importance of the steady-state models should not be underestimated. Steady-state flows give an insight on essential characteristics of the non-Newtonian rheology, such as shear thinning and yield stress. These need, at a minimum, to be captured in models before departing into a more detailed analysis of time-dependent, thixotropic, effects. Furthermore, an approximate, yet efficient, treatment of blood flow in the arterial network involves decomposing the solution into a steady and a zero mean-flow oscillatory component, each one of which is treated separately [Johnson *et al*. (2011)]. Finally, a trustworthy parametric representation of steady-state blood rheology in terms of physiological parameters may be used as a mean of medical diagnosis. Pathological issues can be inferred from observed differences between viscometric blood data and the predicted model results for physiological conditions [Marcinkowska-Gapińska *et al*. (2007)].

A plethora of models have been used for steady-state blood flow predictions in the literature---see [Marcinkowska-Gapińska *et al*. (2007); Yilmaz and Gundogdu (2008)] and references therein. Although, at times, the preference seems to be in one or two of those models, still there appears to be no consensus. Part of the underlying reasons for this state of affairs may be that some of the proposed models have not been extensively compared to experimental data. In other cases, ambiguities may arise due to incomplete characterization of the data samples used. Moreover, on occasion, the pseudo-shear rate defining Poiseuille flow is confused with the actual shear rate in simple shear.

Due to the simplicity of the steady-state shear flow, the most general equation for the shear stress is of the form of a generalized Newtonian model:

$$\tau = \eta\left(|\dot{\gamma}|\right)\dot{\gamma}, \tag{2.1}$$

where the shear stress, τ, is described in terms of a positive (apparent) viscosity, η, that depends only on the magnitude of the local shear rate, $\dot{\gamma}$. As such, such an equation can also be used to describe the steady-state blood rheology. However, inherent to that description is the assumption that the rheology in a steady-state non-homogeneous shear flow, only depends on the local flow kinematics. This is called the simple fluid hypothesis [Bird *et al*. (1977)]. If and only if this question is first answered affirmatively can one proceed to the next step, i.e. determining the particular generalized Newtonian model that best suits the experimental evidence.

As a special case of a generalized Newtonian fluid, but also as one that further extends it to allow for a singular apparent zero-shear-rate viscosity, it is important to recognize here viscoplastic generalized Newtonian fluid models. In general, viscoplasticity defines a rheological behavior that is characterized by the yield stress, τ_y. This represents the minimum magnitude of the extra stress needed in order for the material to deform continuously under flow. Therefore, for shear flows, the most general viscoplastic description for the shear stress is slightly different than that corresponding to a generalized Newtonian model, Eq. (2.1), in that it explicitly only applies to the yielded state. In shear flows it is implicitly described as:

$$\dot{\gamma} = \begin{cases} \dfrac{\tau + \tau_y}{\eta_y\left(|\dot{\gamma}|\right)} & \tau < -\tau_y \\ 0 & |\tau| \le \tau_y \\ \dfrac{\tau - \tau_y}{\eta_y\left(|\dot{\gamma}|\right)} & \tau > \tau_y \end{cases}, \tag{2.2}$$

where η_y is the "post-yield" viscosity, a positive (finite) function of the local magnitude of the shear rate, $\dot{\gamma}$. Note that although Eq. (2.2) can be cast as a particular case of Eq. (2.1), the corresponding form of the (apparent) viscosity, η, given as:

$$\eta = \frac{\tau_y}{|\dot{\gamma}|} + \eta_y\left(|\dot{\gamma}|\right), \tag{2.3}$$

is singular and becomes unbounded in the limit $\dot{\gamma} \to 0$.

The question of whether a real material exhibits a true yield stress, as described by Eq. (2.2) above, or it is only "apparent" and an idealization valid for small but not infinitesimally small values of the magnitude of the shear rate has sparked a lot of discussion [Barnes (1999)]. However, in many practical applications this may be of little significance to the flow predictions. We believe that the explicit reference to a yield stress, if it is substantiated by experiments over a significant range of shear-rate values, is very useful to have. Not only it simplifies the resulting model equations [for instance η_y appearing in Eqs. (2.2) and (2.3) is, in general, much simpler than the apparent viscosity appearing in Eqs. (2.1) and (2.3)] but also it can be critical in certain problems where yield stress matters, i.e. where unyielded regions may be involved, like low stress stagnation regions. Moreover, the yield stress may be more easily connected

to physiological parameters. For blood, there is overwhelming evidence for the existence of yield stress [Cokelet *et al*. (1963); Merrill *et al*. (1963b, 1965, 1966, 1967, 1969); Meiselman *et al*. (1967); Morris *et al*. (1989); Picart *et al*. (1998); Yeow *et al*. (2002); Lee *et al*. (2011)].

A phenomenological viscoplastic model commonly used in the steady-state analysis of blood flow is the Casson constitutive equation [Casson (1959)]. This non-linear model has been found to accurately predict the flow curves of pigment suspensions used for preparation of printing inks [Casson (1959)] and silicon suspensions [Walwander *et al*. (1975)]. Its applicability to blood is strongly supported by the good comparison with experimental data of varying hematocrits [Merrill *et al*. (1965, 1967, 1963a)], anticoagulants [Meiselman *et al*. (1967)] and temperatures [Merrill *et al*. (1963a)]. However, so far, the Casson model has not been systematically compared against other equations, commonly used to describe the steady-state shear rheology of viscoplastic fluids, such as the Herschel-Bulkley model [Herschel and Bulkley (1926)].

In addition, of interest to numerical simulations is the capability to connect the model parameters (i.e. the viscosity and yield stress of the Casson model) to the physiological conditions. Some parametric representations for the viscosity already exist in the literature but they address the dependence of the apparent viscosity [Pries *et al*. (1990, 1992)], not the Casson viscosity, on the hematocrit (Hct). On the other hand, the dependence of yield stress on the physiological parameters has been the focus of many studies [Chien *et al*. (1966); Picart *et al*. (1998); Yeow *et al*. (2002); Lee *et al*. (2011)]. However, most of the proposed equations in those studies quantify the dependence of yield stress only on the hematocrit. Furthermore, in their formulations,

they do not take advantage of the percolation nature of the yield stress [Merrill (1969)]. Merrill *et al*. (1965, 1969) reported a critical hematocrit value below which blood does not exhibit a yield stress. He was also one of the first researchers to systematically measure the exhibited yield stress under various fibrinogen concentrations [Merrill *et al*. (1966, 1969)], proposing a quadratic dependence on the fibrinogen concentration in plasma [Merrill *et al*. (1969)]. His fibrinogen studies, however, were conducted only at a single hematocrit (40%). Morris *et al*. (1989) also tried to quantify this dependence for a wider range of fibrinogen concentrations and at various hematocrit levels. His experimental data were in reasonable agreement to those of Merrill, at least for those involving RBCs suspension in plasma (as opposed to saline solutions inhibiting red blood cell aggregation). Morris's data further suggested a correlation between the critical hematocrit value and the plasma fibrinogen concentration. However, this effect was not quantified.

Another issue pertaining to the correct use of experimental data is the type of suspending phase under study. Red cell suspensions in plasma display a higher viscosity compared to saline suspensions [Brooks *et al*. (1970); Zydney *et al*. (1991)]. In the case of yield stress, important differences are exhibited between saline suspensions with added fibrinogen [Merrill *et al*. (1966)] and plasma suspensions [Merrill *et al*. (1969)]. Morris *et al*. (1989) have postulated that factor VIII related antigen, immunoglobulins, and fibronectin, all of which are plasma constituents that promote cell-cell adhesion, could potentially affect the interaction of fibrinogen with the RBC membrane and thus the yield stress.

Various studies have shown pathologies, along with the drugs that are used to cure the diseases, to have an impact on the rheology of blood. Picart *et al*. (1999) have

identified the ratio of albumin to globulins as the best predictor of yield stress for patients with systemic sclerosis. Marcinkowska-Gapińska *et al*. (2007) have shown changes in blood rheology, caused by acenocoumarol delivered to post-infarction patients, that they attributed to changes in RBC deformability and rouleaux formation. Weng *et al*. (1996) have examined the impact of macromolecules, other than fibrinogen, on erythrocyte aggregation and explained the pathological significance of concentrations of acute phase proteins. They have also reported that RBCs are likely to be deformed and form compact clumps instead of rouleaux at high hematoctit values. Finally, there lies the value of a very interesting line of investigations where the use of pertinent information, such as the sickle cell shape and elasticity, in suitably established microscopic flow simulations, can lead to specific predictions for blood flow behavior under these specific pathological conditions [Lei and Karniadakis (2012)]. These studies show that as we depart from physiological to pathological states the steady state shear rheology of blood is also affected. Thus, a complete description of the steady state, simple shear rheology could be used for potential diagnostic applications.

The objective of this work is to systematically study and macroscopically (at the continuum level) model the behavior of physiological human blood, as a rheological fluid, in steady-state shear flow. Using the most pertinent experimental data from the literature [Merrill *et al*. (1965); Morris *et al*. (1989); Barbee (1971); Barbee and Cokelet (1971)], the non-Newtonian characteristics of physiological human blood under steady-state flow conditions are evaluated. First, we test the simple fluid hypothesis for blood. In particular, we examine whether blood can be described by the same generalized Newtonian equation in all types of steady-shear flows, homogeneous (e.g. simple shear) as well as non-homogeneous (e.g. Poiseuille flow). Second, after showing that the

answer to the aforementioned question is affirmative, we objectively determine the best generalized Newtonian description for the human blood shear rheology. Third, we develop accurate parametric representations for the dependence of yield stress and model viscosity on the most critical parameters under physiological conditions (hematocrit, fibrinogen concentration and temperature).

To address the third goal, i.e. to find effective parametric representations for the steady shear blood flow rheology, we consider the concept, suggested by Merrill [1969] and many other investigators, that blood forms rouleaux of red blood cells at low shear rates and that these rouleaux reversibly disintegrate when the shear rate is increased. The formation of the rouleaux aggregates is behind the underlying microscopic explanation for the macroscopic yield stress. Furthermore, we consider that RBC adsorption is done primarily through fibrinogen [Merrill (1969)], with synergic impact from other macromolecules [Morris (1989)], and that it is a critical, onset-type phenomenon. Thus, the dependence of the yield stress on the fibrinogen concentration, and the difference of the hematocrit from a critical hematocrit value, which in turn is also fibrinogen-dependent, is justified. To elucidate those dependences, we use literature data of normal human blood. An exception is the use of yield stress measurements of Morris et al who, apart from normal suspensions of RBCs in plasma, also used suspensions with an in-vitro augmented fibrinogen content. Finally, it is worth to be mentioned here that we treat blood phenomenologically as a rheologically homogeneous medium. Barbie and Cokelet (1971) showed that this leads to consistent results for tube steady state flow of diameter down to 29μm provided the local hematocrit value is used to characterize the blood condition.

The structure of this chapter is as follows. In Section 2.2 we briefly describe the methods used in carrying out our investigation. In Section 2.3 we present our results, focusing on our parametric representation. In the same section, we present the model verification and validation through a comparison of the model predictions against data used in the model development and additional independent data from the literature, respectively. In Section 2.4 we discuss the comparison of our model against additional data from the literature which are incompletely characterized. Finally, our conclusions follow in Section 2.5.

2.2 Methods

The methods selected in this work have been tailored to address the three key issues identified in the introduction: (a) model consistency, (b) model description and (c) parametrization.

2.2.1 Poiseuille flow data reduction

It is important to convert capillary viscometry data into Couette, in order to consistently compare rheological information from various sources. To achieve this task for viscometric capillary data we use the following formula that is derived based on the standard analysis of the flow of a simple fluid in a cylindrical tube [Bird et al. (1977)]:

$$\dot{\gamma}(\tau_w) = \tau_w \frac{d(U^*)}{d\tau_w} + 3(U^*), \tag{2.4}$$

where $\dot{\gamma}$ is the wall shear rate, $\tau_w = \Delta P/L \times R/2$ is the wall shear stress with $\Delta P/L$ denoting the pressure drop per unit length, and U^* is the pseudo-shear rate defined as $U^* = \frac{Q}{\pi R^3}$, with Q being the experimentally measured volumetric flow in the tube (vessel) and R being the tube radius. If necessary, the raw experimental data may need to be corrected for end effects as discussed in the literature [Bird *et al.* (1977)].

2.2.2 Constitutive model

The constitutive model that we are looking to identify in this work is a particular case of a viscoplastic generalized Newtonian fluid (i.e. one that exhibits a non-zero yield stress), described (for positive shear rates) by

$$\tau^m = \tau_y^m + A^m \times \dot{\gamma}^{k \cdot m}, \ \tau \geq \tau_y \tag{2.5}$$

where is the shear stress, is the yield stress, the shear rate, A denotes the model viscosity, and are model exponents. The choice for the constitutive model is motivated by two viscoplastic constitutive models that have been extensively used in the past, both of which are limiting cases of the general viscoplastic constitutive model described by Eq. (2.5), as discussed below.

2.2.2.1 The Herschel-Bulkley constitutive model

The Herschel-Bulkley model, a generalization of the power law model for systems endowed with yield stress, finds numerous applications in describing viscoplastic flows [Mewis and Wagner (2012)]. The corresponding constitutive

equation is described for positive shear rates as [Herschel and Bulkley, (1926); Mewis and Wagner (2012)]:

$$\tau = \tau_y + K \times \dot{\gamma}^k, \tau \geq \tau_y \tag{2.6}$$

where τ_y represents the yield stress, and K, k are the corresponding power law (positive) factors. The generalized Newtonian fluid expression, Eq. (2.5), reduces to the Herschel-Bulkley model for $m = 1$. In turn, the Herschel-Bulkley model reduces to the Bingham model for $k = 1$.

2.2.2.2 The Casson constitutive model

The Casson model is another popular phenomenological viscoplastic model, used frequently in the steady-state analysis of blood flows. The physical model upon which its derivation is based is that of reversible aggregation, at low shear rates, of suspended particles into rod-like aggregates (rouleaux formation). As the shear rate is increased, the rod-like aggregates decompose into smaller aggregates and, ultimately, into elementary particles [Merrill *et al*. (1963b)]. The Casson model is described for positive shear rates as:

$$\sqrt{\tau} = \sqrt{\tau_y} + \sqrt{\mu\dot{\gamma}}\ , \tau \geq \tau_y \tag{2.7}$$

where τ_y represents the yield stress and μ is the model viscosity.

In a square root "Casson" plot, $\tau^{1/2}$ vs. $\dot{\gamma}^{1/2}$, the Casson model predicts a linear relationship between the square root of the shear stress and the square root of the shear

rate. In such a plot, the slope represents the square root of the viscosity, while the square root of the yield stress is given by the *y*-intercept. Such a plot is then the natural one for the identification of the Casson model appropriateness to describe the data as well for determining best fits for its parameters. Furthermore, based on the Casson equation, one can calculate the resulting pseudo-shear rate expression for pressure driven (Poiseuille) flow in a capillary tube as [Merrill *et al*. (1965)]:

$$U^* = \frac{\tau_w}{4\mu}\left[1 - \frac{1}{21}\left(\frac{\tau_y}{\tau_w}\right)^4 - \frac{16}{7}\left(\frac{\tau_y}{\tau_w}\right)^{1/2} + \frac{4}{3}\left(\frac{\tau_y}{\tau_w}\right)\right]. \qquad (2.8)$$

Note that this expression corrects the corresponding formula reported by Truskee *et al*. (2009) for the factors -1/21 and 4/3 instead of 11/21 and 8/3, respectively.

2.2.3 Parametric equations

Parametric equations are needed in order to correlate the parameters of the Casson model, viscosity and yield stress, with the physiological conditions.

2.2.3.1 Model viscosity

The blood viscosity is known to depend strongly on the hematocrit level, while it also exhibits an Arrhenius type of dependence on the temperature of the suspension [Merrill *et al.* (1963); Merrill (1969)]. A list of proposed models for the apparent viscosity, η in Eq. (2.1), is presented in the work of Yilmaz and Gundogdu (2008). However, despite the long recognized dependence of viscosity on temperature, none of the listed models accounts for it explicitly. Merrill's experimental evidence [Merrill et

al., 1963a] suggests the same Arrhenious-type dependence for the blood apparent viscosity as that for water for moderate to high shear rates (where the model viscosity's contribution is significantly stronger than that of the yield stress in the expression for the apparent viscosity) while the blood's yield stress was found to be essentially temperature-independent. The simplest approximation that could satisfy both of these partially conflicting conditions (rigorously satisfied only in the limit of high shear rates) is what we adopted here. Namely, we introduced an Arrhenious-type temperature dependence only for the Casson model viscosity while treating the yield stress as temperature-independent. Thus, we propose a separable parametric equation for the Casson model viscosity, of the form:

$$\mu = g\left(Hct\right) \times \exp\left(\alpha / T\right), \tag{2.9}$$

where g is a function of Hct (the tube hematocrit) to be determined through data fitting, and the exponential function, describing the dependence on the temperature, T, is obtained from the literature. The pre-exponential factor, α, is taken from the temperature dependence of the viscosity of water as, according to Merrill [Merrill *et al.* (1963); Merrill (1969)] is the same with blood---see also the relevant discussion right before Eq. (2.17) in Section 2.2.3.2. Finally note that the model viscosity, μ, is a model parameter and it should not be confused with the apparent viscosity, defined in Eq. (2.1), which in general can depend on the shear rate.

2.2.3.2 Yield stress

The main physiological parameters of importance in the case of yield stress are the hematocrit and the fibrinogen concentration as experimental evidence exists that shows the yield stress to be essentially temperature-independent [Merrill et al. (1963)]. The vast majority of the parametric descriptions for yield stress in literature account only for the former parameter [Chien *et al*. (1966); Merrill *et al*. (1969); Zydney *et al*. (1991); Picart *et al*. (1998)]. The dependence on hematocrit is found to be either cubic [Merrill *et al*. (1969); Zydney *et al*. (1991); Picart *et al*. (1998)] or quadratic [Morris *et al*. (1989)]. Merrill *et al*. (1963a, 1969) have shown that yield stress is an onset phenomenon that is expressed only for cell concentrations above a critical hematocrit, Hct_c, an approach that was also used by Zydney *et al*. (1991). The work of Morris *et al*. (1989) shows a strong interaction between the effects of hematocrit and fibrinogen concentration on yield stress, therefore suggesting that the critical hematocrit is also expected to depend on c_f. However, this dependence, to be determined in this work as $Hct_c\left(c_f\right)$, has as yet not been quantified.

Furthermore, the use of a critical hematocrit allows us for a much more pertinent parametric representation of the yield stress as a critical, onset, phenomenon by considering the yield stress as a function of the difference of the hematocrit from the critical hematocrit value. In particular, the following parametric equation for yield stress is proposed here:

$$\tau_y = \begin{cases} f\left(\left[Hct - Hct_c\left(c_f\right)\right]^2, c_f\right) & Hct > Hct_c\left(c_f\right) \\ 0 & Hct \le Hct_c\left(c_f\right) \end{cases}, \tag{2.10}$$

where $f\left(\left[Hct - Hct_c\left(c_f\right)\right]^2, c_f\right)$ is a function of $\left[Hct - Hct_c\left(c_f\right)\right]^2$ and c_f to be determined by fitting. Note the dependence on the square of the difference of the local Hematocrit from its critical value. This was found empirically as providing a good fit to the data while requiring a small number of fitting parameters, (in fact, the minimum possible, as only one quadratic term is needed) as shown in Section 2.3.2, Eq. (2.14). Note that the quadratic dependence emerges naturally from the fit of the data when the difference from a critical hematocrit is used, the first time that such a parametric expression is employed. It allows for a much simpler final expression to be obtained involving only one term. As such, we believe that it is of practical (due to its simplicity) as well as of theoretical significance as the power law may be connected to the underlying percolation nature of the yield stress. This can potentially be further explored theoretically using percolation theory (see, for example, Balescu (1997)) albeit, due to the complexity of the phenomenon, such avenue has not been explored here.

2.3 Results

In our investigation we have used pertinent viscometric data from the literature. In Table 2.1 we list the works of various authors that have been used for the development and/or validation of our model, along with the relevant experimental conditions of each investigation.

Table 2.1. Physiological and rheological information of literature data that have been used in this investigation.*

Reference	Exper. Method	Capillary Diameter or Cylinder Gap	Shear rate (sec^{-1})	T (^oC)	*Hct %*	c_f (*g/dl*)
Barbee (1971)	Capillary	29μm-811μm	0.1-100	23	12.3-59.3	
Merrill *et al.* (1963a)	Couette	1465 μm	0.1-10	21 - 37	20.3-49.8	-
Merrill *et al.* (1965)	Capillary	288μm-850μm	0.02-200	19 & 22	20.1 & 39.3	
	Couette	1465 μm	0.02-25	19 & 22	20.1 & 39.3	-
Merrill *et al.* (1967)	Couette	1465 μm	0.1-300	37	40	0.18 & 0.27
Morris *et al.* (1989)	Yield stress chamber	-	-	25	40-80	0.1-0.9

* All listed investigations are in vitro studies of normal human blood.

2.3.1 Blood as a simple fluid

To test the simple fluid hypothesis, we are using experimental data of a sample that have been obtained in both a capillary and a Couette viscometer [Merrill *et al*. (1965)]. The reported yield stress value, as measured with the use of a Couette viscometer, is 0.0289 *dyne/cm*^{2}. First, the capillary data are fitted with a spline interpolation, as shown in Fig. 1, where $\bar{U}$ is a modified pseudo-shear rate defined as $\bar{U} = \frac{4Q}{\pi D^3} = \frac{1}{2}U^*$, with Q denoting the volumetric flow rate. Then, the fitted capillary data were reduced as shear stress vs. shear rate, with the use of Eq. (2.4), and compared against the Couette data in Fig. 2.

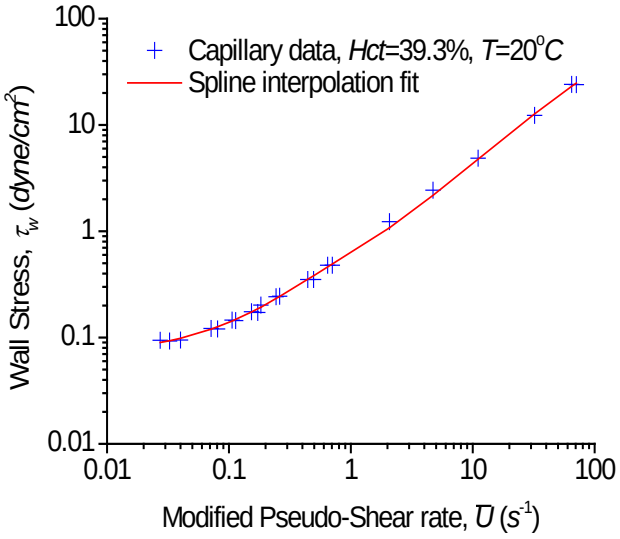

Figure 2.1. Capillary wall stress vs. modified pseudo-shear rate for a blood sample of $Hct = 39.3\%$ and at $T = 20°C$ [Merrill *et al*. (1965)]. Cross symbols: Raw data. Solid line: Spline interpolation fit.

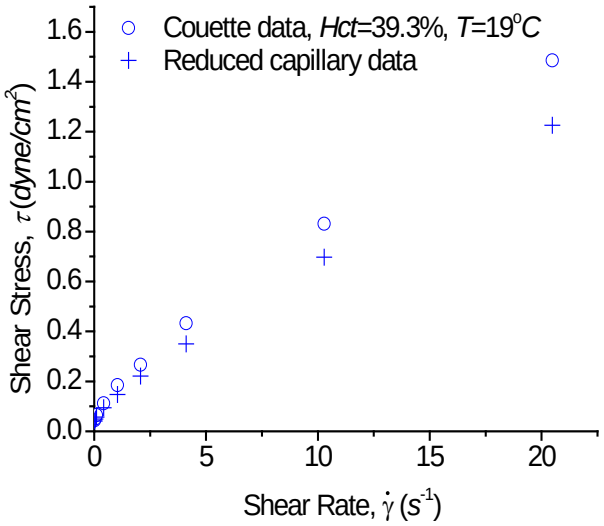

Figure 2.2. Shear stress vs. shear rate for a blood sample of $Hct = 39.3\%$ and at $T = 20°C$ [Merrill *et al*. (1965)]. Open circles: Couette measurements. Crosses: Reduced capillary data.

From Fig. 2, we notice that in the intermediate shear region $\left(\dot{\gamma} \le 5s^{-1}\right)$ there is very good agreement between the Couette measurements and the reduced capillary data. The maximum deviation between the two sets is ~17%, corresponding to the last datum in Fig. 2, while for the rest of the data the deviation is less than 10%. An additional pair of datasets from the same work [Merrill *et al.,* (1965)] but at a lower hematocrit, $Hct = 20.1\%$ has also been examined, where the Couette data are much closer to the reduced Poiseuille ones, with the data shown in the Section 2.4, in Figs. 2.12 and 2.13. Given the close agreement between the Couette and the reduced Poiseuille data for these two cases, we conclude that the simple fluid assumption for blood is a reasonable approximation for the case of steady-state shear flow.

2.3.2 Yield stress modeling and parametric estimation

As described in Section 2.2.3.2, we are concerned here with a more rational modeling of the yield stress based on its interpretation as a critical, onset phenomenon, with respect to Hct, and with the onset being dependent on the fibrinogen concentration. Our analysis is based on experimental data by Morris et al. (1989) that cover a wide range of plasma fibrinogen concentrations ($0.1 \leq c_f \leq 0.9$ g/dl), and hematocrits ($40\% \leq Hct \leq 80\%$). In that work, the empirical formula proposed by the investigators for the fit of the yield stress data is:

$$\tau_y = (-0.091 + 0.47 Hct + 0.22 c_f - 0.14 c_f^2 + 0.48 Hct \times c_f)^2, \qquad (2.11)$$

where the yield stress, τ_y, is in $dyne/cm^2$ and the fibrinogen concentration, c_f, in g/dl. This formula involves a quadratic dependence on the hematocrit and a quartic one on the fibrinogen concentration. It also shows a strong interaction between the effects of hematocrit and fibrinogen concentration on the yield stress. However, in this formula, the yield stress is not recognized as an onset phenomenon. Correspondingly, there are no predictions for a critical hematocrit below which the yield stress is zero. Nevertheless, as we show below, the data can be used to extract such information.

Towards that goal, it is better to represent the data, for fixed fibrinogen concentrations, in terms of square root of the yield stress versus hematocrit graphs, as there some of the non-linearities are eliminated (see Fig. 3). Indeed, as shown in Fig. 3 and consistent with Eq. (2.11), the dependence of the square root of the yield stress on the hematocrit is well approximated as linear for any given value of the fibrinogen

concentration. When extrapolated, these straight lines intersect the horizontal x-axis at positive values of hematocrit, Hct, that are decreasing as the fibrinogen concentration, c_f, increases. Based on that evidence, we postulate here the existence of a critical Hct, Hct_c, which, as a function of the fibrinogen, defines the onset of non-zero yield stress in blood flow.

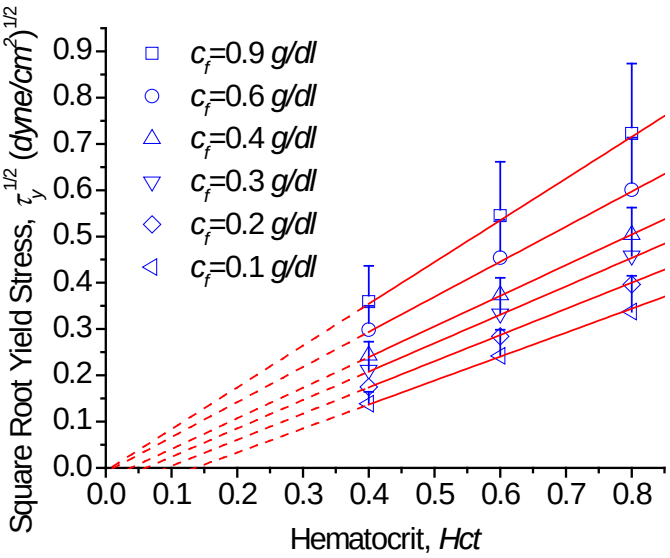

Figure 2.3. Experimental yield stress measurements (discrete symbols) and fitting curves (continuous lines) as a function of the hematocrit values based on the model of Morris [Morris *et al.* (1989)]. The error bars are +1.5 standard error of the mean and represent the upper 95% limit of normal by one sided test. Extrapolation of the model predictions is performed (dash lines) to obtain the critical hematocrit for each fibrinogen concentration (*x* intercepts).

The critical hematocrit data obtained from the *x*-intercepts are shown in Fig. 4, along with a quadratic fit, as a function of the fibrinogen concentration. The shaded region below the fitted line denotes the purely viscous region, i.e. the parameter region where blood behaves like a viscous Newtonian fluid without exhibiting a yield stress. From the good fit of the data, we conclude that the critical hematocrit can be accurately predicted as a quadratic function of the fibrinogen concentration, for concentrations less than $0.75\ g/dl$, where it assumes a minimum, and as a constant otherwise. The resulting equation is:

$$Hct_c = \begin{cases} 0.3126{c_f}^2 - 0.468c_f + 0.1764 & c_f < 0.75 \\ 0.0012 & c_f \geq 0.75 \end{cases}, \tag{2.12}$$

where the fibrinogen concentration, c_f, is in g/dl.

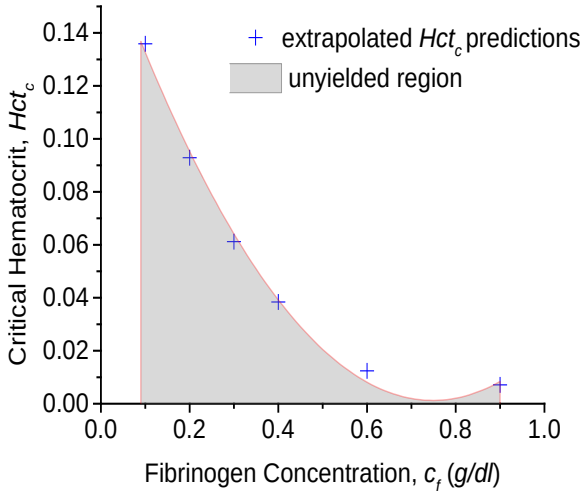

Figure 2.4. Critical hematocrit predictions as a function of the fibrinogen concentration based on the extrapolated data

shown in Fig. 2.3. Crosses: Extrapolated values. Solid line: Quadratic fit. Shaded area: unyielded zone.

The increasing slope of the fitting curve in Fig. 2.4 for c_f greater than 0.75 is an artifact of the quadratic fit rather than a consequence of the underlying physics. As explained in Section 2.3.4, at high fibrinogen concentrations there is a saturation effect. Thus, the curve is expected to monotonically decrease asymptoting to a small value at high concentrations. This is the explanation for the correction for fibrinogen concentrations more than those corresponding to the minimum of the quadratic fit, $0.75\ g/dl$, in the fitting approximation offered by Eq. (2.12).

In Fig. 2.5 we plot the slope of each curve in Fig. 2.3, $d(\tau_y)^{1/2}/dHct$, against the fibrinogen concentration. As shown in that figure, the dependence on the fibrinogen concentration is linear:

$$d(\tau_y)^{1/2}/dHct = 0.5084 \times c_f + 0.4517, \tag{2.13}$$

where the slope, $d(\tau_y)^{1/2}/dHct$, is in $\sqrt{dyne}/cm$ and the fibrinogen concentration, c_f, in g/dl.

Combining the information extracted from Figs. 2.3-2.5, with the formula described by Eqs. (2.12) and (2.13), leads to the following parametric form for the yield stress:

$$\tau_y = \begin{cases} [(Hct - Hct_c)^2 \times (0.5084 c_f + 0.4517)^2 & Hct > Hct_c \\ 0 & Hct \le Hct_c \end{cases}, \tag{2.14}$$

where the yield stress, τ_y, is in $dyne/cm^2$ and the fibrinogen concentration, c_f, in g/dl. Notice that the dependence of the yield stress on the hematocrit is through the square of the difference of the hematocrit from its critical value. This arises naturally from the data, reinforcing our interpretation of the yield stress as an onset phenomenon.

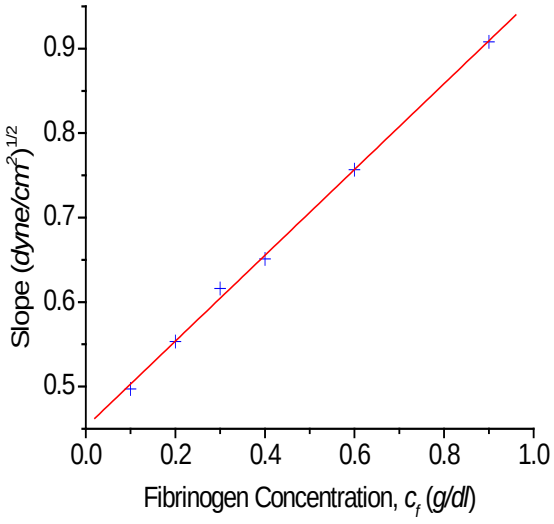

Figure 2.5. Dependence of the slope, $d(\tau_y)^{1/2}/dHct$, on the fibrinogen concentration, for the data shown in Fig. 3. Crosses: Discrete data. Solid line: Linear fit.

The raw yield stress measurements of Morris *et al*. (1989) were made at a wide range of fibrinogen concentrations that span and exceed the physiological range. Including all experimental data of Figure 2.3 not only does not affect the validity of Eqs.

(2.12)-(2.14) within the physiological range but it also makes them potentially applicable to certain pathological conditions involving hyperfibrinogenemia.

2.3.3 Constitutive model and parametric estimation for model viscosity

2.3.3.1 Best constitutive model

Once it has been determined that the simple fluid assumption is a reasonable approximation for describing the steady-shear flow behavior of blood, it still remains the task of systematically investigating for an appropriate equation to describe it. Towards that goal, and given the overwhelming evidence (in general) in favor of the presence of a nonzero yield stress, we investigated the quality of fit of available experimental literature viscometric data against various versions of the proposed generalized viscoplastic constitutive model, Eq. (2.5).

For any fixed value of the exponent m, a simple rearrangement of Eq. (2.5) leads to the following form:

$$\log\left(\tau^m - \tau_y^m\right)^{\frac{1}{m}} = \log A + k \times \log \dot{\gamma}. \tag{2.15}$$

Observe that for a given value of m this is a linear equation of the experimentally determined quantity $\log\left(\tau^m - \tau_y^m\right)^{\frac{1}{m}}$ with respect to $\log \dot{\gamma}$. The remaining unknown parameters, $\log A$ and k, are determined from a Least Squares (LS) fit, as the *y*-intercept and the slope, respectively [Edwards (1979)]. A Least squares fit also provides the correlation coefficient, $r, |r| \le 1$. The closest the magnitude of the correlation coefficient is to 1 the better the fit is [Edwards (1979)].

We have applied the LS analysis on (a) five Couette viscometric datasets [Merrill *et al*. (1963a, 1965, 1967)] and (b) two sets of reduced capillary data that correspond to two of the Couette viscometric datasets [Merrill *et al*. (1965)]. Pertinent information on the key physiological and rheological characteristics of these datasets is to be found in Table 2.2. For each dataset the reported yield stress, τ_y, has been experimentally determined by the respective investigators. For each dataset the LS calculations were performed for three distinct values of the parameter m $\left(1/3, 1/2, 1\right)$. In each case, the parameters A and k are determined by the fit.

Table 2.2. Physiological and rheological information of the selected under study datasets.

Dataset #	Reference	*Hct*	c_f (*g/dl*)	τ_y (*dyne/cm*^{2})
1	Merrill *et al*. (1965)	39.3%	-	0.0289
2	Merrill *et al*. (1965)	20.1%	-	0.0036
3	Merrill *et al*. (1965) (reduced capillary data)	39.3%	-	0.0289
4	Merrill *et al*. (1965) (reduced capillary data)	20.1%	-	0.0036
5	Merrill *et al*. (1963a)	35.5%	-	0.019
6	Merrill *et al*. (1967)	40%	0.18	0.0188
7	Merrill *et al*. (1967)	40%	0.27	0.04

Note: Unless otherwise indicated the data correspond to Couette viscometry.

The resulting k values, as well as the square of the correlation coefficients, r^2, are reported in Table 2.3. Of interest is that $m = 1$ corresponds to the Herschel-Bulkley model, which for a value of $k = 1$ reduces further to the Bingham model, whereas the combination $m = 1/2$ and $k = 1$ characterizes the Casson model.

Table 2.3. Least squares data of the cases of the selected under study datasets.

Cases →	$m = 1/3$		$m = 1/2$		$m = 1$	
Dataset #	k	r^2	k	r^2	k	r^2
1	1.2883	0.9974	0.9684	0.9992	0.6714	0.9961
2	1.2210	0.9983	0.9912	0.9991	0.8047	0.9964
3	1.3076	0.9996	0.9768	0.9999	0.6676	0.9936
4	1.3194	0.9976	1.0329	0.9998	0.7817	0.9967
5	1.2453	0.9988	0.9711	0.9999	0.7297	0.9982
6	1.2705	0.9939	0.9967	0.9980	0.7575	0.9964
7	1.2863	0.9927	0.9977	0.9971	0.7409	0.9957

The selection of the most suitable constitutive model was based on two criteria, the correlation coefficient r^2 and the dispersion of the k value. The closest the magnitude of the correlation coefficient to 1 is the better the fit [Edwards (1979)]. On the other hand, the smallest the dispersion of computed k value among the seven data sets, the more reliable and consistent the constitutive model is (a highly varying k value would have meant an inability to uniquely evaluate it). Table 2.3 shows that, based on both criteria, the most suitable constitutive model is the Casson, since both conditions are met when $m = 1/2$. In particular, for each data set examined the r^2 is highest, and the dispersion of the computed k value among the seven datasets is minimum, when $m = 1/2$. Thus, based on the analysis of the seven data sets listed in Table 2.3, the Casson constitutive model emerges naturally from the data as the most suitable one for the description of the steady state simple shear rheology of blood.

It should be noted that this is not a rigorous proof since the conclusion has been based on a particular, finite, number of investigations that has been used in the analysis and on a specific form of the most general constitutive model, provided by Eq. (2.5). The latter, albeit is general enough to cover many common particular cases (including the Hershel-Bulkley model) it is clearly not the most general that one could have devised. Nevertheless, it is likely that anything more general would have required more parameters, and more parameters would have required more experimental data. However, the number of experimental data available that were well characterized are fairly limited and not too many beyond those used in this study. Based on this consideration and the fact that the Casson model naturally emerges as the optimum fit for the data and the general model equation used in this work, we believe that strong evidence is provided in favor of the Casson model. Therefore, in the rest of the paper only the Casson model is further considered.

2.3.3.2 Parametric estimation for model viscosity

Having shown the suitability of the Casson model and also having developed a parametric expression for the calculation of yield stress, the last stage towards the completion of our model is the parametrization of the Casson model viscosity, μ. The key physiological parameter (other than the temperature that was discussed earlier) on which the model viscosity is anticipated to sensitively depend upon is the tube hematocrit, Hct. For our parametrization we tried to find a set of data covering a wide range of hematocrit values. Those turned out to be capillary data. Therefore, they have to be reduced to equivalent Couette data prior to the analysis. More specifically, we use the in vitro capillary data of Barbee (1971) which consist of 9 sets of shear stress versus

pseudo-shear rate data, each set having a distinct and specified hematocrit between 0.123 and 0.593. Conveniently, those data can be parametrically represented, as suggested by Lee (1977), following a modification of an earlier form provided by Barbee (1971), as:

$$\tau_w = \begin{cases} 4U^* n_p e^{5.8Hct\left(4U^*\right)^{-0.15}} & 0.75 \le U^* \le 37.5 s^{-1} \\ 4U^* n_P e^{Hct\left[2+18.5\ln\left(4U^*\right)^{-2}\right]} & U^* > 37.5 s^{-1} \end{cases}, \qquad (2.16)$$

where $n_p = 1.67 \times 10^{-2}\, dyne \times s/cm^2$ is the plasma viscosity, τ_w is the wall shear stress and U^* is the pseudo-shear rate in s^{-1}. We have used Eq. (2.16) in this work instead of the original data as it is much more convenient due to its explicit parametric dependencies. Thus, when we combine Eq. (2.16) and Eq. (2.4) we obtain the reduced Couette predictions, typical results of which are shown in Fig. 2.6.

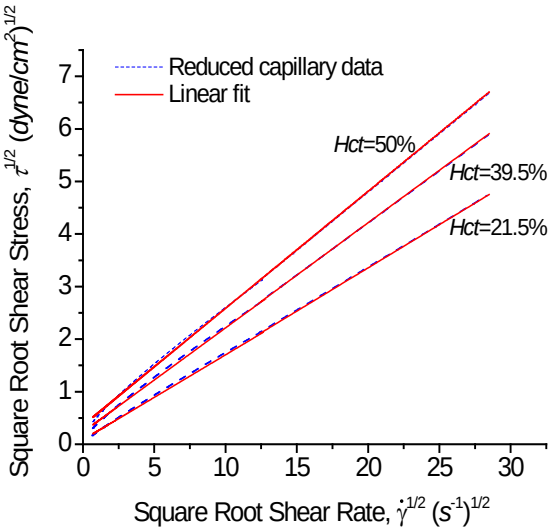

Figure 2.6. Casson plots, $\tau^{1/2}$ vs. $\dot{\gamma}^{1/2}$, for three data sets from the work of Barbee (1971) each one corresponding to a different hematocrit value as indicated. Dash lines: Reduced capillary data. Solid lines: Linear fits.

As indicated in Fig. 2.6, when the data are plotted as a $\tau^{1/2}$ vs. $\dot{\gamma}^{1/2}$, the reduced data (dashed lines) display linearity. The quality of the linear fits is equally good for the six remaining data sets (data not shown). This serves as further verification for the suitability of the Casson equation. In fact, the Casson constitutive equation correlates excellently with all the Barbee (1971) viscometric data in a shear rate range between ~ $0.5\ \mathrm{s}^{-1}$ and ~ $800\ s^{-1}$. Upon reduction and linear fit of the nine data sets, we obtain nine model viscosities, one for each hematocrit, as shown in Fig. 2.7.

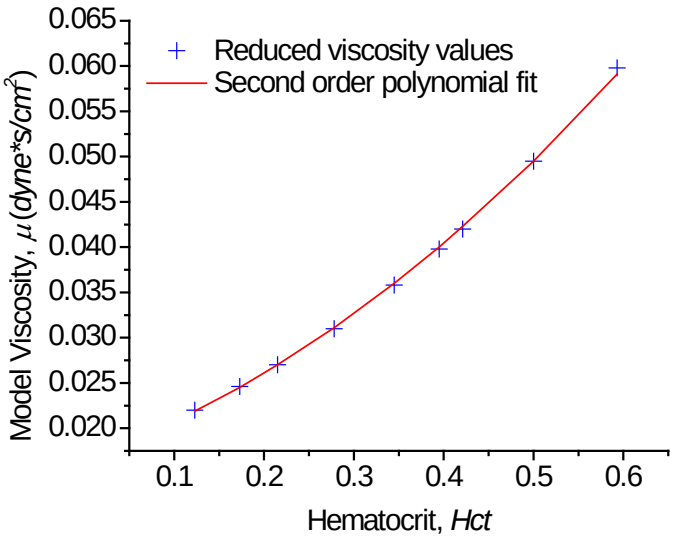

Figure 2.7. Second order polynomial fit (solid line) to the viscosity values obtained from the Casson plots of the reduced in-vitro capillary data of Barbee (1971) (cross symbols)---typical results of which are shown in Fig. 6---as a function of the hematocrit values.

Fig. 2.7 shows that a quadratic fit describes excellently the viscosity dependence on the hematocrit. To ensure consistency we need to force the model viscosity to reduce to the plasma viscosity, n_p, at zero Hct. This leaves for obtaining the quadratic fit shown in Fig. 2.7 only two unknowns. Those are most conveniently obtained by a linear least squares fit of the reduced viscosity $\left(n-n_p\right)\Big/\left(n_p Hct\right)$ with respect to Hct as the $x-\text{intercept}$ and the slope, 2.0703 and 3.7222, respectively. In this way, we also get from the closeness of the square of the correlation coefficient, $r^2=0.9949$, to 1 another confirmation for the good quality of the fit.

For the complete parametrization of viscosity the temperature dependence needs also to be taken into account. Merrill *et al*. (1963a) have shown that, for shear rates between 1 sec^{-1} and 100 sec^{-1} and for temperatures between 10°C and 37°C, the relative apparent viscosity of whole blood to water is independent of temperature. In the same investigation it was proposed that the temperature function of the apparent (shear rate dependent) viscosity is expressed by an Arrhenius type of equation with the same activation energy as is applicable to water. However, in the same investigation it was also found that the yield stress is essentially temperature independent [Merrill *et al*. (1963a)]. The best way to accommodate those two, partially conflicting, experimental observations in the present model is by restricting the temperature dependence for the model viscosity only, assuming a temperature-independent yield stress. Furthermore,

we take the dependence of the model viscosity on the temperature to be the same as for water. Thus, we quantify that dependence in an Arrhenius-type expression that we obtained using a least squares fit between the natural logarithm of the viscosity of water, $\ln(\mu_w)$, and the inverse of the absolute temperatures, $1/T$, over the desired range of temperatures of 10-37 ^oC. We based that calculation on the very accurate viscosity data for water reported in [Korson *et al*. (1969] to obtain an optimum proportionality coefficient. Thus, the final form for the viscosity model is:

$$\mu = n_p\left(1+2.0703\times Hct+3.7222\times Hct^2\right)\times\exp\left(-7.0276\left(1-\frac{T_0}{T}\right)\right), \qquad (2.17)$$

where T_0 is the reference temperature of 273.16+23=296.16 ^oK (at which the Barbee data were taken and the plasma viscosity $n_p = 1.67\times10^{-2}\ dyne\times s/cm^2$ is measured), and T is the blood absolute temperature (in ^oK). Alternatively, one can construct an Arrhenius expression around the reference temperature by linearizing an empirical fit of experimental data provided by Eq. (1) in [Kampmeyer (1952)] around the reference temperature. This yields a slightly different coefficient of 6.9274 instead of 7.0276 in the RHS of Eq. (2.17). Note that use of either coefficient results in less than 1% relative error for the estimation of the water viscosity over the desired temperature range of 10-37 ^oC. In the following we use the slightly more accurate (for the range of temperatures sought) coefficient determined through the direct least squares fit of the data, as it appears in Eq. (2.17).

Eq. (2.17) predicts that, at room temperature and in the limit of very low hematocrit, the so-called intrinsic viscosity is equal to 2.07, a value which is lower than the Einstein result for a rigid sphere. This deviation is expected as Einstein examined

ideal, non-interacting rigid spheres while the RBCs are deformable and interact with neighboring cells. Moreover, unlike the rigid sphere, the RBC is characterized by an internal viscosity (hemoglobin solution for RBC) and the ratio of internal to external (plasma) viscosity is known to affect the intrinsic viscosity of a sample [Vitkova *et al*. (2008)]. Theoretically one can show that both these conditions lower the intrinsic viscosity below Einstein's value of 2.5 [Happel and Brenner (1983)] and that the value 2.07 coming from our prediction is not inconsistent to those theoretical considerations, albeit a direct a priori evaluation is not possible due to the additional effects that exist in actual blood (such as the interactions between the RBC and between those and other blood constituents).

In the following Sections (2.3.4 and 2.3.5) we test the quality of the derived model. We start with the model verification, where we examine whether the model can predict the specific data upon which its derivation was based. In Section 2.3.5 we validate the model against additional experimental evidence that were not used in the model development.

2.3.4 Model verification

For verification purposes we tested our model against the experimental wall stress vs. shear rate data of Barbee (1971), based on which the parametric expression of viscosity, Eq. (2.17), was derived. In that study, the fibrinogen concentrations in plasma were not reported. Therefore, through Eqs. (2.14) and (2.12), a fit was made to the experimental yield stress data, resulting to a fibrinogen concentration of 0.35 *g/dl*. This is a very reasonable estimate, almost in the middle of the reported physiological range ($0.1\,g/dl \le c_f \le 0.4\,g/dl$) [Merrill *et al*. (1969)]. A comparison between the

nine available experimental datasets and our model predictions is shown in Fig. 2.8 in terms of the original capillary wall stress vs. (modified) pseudo-shear rate relations.

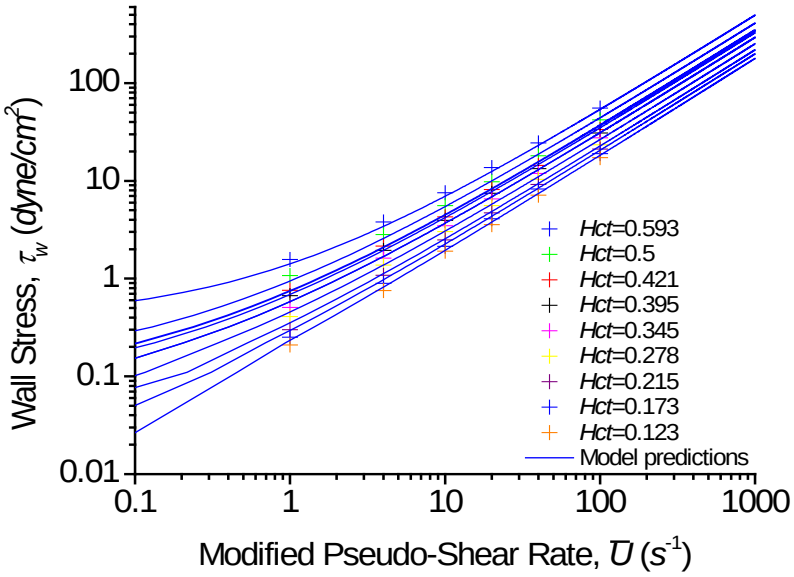

Figure 2.8. Wall stress vs. modified pseudo-shear rates model predictions (solid lines) vs. capillary data [Barbee (1971)] (cross symbols). For any fixed modified pseudo-shear rate value the data are presented in the same order, high to low hematocrits from top to bottom, as in the legend. A constant fibrinogen concentration of 0.35 *g/dl* was used for the evaluation of the yield stress required in the model.

As Fig. 2.8 shows, our model provides excellent correlation of experimental data at hematocrits (Hct) between 0.3 and 0.5, and modified pseudo-shear rates ($\bar{U} = U^*/2$)

between 20 and 100 s^{-1}, the most commonly encountered data. The observed deviations in the low pseudo-shear rates appear to be due to the use of a single fibrinogen concentration for all nine fits. The fibrinogen content corresponding to each one of the data sets is unknown, and albeit it is likely that it was within the physiological range it may still have varied within that range with different values for each case as the blood samples have been taken from different donors.

Further verification of the yield stress model was performed by comparing the predictions to the experimental data of Morris *et al.* (1989) that were used for the development of the yield stress parametrization, Eqs. (2.12) and (2.14). The results are shown in Fig. 2.9.

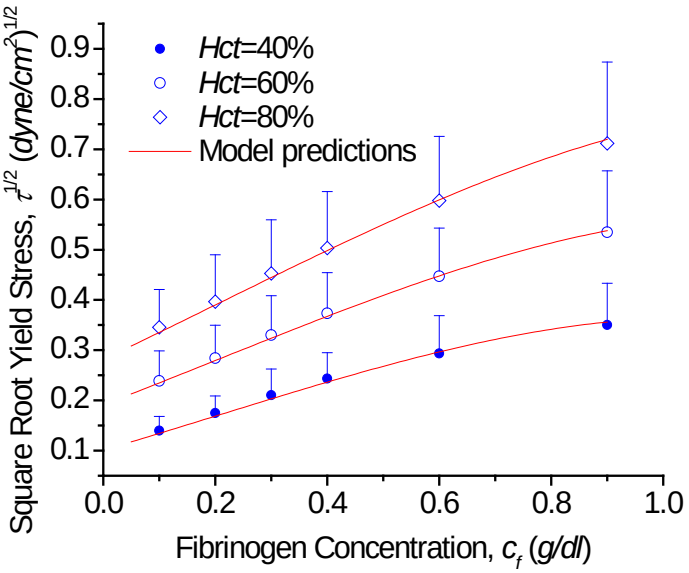

Figure 2.9. Square root of the yield stress vs. fibrinogen concentration for three different hematocrit values. The solid lines represent the predictions of our model based on Eqs. (14) and (12). The symbols

represent the experimental data that included blood samples from seven healthy donors and the error bars are +1.5 standard error of the mean and represent the upper 95% limit of normal by one sided test [Morris *et al*. (1989)].

In Fig. 2.9 we see a decreasing effect of fibrinogen to the yield stress at high concentrations and a relative insensitivity of yield stress to fibrinogen at low concentrations (realized by the constant slope at low fibrinogen concentrations). Both of these effects have been reported [Morris *et al.* (1989); Merrill *et al*. (1966)]. The former is identified as a saturation effect, while the latter as a threshold effect. Our model captures both of these phenomena as it is implied by the reduced slope of the curves observed at high fibrinogen concentrations and by the exhibited linearity at low concentrations, respectively (see Fig. 2.9). Strictly speaking, the postulated model should be used only for fibrinogen concentration and hematocrit values within the ranges specified by the experimental evidence, i.e. for fibrinogen concentrations between 0.1 and 0.9 g/dl and for hematocrit values between 0.4 and 0.8. However, the smoothness of the profiles in Fig. 2.9 and the simplicity of the proposed expressions, Eqs. (2.12) and (2.14), are suggestive for a potential validity even outside that range, certainly for lower values, from the mentioned minima down to zero.

2.3.5 Model validation

Merrill and Pelletier (1967) have reported coaxial cylinder Couette viscometer data for two samples with a specified innate plasma fibrinogen concentration. As seen

in Fig. 2.10, our model correlates well with these experimental data, also presenting additional evidence in favor of the Casson model hypothesis. Furthermore, the reported yield stresses, $\tau_y = 0.04 \, {dyne}/{cm^2}$ for the sample with a fibrinogen concentration, $c_f = 0.27 \, {g}/{dl}$ (upper graph in Fig. 10), and $\tau_y = 0.0188 \, {dyne}/{cm^2}$ for $c_f = 0.18 \, {g}/{dl}$ (lower graph in Fig. 2.10) are in good agreement with the predictions of our model $\tau_y = 0.0371 \, {dyne}/{cm^2}$ and $\tau_y = 0.0262 \, {dyne}/{cm^2}$, respectively.

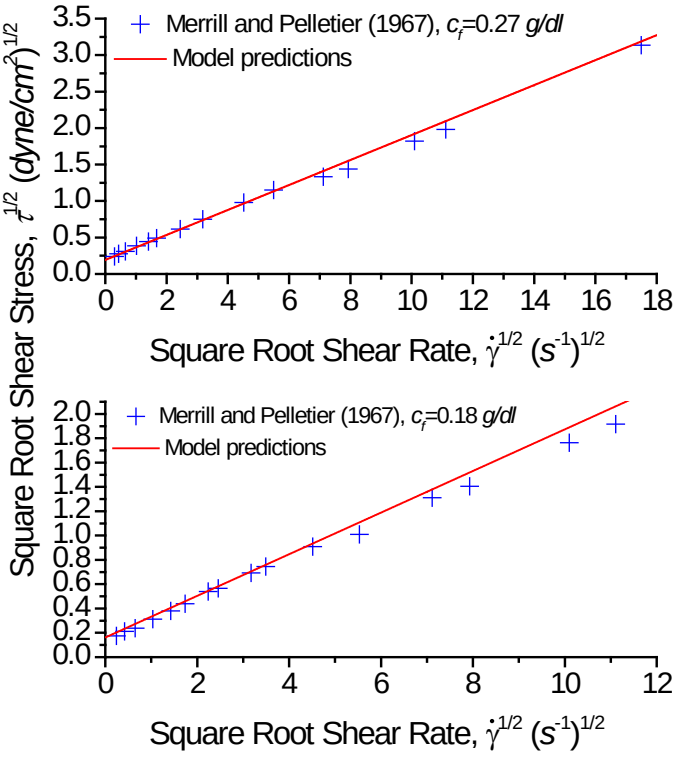

Figure 2.10. Casson plots, $\tau^{1/2}$ vs. $\dot{\gamma}^{1/2}$, for Couette viscometer data of two blood samples [Merrill and Pelletier (1967)]. Upper plot: Hematocrit 40%, temperature 37°*C*, fibrinogen concentration 0.27 *g/dl*. Lower plot: Hematocrit 40%, temperature 37°*C*, fibrinogen

concentration 0.18 *g/dl*. Solid lines: Model predictions. Cross symbols: Experimental data.

Additional results on the fibrinogen dependence of the yield stress have been provided by Merrill *et al.* (1966, 1969). Merrill's experiments have been conducted at a constant hematocrit of 40%, with red blood cells suspended either in physiological plasma [Merrill *et al.* (1969)] or in plasma-saline solutions [Merrill *et al.* (1966)]. Our model is in good agreement with the results based on the physiological plasma suspensions. When studying the yield stress of normal human blood ($Hct = 40\%$) as a function of endogenous fibrinogen, Merrill *et al.* (1969) reported a variation over the range 0.01-0.06 *dyne/cm*^{2}. The fibrinogen concentration in that study varied between 0.14-0.42 *g/dl*. Between these limiting c_f values our model predicts a $\tau_y$variation in the range of 0.0219-0.059 *dyne/cm*^{2}. Note that fibrinogen introduced by addition requires substantially higher concentrations to produce a given yield stress [Merrill *et al.* (1966)], indicating that other proteins present in blood play also a role in the yield stress development.

In the case of saline-plasma solutions, the reported results strongly deviate from our model predictions. The experimental yield stress values in this case are constantly over-predicted, especially at high fibrinogen concentrations (greater than 0.4 *g/dl*), by an order of magnitude. As explained in the subsequent work of Morris *et al.* (1989), this deviation is attributed to the higher potency of the fibrinogen-plasma solutions in their effect on yield stress, compared to the fibrinogen-saline solutions. The two

solutions contain a different mix of proteins, such as immunoglobulin and fibronectin, which are capable of augmenting the cell-to-cell adhesions.

Merrill also reported the existence of a critical hematocrit, below which blood does not exhibit a yield stress [Merrill (1969)]. Based on his experimental evidence, the critical hematocrit values range approximately from 0.04 to 0.08. However, direct quantification of the effect cannot be assessed as the fibrinogen concentration of the samples, based on which this range was specified, has not been reported. To the best of our knowledge, none of the models in the literature quantifies this dependence.

We have developed such a quantitative correlation, Eq. (2.12), that we extracted from the data of Morris *et al*. (1989). The corresponding critical hematocrit predictions are shown in Fig. 2.4. If we assume that physiological fibrinogen concentrations were employed, that is in the range ($0.1\, g/dl \le c_f \le 0.4\, g/dl$) [Merrill *et al*. (1969)], then our predicted Hct_c range is 0.039-0.13. In that case, our model predictions for the critical hematocrits for the onset of yield stress compare reasonably well with the reported range by Merrill that can, therefore, be used as a validation of our expression.

2.4 Discussion

In this section we continue the comparison of model predictions against data from the literature. Thus, this discussion offers additional validation of the model parametrization. However, this is offered separately from the model validation described in the previous section as the datasets used here are less complete, in terms of the range of values covered or their characterization or both.

2.4.1 Comparison of model predictions to experimental yield stress measurements

Numerous investigations for the determination of yield stress dependence on the hematocrit have been carried out in the past [Merrill *et al*. (1963); Chien *et al*. (1966); Morris *et al*. (1987); Zydney *et al*. (1991); Picart *et al*. (1998)]. The experimental measurements of the aforementioned investigations are presented in Fig. 2.11. We selected the particular studies presented in Fig. 2.11 as being more representative and self-consistent among the overall results available in the literature. The variability of the reported results is still important, yet much less than seen in other works of the literature not shown here. As two extreme examples we can mention the data of Charm and Kurland (1967) (reporting yield stress values much higher than the ones shown) and that of Benis and Lacoste (1968) (much lower). The depicted data in Fig. 2.11 were obtained by three different experimental techniques. Morris *et al.* (1987) used a chamber-sedimentation method, Picart *et al.* (1998) applied a direct rheometrical measurement of stress at 0.001 s^{-1}, while the rest were based on an extrapolation from low shear rheometry. The fact that three distinct experimental procedures yield similar results makes the particular evidence shown in Fig. 2.11 more trustworthy than the values of (a) Charm and Kurland (1967) who reported a yield stress of the order of 0.095-0.4 $dyne/cm^2$ for a hematocrit of 0.18-0.56 or (b) Benis and Lacoste (1968) who reported yield stress values lower by an order of magnitude to those shown in Fig. 2.11 over the hematocrit range of 0.41-0.73.

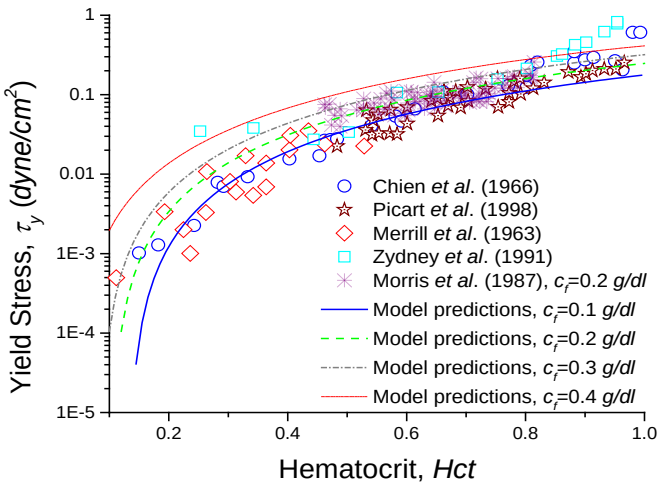

Figure 2.11. Yield stress vs. hematocrit. Continuous lines: Model predictions for different values of fibrinogen concentration as shown in the legend. Symbols: Yield stress measurements obtained by direct measurement [Picart *et al.* (1998)], chamber sedimentation [Morris *et al.* (1989)] and extrapolation form low shear [Chien *et al.* (1966), Merrill *et al.* (1963)]. Except from the data of Morris *et al.* (1987), where $c_f \cong 0.2\, g/dl$, the fibrinogen content for the rest of the experimental data is unknown.

In Fig. 2.11, the set of data of Morris (1987) is the only one for which the average fibrinogen concentration has been reported $\left(c_f \cong 0.2\ g/dl\right)$. In the same figure, model predictions are provided at four distinct fibrinogen concentrations spanning the physiological range. The predictions for $c_f = 0.2\ g/dl$ are close to the set of data by Morris. The predictions for all four different fibrinogen concentrations show the effect of fibrinogen on yield stress as well as its anticipated yield stress variability from one individual to another, given that they span the physiological

range. From Fig. 2.11 we see that the variability of the model predictions is very comparable to that seen in the data; furthermore, we can see an almost perfect overlap for hematocrit values in the range of 0.4 – 0.8 which is also the range, as mentioned above, where one trusts the most the model parametrization. For the lower hematocrit values, there is still considerable overlap, albeit one can also see some systematic deviations, the model predictions being higher than the data. Still, given the inherent variability of the data, the uncertainly on the fibrinogen concentration, and the experimental errors associated especially with the low values of the measured yield stress, we do not feel that there is enough experimental evidence to warrant further changes to our parametric expressions.

2.4.2 Comparison of model predictions to viscometry data with unspecified c_f

Our extensive literature review has only revealed a very limited number of reported viscometric blood flow data with known fibrinogen concentrations. Those have been used in the previous section for model verification and validation. Here we present an attempt to approximately fit and interpret additional data for which the fibrinogen concentrations are unknown. In Fig. 2.12 we present the Couette experimental data by Merrill *et al*. (1965) for two datasets at two different hematocrits with, however, unspecified fibrinogen content. The rheological parameters for the two cases have been independently fit by the investigator and we report them in Table 2.4. From the reported yield stress and hematocrit, and with the use of Eqs. (12) and (14), we were able to back calculate the fibrinogen concentration. The values obtained for the two samples are 0.215 *g/dl* and 0.206 *g/dl* corresponding to a hematocrit of 39.3% and

20.1%, respectively. An average concentration of 0.21 *g/dl* was then used in both cases to fit the viscometric data with the results shown in Fig. 2.12.

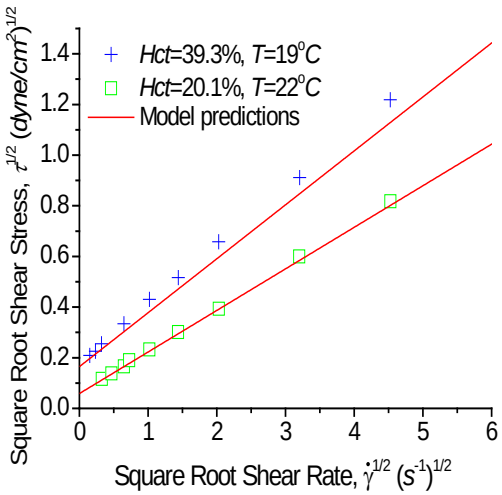

Figure 2.12. Casson plots, $\tau^{1/2}$ vs. $\dot{\gamma}^{1/2}$, for Couette viscometer data of two blood samples [Merrill *et al.* (1965)]. Solid lines: Model predictions. Symbols: Experimental data for the conditions shown.

The back calculation of the fibrinogen concentration and then its further usage in our model is justified on two grounds. First, even though not explicitly mentioned in the work of Merrill *et al.* (1965), we expect the two datasets to have the same fibrinogen content, as both originated from the same blood sample. Had that not been the case, using the same c_f to fit the two data sets would have resulted in a poor prediction of the yield stress, at least for one of the two sets. Moreover, the c_f prediction of roughly 0.21 *g/dl* is a reasonable value as it is well within the

physiological range that Merrill has been using in his studies [Merrill *et al*. (1966, 1967, 1969)].

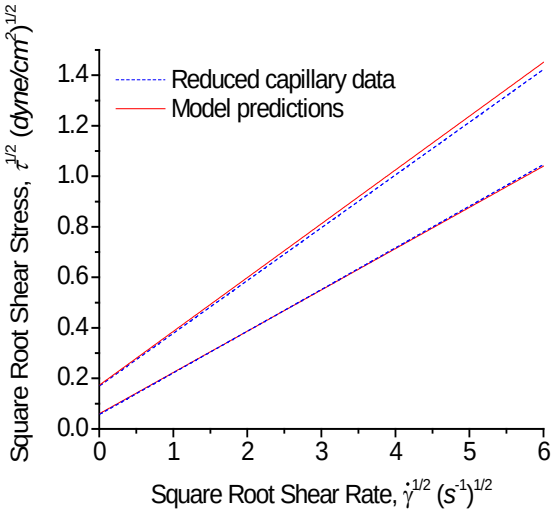

Figure 2.13. Casson plots, $\tau^{1/2}$ vs. $\dot{\gamma}^{1/2}$, for reduced capillary data of two blood samples [Merrill *et al.* (1965)]. Solid lines: Model predictions. Dash lines: Experimental data, top line: *Hct*=39.3%, *T*=19º*C*; bottom line: *Hct*=20.1%, *T*=22º*C*.

As Fig. 2.12 shows, the model predictions are in very good agreement with the viscometric data. The apparent deviation in the first set ($Hct = 39.3\%$) is due to the predicted viscosity value which is ~17% lower than the Couette-measured viscosity for that sample, while the second set is in excellent agreement with our model. It is

interesting to notice that, for both datasets, the model-predicted viscosity is in significantly better agreement with the reduced-capillary viscosity values, compared to the experimentally measured values, as demonstrated in Table 2.4 (see also Fig. 2.13). Thus, we can infer that the noticeable, yet acceptable, deviation observed in the first set is due to the approximate nature of the simple fluid hypothesis (manifested here in the discrepancy between Couette and capillary data), as already seen in Section 2.2.1 and Fig. 2.2.

Table 2.4. Rheological parameters: Data and predictions.

		Parameters directly obtained from Couette viscometer [Merrill *et al.* (1965)]		Parameters obtained from reduced capillary data [Merrill *et al.* (1965)]		Model Predictions	
Hct	Temperature , (^oC)	$\tau_y^{\frac{1}{2}}$, (*)	$\mu^{\frac{1}{2}}$, (**)	$\tau_y^{\frac{1}{2}}$, (*)	$\mu^{\frac{1}{2}}$, (**)	$\tau_y^{\frac{1}{2}}$, (*)	$\mu^{\frac{1}{2}}$, (**)
39.3%	19	0.17	0.229	0.173	0.213	0.1682***	0.2089
20.1%	22	0.06	0.1648	0.057	0.165	0.0608***	0.1634

* $(dyne/cm^2)^{1/2}$

** $(dyne \times s/cm^2)^{1/2}$

*** Based on the back-calculated value of $c_f = 0.21 \, g/dl$

2.5 Conclusions

In this work we undertook a systematic investigation of the rheology of normal human blood under steady-state shear flow. Based on a comparison between a homogeneous (Couette) and non-homogeneous (Poiseuille) flows, we first showed that the simple flow hypothesis constitutes a reasonable assumption for blood under steady-shear flow with the errors resulting from it in all but one datum being less than 10%. Second, we unequivocally showed that the Casson viscoplastic model is the one that naturally emerges as the best approximation of available experimental data. Third, we developped a parametrization of the Casson model parameters, the yield stress and the Casson viscosity, in terms of parameters that define the physiological state of blood. As a single most important contribution of this work is the realization that yield stress is an onset phenomenon only occurring when the hematocrit exceeds a critical value that depends on the fibrinogen concentration. Most importantly, we have found a simple quadratic relationship that connects the critical hematocrit with the fibrinogen concentration. Albeit the connection of yield stress to fibrinogen (a key plasma protein responsible for the development of red blood cells adhesion) is not new, it is the first time that this is made in such a direct, quantitative, fashion. Furthermore, beyond the onset, the dependence of the yield stress on the hematocrit is found to be through the square of its difference from its critical value, further reinforcing the interpretation of yield stress as a critical, percolation-type, phenomenon.

A word of caution is needed for the applicability of our model. The range of applicability is dictated by the range of experimental results that were used for the development of the parametric equations. For the parameterization of viscosity, the hematocrit ranged roughly from 10% to 60%, while for yield stress the hematocrit varied

between 40% and 80% and the fibrinogen concentration between 0.1 *g/dl* and 0.9 *g/dl*. The fibrinogen content of the capillary data that were used for the parameterization of viscosity was unknown, as was the content of any other plasma macromolecule in any of the data sets used in the fitting of either the viscosity or yield stress. We assumed that both of those unreported quantities were within their physiological range. Based on that information, and under this assumption, the model is most safely applicable for 40%<Hct<60% and $0.1 g/dl < c_f < 0.4 g/dl$, which is where the ranges of parameter values of all used data sets meet. However, as shown in Figure 2.11, Eqs. (2.12) and (2.14) can be successfully extrapolated to predict yield stress measurements in the range 10%<Hct<100%. Therefore, we can safely extend the limits in which our model can be used to 10%<Hct <60% and $0.1 g/dl < c_f < 0.4 g/dl$ and even expect a good fit, based on the smooth fits of Figure 2.9 and the commenting of Figure 2.4 results in Section 2.3.2, for the extended limits of 10%<Hct<80% and $0.1\ g/dl < c_f < 0.7\ g/dl$.

Beyond verifying the proposed model through a comparison of its predictions against the data that we have used for its development, we have extensively validated it against additional data from the literature. The model validation was successful as long as the blood used in the studies was minimally processed and within the physiological range of conditions. In particular, the model predictions were found to be off when compared against data involving red blood cells in other than plasma solutions (such as saline solutions) and/or the blood was drawn from patients with specific illnesses or individuals under various drag regiments. This finding, beyond setting the limits of validity of the proposed parametrization for our model (minimally processed blood, under physiological conditions) it also most definitely points out further to the rheologically complex character of blood. Clearly, one needs to know the fibrinogen

concentration, in addition to the hematocrit, in order to properly characterize the steady-state shear blood flow. Furthermore, it is also clear that more blood ingredients, beyond those used explicitly in our parameterization (i.e. the red blood cells and fibrinogen) play a role in defining the blood flow rheology, even in the limiting case of steady-state shear flows examined here. Although those ingredients have not been explicitly taken into account here (the primary reason being of course the lack of adequate quantitative data) nevertheless they have been present in the blood samples used in the experimental data and therefore they have been considered implicitly, as defining the physiological environment. The fact that when the physiological conditions change we can have significant departures in the steady–state shear blood flow rheology points out to a potential diagnostic application of the present work. Considerable differences between the predicted and experimentally determined viscometric results based on the above analysis provide evidence to a non-physiological, i.e. pathological, behavior (thus suggesting new uses for rheology!). Clearly this is a point worth of further study in the future.

Chapter 3

THE EFFECT OF CHOLESTEROL AND TRIGLYCERIDES ON THE STEADY STATE RHEOLOGY OF BLOOD

3.1 Introduction

In Chapter 2 we established parametric relationships that connect the yield stress and model viscosity appearing in the Casson model to important physiological parameters such as the hematocrit, temperature and the fibrinogen concentration [Apostolidis and Beris (2014)]. These relationships, derived on a large number of available blood flow data from the literature, represent the first improvement over the previously widely used but rather obsolete relations offered by Pries *et al*. (1990). However, those parametric relations were developed and extensively tested for healthy blood and thus are restricted to physiological conditions. There is considerable interest therefore (a) to test those relationships with blood samples of blood indices considerably outside the physiological conditions and (b) to see how, in case those relationships fail to hold, they need to be corrected. This is exactly the subject of the present work focusing on the particular case of high and low cholesterol/trigluceride conditions, exploiting the very recent, well-characterized, available data by Moreno *et al*. (2015).

Cholesterol is a lipid that is produced by the liver and/or found in certain foods [Thiriet (2008)]. Being insoluble to water, it is carried within blood through various transport proteins, the lipoproteins, which are usually distinguished as low, intermediate and high density (or LDL, IDL and HDL). Cholesterol is useful for a variety of important functions, ranging from maintaining healthy cell membranes to building crucial hormones and vitamins [Thiriet (2008)[. At the same time, it is well known that elevated cholesterol levels can increase the risk of several adverse health effects

including atherosclerosis, heart attack and stroke [Cowan *et al*. (2012)]. This is especially true for LDL (also termed "bad cholesterol") as it is associated with the transfer of cholesterol from the liver to the cells. Inversely, high levels of HDL(also termed "good cholesterol") are considered beneficial, as it is associated with the transfer (clearing) of cholesterol from the cells and to have antioxidant and antiflammatory properties [Forti and Diament (2006); Cowan *et al*. (2012)].

. However, although that much is universally accepted, the mechanism through which cholesterol increases the risk of diseases is not well understood or agreed upon. While the mainstream theory considers the accumulation of cholesterol, crossing the endothelial barrier and subsequent oxidation activating the endothelial cells promoting the formation of atherosclerotic plaques as the primary reason [Kwiterovich (2000)], there is also evidence [Kensey (2003); Cowan *et al*. (2012)] and support [Sloop (1996, 1999)] of the hypothesis that it is through the increase in blood viscosity that LDL cholesterol contributes to atherogenesis. Inversely, lowered HDL levels are associated with elevated blood viscosity [Stamos and Rosenson (1999)] and elevated HDL levels are connected to a decrease in blood viscosity (Cowan et al. 2012). This makes the study of the effects of cholesterol to blood viscosity and blood rheology, in general, of considerable medical, as well as rheological, interest. Moreover, elevated levels of triglycerides (the most common form of fats--fatty acid esters--that are circulated within blood, also through lipoproteins, as they are also insoluble to water) are also considered as a factor of increased blood viscosity [Rosenson *et al*. (2002)] and a contributor to cardiovascular disease [Chapman *et al*. (2011)]. Thus, emerges the need to study simultaneously the effect of all those factors, i.e. total cholesterol levels, LDL, HDL and triglycerides, on blood viscosity and rheology.

Although several studies have been dedicated in the past to study the effect of each one of the above factors to blood viscosity, this was so far implemented statistically and for each one of the factors considered separately or at most studied in cross-correlation against another [Koenig *et al*. (1992); Crowley *et al*. (1994); Stamos and Rosenson (1999); Rosenson *et al*. (2002)]. Moreover, the analysis has been limited to the overall blood viscosity at a particular shear rate, or, to the plasma viscosity [Koenig *et al*. (1992)]. It is only with the new rheology study by Moreno *et al*. (2015) that we have full rheological results (viscosity vs shear rates) for fully characterized blood samples, with respect to all the physiological (hematocrit, fibrinogen) but also cholesterol and triglycerides levels and also for samples taken from two populations, exhibiting high and low cholesterol and triglycerides. However, the analysis in Moreno *et al*. (2015), albeit complete from a rheological perspective (three different models were used to fit the data for any particular sample), it still did not address the issue of their parametric dependence effects on all the factors synergistically, but again only on an one by one basis. Moreover, there was no quantitative correlation of the results to those factors except some limited semi-quantitative correlations that, as a result, showed considerable scatter. The most promising results was a close to linear fit of the yield stress (as fit through a Casson model) to the total cholesterol levels. However, even in that case, the discussion as for the procedure used to extract those yield stress values and the fit to the supplied viscosity data was not addressed but only in a couple of cases.

The presence of the previous work [Apostolidis and Beris (2014)], demonstrating the Casson model as the most useful model to describe steady state shear blood rheology, leads naturally to the suggestion of using its two parameters, yield stress and model viscosity, to quantitatively characterize blood viscosity, not only at a specific

shear rate but as a general dependence vs. shear rates, and all this following just two parameters with concrete physical meaning. Especially the yield stress, as it has been connected to the rouleaux aggregates that form between the red blood cells in the flow, becomes the natural way to express the effect of biological factors that influence cell-cell interactions and aggregation to rheology. Moreover, the previously developed parametrization for healthy blood under physiological conditions allows us to accommodate a physically meaningful reference state and therefore it presents a unique opportunity for analysis of pathological effects. Finally, the systematic procedure employed in the previous chapter can also be applied here to eliminate biases in the analysis. This is exactly what we are undertaking here.

The rest of the chapter has as follows. In the next section, the Casson model and the standard parametrization developed in our previous work are summarized. In the section following that, we describe the results of our analysis of the effects of cholesterol and triglycerides on the Casson model parameters based on the Moreno *et al*. (2015) viscosity data. This is followed by our conclusions.

3.2 Model Equations

In our recent investigation [Apostolidis and Beris (2014)], by a careful analysis of existing literature data drawn from healthy individuals, it was shown that:

(1) The simple fluid assumption (i.e. that the rheology can be described based on the local kinematics) is a reasonable working hypothesis for steady shear blood flows, at least when wall effects can be neglected. Thus, the use of a generalized Newtonian model, the most general model for simple fluids in shear flows, is justified.

(2) Among a fairly wide representation of plausible generalized Newtonian model representations, including the power law and the Herschel-Bulkley, Casson and their modifications, the Casson model came us as statistically the one providing by far the best overall fit to a large collection of data. As a reminder, and for future reference, in the Casson model the steady state shear stress, τ, is described for positive shear rates, $\dot{\gamma} > 0$, as [Casson (1959)]:

$$\sqrt{\tau} = \sqrt{\tau_y} + \sqrt{\mu\dot{\gamma}} \ , \ \tau > \tau_y \ , \tag{3.1}$$

where τ_y represents the yield stress and μ is the model viscosity.

(3) For a large number of healthy blood samples with rheological data reported in the literature, which are characterized physiologically by at least the hematocrit, Hct (i.e. the red blood cells (RCB) volume fraction) and the fibrinogen concentration, c_f (in g/dl), the Casson model parameters can be parametrically represented as functions of those parameters and the temperature. In particular, for the yield stress, it is recognized as a critical phenomenon due to the RBC aggregation that is mediated, among other factors not explicitly resolved in this work, through fibrinogen. As a result, it was postulated that, for any given fibrinogen concentration, there is a critical hematocrit, Hct_c, for yield stress phenomena to appear. This critical hematocrit concentration was shown to be provided by the following parametric relation in terms of the fibrinogen concentration, $c_f(g/dl)$, as:

$$Hct_c = \begin{cases} 0.3126{c_f}^2 - 0.468c_f + 0.1764 & c_f < 0.75 \\ 0.0012 & c_f \geq 0.75 \end{cases} . \tag{3.2}$$

For hematocrit values below that critical hematocrit value, Hct_c, there is no yield stress and the blood is assumed to behave like a Newtonian fluid. Above Hct_c the yield stress, $\tau_y(Pa)$, quickly develops as a quadratic function of both the hematocrit and the fibrinogen concentration. Thus, the overall expression developed by Apostolidis and Beris (2014) for the yield stress is:

$$\tau_y = \begin{cases} [(Hct - Hct_c)^2 \times (0.5084 c_f + 0.4517)^2 & Hct > Hct_c \\ 0 & Hct \le Hct_c \end{cases} . \qquad (3.3)$$

Similarly, the following parametric relationship has been developed for the Casson model viscosity in terms of the hematocrit and the temperature:

$$\mu = n_{p0}\left(1 + 2.0703 \times Hct + 3.7222 \times Hct^2\right) \times \exp\left(-7.0276\left(1 - \frac{T_0}{T}\right)\right), \qquad (3.4)$$

where the temperature T is in $^{\circ}K$ and η_{p0}, $\eta_{p0} = 0.00167\ Pa \cdot s$ is the plasma viscosity at the reference temperature $T_0 = 273.16 + 23 = 296.16\ ^{o}K$. Note that the fibrinogen concentration does not enter the viscosity expression. From a rheology perspective, Eq. (3.4), that has been developed from a regression of rheological data, offers good agreement to independent theoretical expectations, such as for example, considering the first, linear, coefficient of proportionality between the relative viscosity μ / η_p, $\eta_p = \eta_{p0} \exp(-7.0276(1 - T_0 / T))$, and the blood hematocrit, Hct, which is the volume fraction of RBC in suspension. With the reported value of 2.0703 being just below the Einstein hard sphere limit (2.5) and right in the range of expectations considering the

deformability and inner viscous internal nature [Vitkova (2008)] of the RBCs [Happel and Brenner (1983)].

The parametrization expressed by Eqs. (3.2)-(3.4) represents what we call here the Basic Reference Physiological Healthy State (BRePHS). As it has been developed for healthy individuals, and only based on hemactocrit and fibrinogen data, it cannot possibly accommodate the effect of significant variations of other parameters, such as cholesterol and triglycerides, of interest to the present work. As we will see this is true not only for pathologically high levels of those factors (expressing a hypercholesterolemia condition) but also, potentially, for low levels, as (when they are excessive, as postulated here) they may also take us beyond the range covered in the samples that led to the BRePHS model. Of course, in this case, the evaluation of the new model applicable for those data, should involve, in principle, a full reparametrization of the Casson model, in terms of all the parameters, i.e. the various indices of cholesterol, and triglycerides, as well as hematocrit and fibrinogen, truly a daunting task. Fortunately, in the present work, the available data been restricted to approximately constant Hematocrit and fibrinogen values allows us to focus our analysis to only the effect of cholesterol and riglycerides that can be safely assumed to be described through a multiplicative factor to Eqs. (3.3) and (3.4), for the yield tress and model viscosity, respectively. Of course, this is only meaningful if the Casson model continues to describe well the steady state blood rheology. This is shown first, followed by the new parametrization, in the following results section.

3.3 Experimental Data

The task undertaken in the present work is the analysis and interpretation of the detailed steady state shear blood rheology results made available in a seminal work by Moreno *et al*. (2015) on well characterized physiologically blood samples taken from two populations, both of high (H) and low (L) cholesterol/triglycerides. Detailed viscosity data were offered in their Figure 1 Moreno *et al*. (2015) for 4 high cholesterol (H1-H4) and 4 low cholesterol (L1-L4) samples. These are the data that we employ also here in our analysis taking also advantage of their detailed physiological evaluation in terms of (a) total cholesterol levels, (TC), triglyceride levels, (TG), low density lipoprotein, (LDL), and high density lipoprotein levels, (HDL), in addition to their hematocrit (Hct) and fibrinogen concentration (c_f). For convenience, those data (the mean values, as the uncertainties, which are also supplied in Moreno *et al*. (2015), are typically fairly small, within less than 5%) are reproduced here in Table 3.1. Note that both the hematocrit and fibrinogen concentration levels varied little both within the H and L groups as well as between the two groups ($Hct = 48 \pm 1\%$ and $c_f = 0.28 \pm 0.01 g/\mathrm{dl}$). This is particularly advantageous as it allows us to focus on the cholesterol and triglyceride effects.

Table 3.1. Clinical data on physiological indices of the blood samples used in the viscosity evaluation study as reported by Moreno *et al*. (2015). The sample notation follows the notation introduced in that work: H1-H4 correspond to high cholesterol/triglycerides; L1-L4 to low cholesterol/triglycerides.

Sample	TC (mg/dL)	TG (mg/dL)	HDL (mg/dL)	LDL (mg/dL)	c_f (mg/dL)	*Hct* (%)
H1	400	250	35.5	135.5	284	48.2
H2	268	157	36.1	130.8	278	47.9
H3	250	187	38.2	139.4	273	48.0
H4	290	160	40.6	149.1	278	47.8
L1	187	180	48.8	159.1	288	48.7
L2	164	122	46.7	148.9	275	48.8
L3	109	130	47.6	146.8	270	49.0
L4	180	145	40.6	144.5	278	47.9

As analyzed by Moreno *et al*. (2015), what one sees in their raw data is a significant variability in blood flow viscosity between the various samples, on top of the (expected) differences between the H and L groups. The variability is such that viscosity levels at any given shear rate can only exhibit certain qualitative trends when plotted in terms of any given factor, with significant variations remaining, of the order 50 – 100%. For example, as seen in Fig. 2 of Moreno *et al*. (2015) when the viscosity at $\dot{\gamma} = 1 s^{-1}$ is plotted as a function of the total cholesterol (TC) levels, whereas there is an overall linearly increasing trend of the viscosity with TC there is still considerable scatter. This scatter is also reminiscent of earlier results reported in the literature, much

more voluminous in size, such as those shown in Fig. 2 of Crowley *et al*. (1994) extracted from a healthy population, as well as in Fig. 1 of Nara *et al*. (2009) obtained with blood samples taken from hypercholesterolaemic subjects. The scatter in these last two studies is further exacerbated from the fact that the data involved concerned more variable hematocrit values as opposed to the Moreno *et al*. (2015) reported cases.

In this respect, the raw data by Moreno *et al*. (2015), in terms of extracting correlations between blood viscosity and TC (or the other factors) little added to the previous information --- such positive correlations were also reported in both the Crowley *et al*. (1994) as well in the Nara *et al*. (2009) studies. More specifically, in addition to the well known correlation of blood viscosity with hematocrit (that our previous study nicely quantified for normal samples), Crowley *et al*. (1994) also detected, again within a normal, healthy population, and in order of decreasing effect, positive correlations between blood viscosity and TC, LDL (almost at the same level, about 1/3 the effect seen with hematocrit) as well as with TG (although about half as strong as the effect with TC, LDL) whereas a negative correlation was noticed with respect to HDL (and almost as strong a magnitude as with TC and LDL). It is interesting that almost exactly the same correlations were also noted in the above-mentioned [Nara *et al*. (2009)] study that also involved hypercholesterolaemic subjects, although there (presumably because of the higher variations) the correlations were twice as strong as those reported by Crowley *et al*. (1994) that involved only healthy subjects, and the correlation with TG was as strong (in fact even slightly stronger) as with TC and LDL. Similar statistical correlations were also reported in several other studies---see, for example, Stamos and Rosenson (1999), Rosenson *et al*. (2002). Still, the same scatter, as well as interrelationships between the various factors involved (as well as also with

hematocrit and fibrinogen that were not as tightly controlled in these studies), prevented a more quantitative analysis.

Still, the Moreno *et al*. (2015) study was unique for one more reason. In addition for offering detailed viscosity results (as well as linear viscoelasticity data) for a number of well-characterized samples, both of low and high cholesterol/triglycerides, they also attempted a rheological fir of the data---several models have been tried, including purely shear thinning (Carreau), viscoplastic [Casson and Quemada—see (Quemada 1978a,b)] and multimode thixotropic-viscoelastic [Bautista-Manero-Puig---see (Bautista et al. 1999)] models. All models appear to be able to fit the data, with suitably selected parameters (with the Bautista-Manero-Puig model, of course, due to its viscoelastic three modes, been able to also fit the linear viscoelasticity data).

However, the most important contribution was the capability to now use model parameters to correlate against the blood flow physiological indices. In that respect, not surprisingly, it was the yield stress parameter of the Casson model that was selected to study. In Fig. 10 of Moreno *et al*. (2015) we see a much better correlation (linear relationship) between the yield stress and the total cholesterol (TC) with significantly less scatter than in the correlation mentioned above involving directly the blood viscosity at $\dot{\gamma} = 1 s^{-1}$. However, only partial Casson data are offered and no quantitative relations were produced. In the following subsection, and starting from the raw blood viscosity data, we reevaluate the Casson fits of the data. Those are compared against the BRePHS model predictions in Table 3.2. Then, in the subsection that follows, we show the development of more quantitative relations, by fully exploring the cholesterol/triglyceride dependencies.

3.4 Casson Model Fits

In Figs. 3.1a,b we show the blood viscosity data of Moreno *et al*. (2015) for High (H) and Low (L) cholesterol/triglyceride levels and their linear fits in the Casson coordinates, i.e. in a $\sqrt{\tau}$ vs. $\sqrt{\dot{\gamma}}$ diagram form. There are several important observations that we can make from Fig. 3.1. First, from the quality of the linear fits we can testify about the appropriateness of the Casson model to represent the blood viscosity data, for the low as well as the high cholesterol/ triglyceride levels alike. Second, we notice that the graphs do not superimpose, despite the fact that they correspond to almost the same hematocrit and fibrinogen levels (as well as temperature, $T = 37\,^{\circ}C$. In fact, there are quite different. Therefore, the BRePHS model, which only involves those parameters—see Eqs. (3.2)-(3.4), cannot possibly explain them.

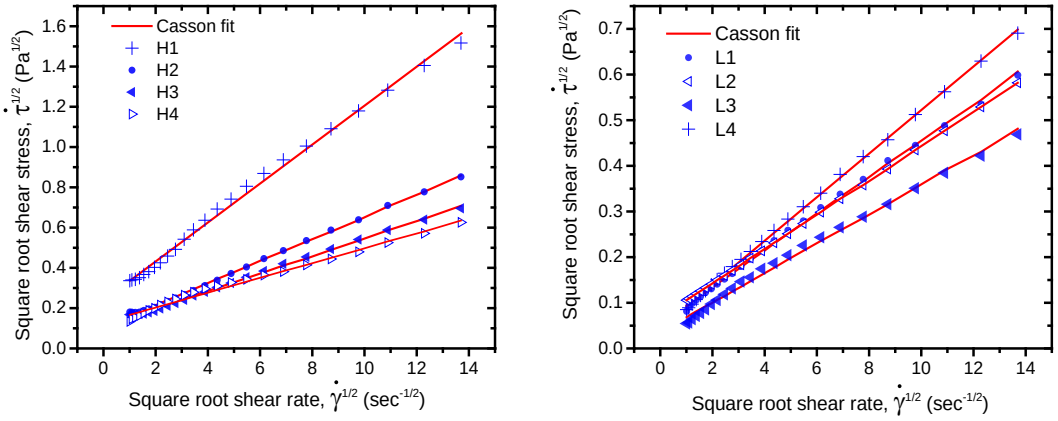

Figure 3.1. Casson plots ($\sqrt{\tau}$ vs. $\sqrt{\dot{\gamma}}$) of four high cholesterol/triglyceride data samples (symbols, as indicated by H1-H4 in graph (a)) and four low cholesterol/triglyceride data samples (symbols, as indicated by L1-L4 in graph (b)),

and their corresponding best linear (Casson) fits (continuous lines) corresponding to the H1-H4 and L1-L4 viscosity vs. shear rate data of Figure 1 of Manero *et al*. (2015). The corresponding Casson model parameters are indicated in Table 3.2.

Table 3.2. Casson model fitted parameters (the yield stress, τ_y , and the viscosity, μ) to the blood samples viscosity data reported in Figure 3.1 of (Moreno *et al*. 2015). The BRePHS model predictions, and their ratios are also shown.

Sample	τ_y	$\tau_{y\text{BRePHS}}$	r_y	μ	μ_{BRePHS}	r_μ
	(Pa)	(Pa)	(-)	(Pa s)	(Pa s)	(-)
H1	0.0568	0.0605	0.939	0.00935	0.00348	2.69
H2	0.0111	0.0585	0.190	0.00290	0.00346	0.838
H3	0.0125	0.0579	0.216	0.00149	0.00347	0.429
H4	0.0167	0.0582	0.287	0.00136	0.00345	0.394
L1	0.00287	0.0627	0.0458	0.00129	0.00352	0.366
L2	0.00458	0.0605	0.0757	0.00141	0.00352	0.401
L3	0.00126	0.0602	0.0209	0.00104	0.00354	0.294
L4	0.00203	0.0585	0.0347	0.00227	0.00346	0.656

As seen in Table 3.2, there is a significant variation on the individual Casson model parameter values (i.e. the yield stress and the viscosity) between the samples. In the same table we have also listed the values corresponding to the BRePHS model predictions. Not surprisingly, given the closeness in the hematocrit and fibrinogen

values between the various sample, the BRePHS predictions show much smaller differences between the different samples. Thus, there are quite significant differences between the actual fitted values of the Casson model parameters to the experimental data and their BRePHS predictions. A measure of that difference is further obtained by evaluating the yield stress ratio, $r_y \equiv \tau_y / \tau_{\text{yBRePHS}}$ and the viscosity ratio, $r_\mu \equiv \mu / \mu_{\text{BRePHS}}$ which are also shown in Table 2. The substantial deviation of these ratios from 1 is at first glance quite astonishing.

On the other hand, neither the deviation from one of those ration, nor their variations from sample to sample should be surprising given the large variations reported for these samples regarding the various cholesterol and triglycerides levels, as seen in Table 3.1. Indeed, the strong effect of cholesterol and triglycerides on blood viscosity, albeit so far mostly qualitative, has been well documented, as mentioned above in many references (Crowley et al. 1994, Stamos and Rosenson 1999, Rosenson et al. 2002, Nara et al. 2009) well before the (Moreno et al. 2015) data appeared. However, as the biological effect that causes these changes to the blood rheology are still unknown (at least on a quantitative fashion, suitable for modeling) we will attempt to capture those effects phenomenologically, parametrically and separately for each one of the two Casson model parameters, the yield stress and the Casson viscosity, in the two sections that follow. For that task, we will be taking advantage of the detailed information offered in the (Moreno et al. 2015) about the blood samples physiological characterization, as reproduced in Table 3.1..

3.4.1 Cholesterol/Triglycerides effects on yield stress

The effect of cholesterol/triglycerides on the yield stress of blood was also attempted to be captured by Moreno *et al*. (2015) in their seminal work by trying to correlate their yield stress fitted values to the total cholesterol levels, and that correlation appeared to be very well represented by a simple linear relationship---see Fig. 11 in Moreno *et al*. (2015). However, (a) the fit had some scatter around this linear proportionality average and (b) their reported yield stress values were at considerable disagreement from the values obtained in the present work---compare the reported values for samples H1-H4 in Table 3 of Moreno *et al*. (2015) to those that appear in Table 3.2 in this work. Most importantly, when we attempted to represent our own reported yield stress values as a function of the total cholesterol levels, the relationship appeared significantly more complicated with the data much more scattered---see Fig. 3.2. Thus a different modeling approach is warranted.

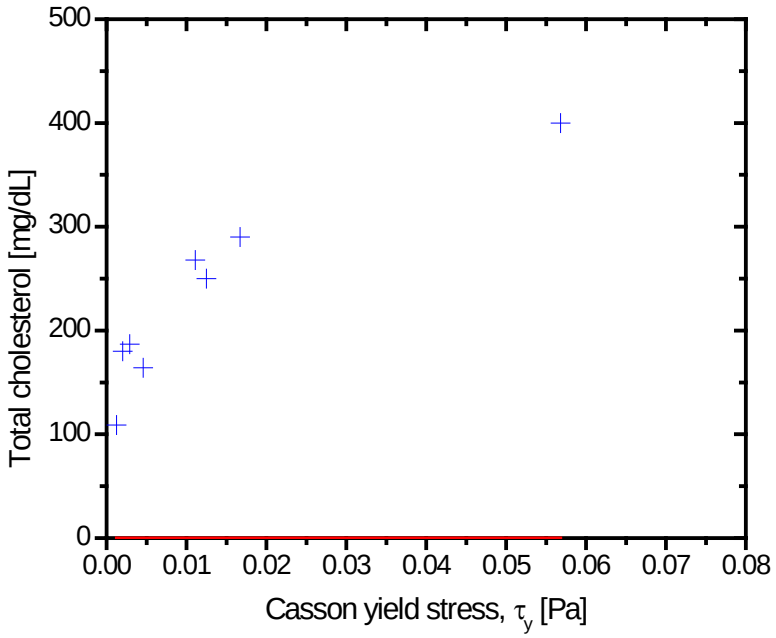

Figure 3.2. Total cholesterol (in mg/dL) of the samples as a function of the Casson yield stress values (in Pa)

To be able to better explain the obtained data, we looked more carefully on evidence from the medical literature as for the most significant indices that medically make sense to use in order to judge the effect of cholesterol and triglycerides in blood. It appears that there is growing support to the opinion that it is not the absolute values of any of the indices (TC, TG, LDL, HDL). Rather, one should look at the ratios TC/HDL, LDL/HDL and TG/HDL (Mercola 2012). Still, when a direct linear regression of the data was attempted, the results appeared not very well quantitatively explained.

At the end, what worked, was a simple two-prong process. First, the yield stress data were regressed as a function to the TC/HDL ratio. Astonishingly, a strong quadratic correlation $r_y \propto \left(TC/HDL\right)^2$ appeared! Then, the yield stress ratio weighted by $\left(HDL/TC\right)^2$ was considered with respect to the remaining two indices, LDL/HDL and TG/HDL. What then became obvious is that there is a fairly different behavior between the high (H series, considered here when LDL/HDL > 3.623) and the low (L series, considered here when LDL/HDL < 3.623) cases. In the first, a critical behavior was exhibited very clearly between the weighted yield ratio and LDL/HDL manifested with a linear relationship with respect to the square root of the departure of LDL/HDL from its critical value, 3.623---see Fig. 3.3a. In contrast, for the second case, what correlated the weighted yield stress perfectly was the TG/HDL ratio, with a quadratic relationship allowing for a clear minimum (sweet value?) at TG/HDL=3.25---see Fig. 3.3b.

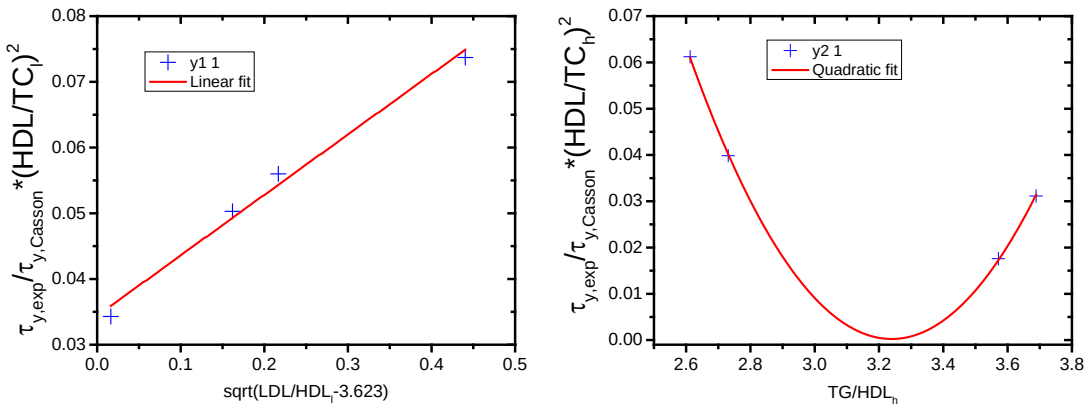

Figure 3.3. Weighted yield stress ratio, $r_y\left(HDL/TC\right)^2$, as a function of (a) $\sqrt{\left(LDL/HDL-3.623\right)}$ (for H samples, $LDL/HDL \geq 3.623$) or (b) TG/HDL (for L samples, LDL/HDL < 3.623).

Those results can be summarized to the following expression for the yield stress ratio:

$$r_y = \left(\frac{TC}{HDL}\right)^2 \times \begin{cases} 0.0344 + 0.092\sqrt{\left(\frac{LDL}{HDL}\right) - 3.623} & \left(\frac{LDL}{HDL}\right) \geq 3.623 \\ 1.6216 - 1.001\left(\frac{TG}{HDL}\right) + 0.1545\left(\frac{TG}{HDL}\right)^2 & \left(\frac{LDL}{HDL}\right) < 3.623 \end{cases} . \quad (3.5)$$

How well can the expanded model proposed here through Eq.(3.5), together with the BRePHS model, predict the observed yield stress? To answer that we show in Fig. 3.4 the expanded model vs. the fitted Casson yield stress values. As it can be seen from there, the agreement is excellent.

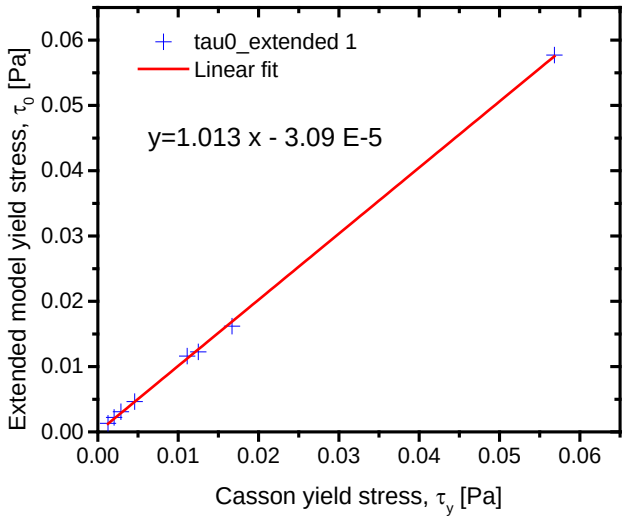

Figure 3.4. Comparison of the extended model predictions against the experimental data fitted values for the yield stress for the eight samples, H1-H4 and L1-L4 corresponding to the viscosity data of Figure 1 of (Moreno et al. 2015).

All resulting fits appear to be consistent with the anecdotal evidence that we have from the literature on the cholesterol/triglycerides effects to the blood flow rheology: i.e. that the (apparent) viscosity of blood increases as either TC, LDL or TG increase, but is the opposite, i.e. it decreases, with increasing HDL. Indeed, Eq. (3.5) implies exactly those effects to the yield stress, and if the yield stress increases, the apparent viscosity also increases (at least for low shear rates---for higher shear rates, one needs to see what happens to the model viscosity as well). What is of interest is that now we have specific quantitative expressions for those effects and in terms of a concrete physical parameter (the yield stress) instead of a rather vague "(apparent) viscosity" that may also (and it does) have a shear rate dependence. Moreover, we

noticed that they are ratios that are of importance, rather than absolute values—that seems to be now the feeling in the medical community regarding the medical evaluation of cholesterol and triglyceride effects (Mercola 2012).

Given the small number of samples, we feel that the particular quantitative details maybe off; however, we tend to believe that certain qualitative characteristics, certainly the dependence on ratios as well as the fact the dependence on the yield stress on the TC/HDL is through its second power, may be generic and more reproducible. Here, as before in Apostolidis and Beris (2014) (also supplied here as Eq. (3.3)), in the parametric expressions for the stress we see second powers which may be revealing on the criticality of the phenomena (here as then) giving rise to the yield stress. The fact that the dependences observed are so strong and that yield stress is significantly increased in association to increased TC, LDL cholesterol levels and triglycerides (respectively, decreased in association to increased HDL levels) may also be explained in terms of our ideas on the influence of cholesterol and triglycerides to the cell membrane proteins, adhesion and interactions of the membrane with the cytoskeleton (Sun et al. 2007). Of course we are far away from a priori explanation of those effects and more work is definitely warranted but the present results may provide some evidence supporting such a path through which cholesterol can influence the blood rheology

3.4.2 Cholesterol/Triglycerides effects on Casson viscosity

The examination of the effect of cholesterol/triglycerides on the Casson model viscosity followed a similar path to that described to the yield stress. Namely, first we regressed the observed viscosity ratios (as shown in the last column of Table 3.2) against

the TC/HDL ratio. In this case, two different linear relationships emerged, depending on whether we considered high cholesterol/triglyceride (H series, considered here when LDL/HDL > 3.623) or low (L series, considered here when LDL/HDL < 3.623) cases:

$$r_\mu \approx \begin{cases} 0.5\left(\dfrac{TC}{HDL} - 5.93\right) & \left(\dfrac{LDL}{HDL}\right) \geq 3.623 \\ \dfrac{1}{8}\left(\dfrac{TC}{HDL}\right) & \left(\dfrac{LDL}{HDL}\right) < 3.623 \end{cases} . \tag{3.6}$$

However, as before, the above relations are highly approximate and there is a considerable scatter in the data present. To remove that, again, as in the case of the yield stress before, we seek correlations of the differences with respect to the other relevant ratio, TG/HDL. In this case, what we found that it worked the best was the correlation of the inverse weighed viscosity ratio, or normalized fluidity, φ^* , with TG/HDL, where the normalized fluidity is defined, based on the regression shown in Eq. (3.6), as:

$$\varphi^* \approx \begin{cases} 0.5\left(\dfrac{TC}{HDL} - 5.93\right)\dfrac{1}{r_\mu} & \left(\dfrac{LDL}{HDL}\right) \geq 3.623 \\ 0.123\left(\dfrac{TC}{HDL}\right)\dfrac{1}{r_\mu} & \left(\dfrac{LDL}{HDL}\right) < 3.623 \end{cases} . \tag{3.7}$$

Those correlations are shown in Figs. 3.5a and 3.5b for the high and low cholesterol/triglyceride cases, respectively. As it can be seen from there, they can very well be represented by quadratics, similar to the case shown in Fig. 3.3b.

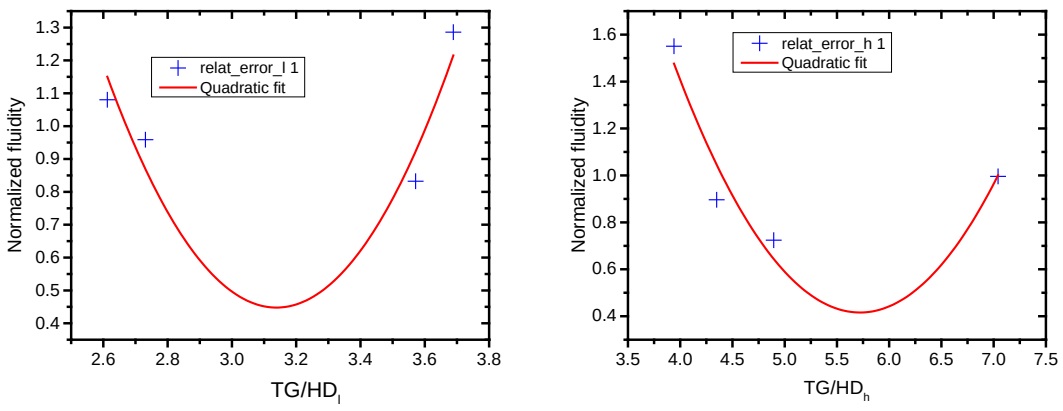

Figure 3.5. Normalized fluidity, φ^* (as defined in Eq. (3.7)) as a function of TG/HL for (a) L samples, LDL/HDL < 3.623) and (b) H samples, $LDL/HDL \geq 3.623$.

The results can be summarized to the following expression for the Casson model viscosity ratio:

$$r_\mu = \begin{cases} \dfrac{0.5\left(\dfrac{TC}{HDL} - 5.93\right)}{11.37 - 3.83\left(\dfrac{TG}{HDL}\right) + 0.3348\left(\dfrac{TG}{HDL}\right)^2} & \left(\dfrac{LDL}{HDL}\right) \geq 3.623 \\ \dfrac{0.12315\left(\dfrac{TC}{HDL}\right)}{25.443 - 15.928\left(\dfrac{TG}{HDL}\right) + 2.5374\left(\dfrac{TG}{HDL}\right)^2} & \left(\dfrac{LDL}{HDL}\right) < 3.623 \end{cases} . \quad (3.8)$$

How well can the expanded model proposed here through Eq. (3.8), together with the BRePHS model, predict the observed Casson model viscosity? To answer that we show in Fig. 3.6 the expanded model vs. the fitted Casson model viscosity

values. As it can be seen from there, the agreement is very good with the emerging linear fit almost coinciding with the identity map and the scatter minimal.

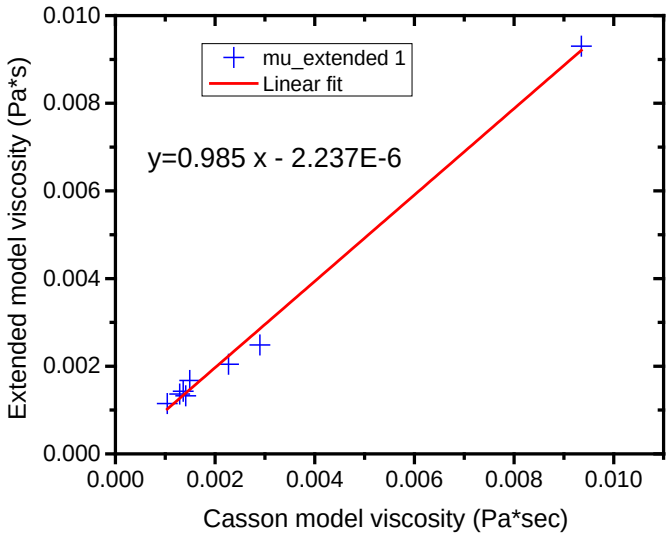

Figure 3.6. Comparison of the extended model predictions against the experimental data fitted values for the Casson model viscosity for the eight samples, H1-H4 and L1-L4 corresponding to the viscosity data of Figure 1 of Moreno *et al*. (2015).

In this case we also feel that the most important item is that the reported results on model viscosity, that showed significant deviations from the reference values of the previously established parametric relations of the BRePHS model, can also be fit through relations to the same ratio of indices, and not their absolute values. The results are also a bit surprising in that they tend to show (in all but one case) that the model viscosity is actually reduced as a consequence to cholesterol/triglyceride effects. Again

the number of data is small to be able to draw firm conclusions but the indications are that it may be that the model viscosity effect is a result of a model compensation to the very strong effect on the yield stress and to the model nonlinearity. It certainly makes the case that the data on yield stress and mode viscosity need to be examined and interpreted in combination rather than in isolation. Once more, additional data are necessary before we can draw more concrete conclusions.

3.5 Conclusions

In this work we presented a first attempt to quantitatively rationalize on the very significant effects that the cholesterol and triglycerides have on the steady state shear rheology of blood. We show that these effects are considerable and modify the parameterization description provided in our previous work (Apostolidis and Beris 2014) in a very significant way. However, despite their significant effect, as a positive result, the Casson model remains a very good model for the steady state shear blood rheology. That limits the need of the investigation in expressing the changes needed to predict the Casson model parameters, i.e. the yield stress and the Casson model geometry. In the present work we showed how the same ratios that physicians have found to be of importance in assessing the risks of hypercholesterolemia and hypertriglycerolaemia also seem to be important in assessing the cholesterol and triglyceride effects on blood rheology. This provides indirect evidence on the value of the hypothesis that cholesterol and triglycerides when in excess they contribute to cardiovascular diseases primarily because they increase blood viscosity (Sloop 1997). Inversely, the natural emergence of certain ratios in the viscosity and yield stress

correlations, such as LDL/HDL = 3.623, and TG/HDL = 3.2 point out to naturally emerging target values that may end up having future medical significance.

The rheology of biofluids and blood in particular, proves to be a very complex phenomenon due to the presence of many constituents with complex interconnections. The need for further microscopic and biological investigations on the underlying phenomena that eventually lead to rheological changes is very high. However, this undertaking will take time to be completed, given the underlying complexity of the phenomena. In the mean-time, phenomenological relations may play a role in modeling and simulations. Even those, they require very extensive physiological evaluations of the blood samples used in the measurements. The present work due to the many factors involved and the relatively small number of available data cannot claim to have provided strong relations that can be used for a priori predictive purposes. In all likelihood the results are limited to the particular cases studied as other factors, not explicitly accounted for (such, for example, other proteins in blood, as albumin) may also play a key role in establishing blood's rheological behavior. However, we strongly believe on the robustness of the most important conclusions, i.e. the demonstration that (a) the Casson model appears to hold even under pathological conditions and that (b) key ratios of importance to medical diagnosis, emerged naturally in the investigation as the most sensitive factors controlling blood rheology as well. This close connection of rheology to pathology is the most important contribution of the present work and one that may have significant repercussions in the future.

Chapter 4

MODELING OF HUMAN BLOOD RHEOLOGY IN TRANSIENT SHEAR FLOWS

4.1 Introduction

As a dense suspension of deformable red blood cells (RBCs), as well as leucocytes and platelets, in plasma, an aqueous solution of proteins, blood rheology is characterized by a complex, viscoplastic and thixotropic, non-Newtonian behavior [Cokelet *et al*. (1963); Dintenfass (1962); Merrill (1969)]. At low shear rates RBCs tend to aggregate, via the bridging of fibrinogen, into column structures (rouleaux), thus giving rise to the experimentally measured blood yield stress [Merrill *et al*. (1969); Picart *et al*. (1998)]. However, this process is shear-rate dependent, as the rouleaux structures disintegrate when they are deformed by the flow. The reversibility of this process, that is the ability of RBCs to aggregate and disagregate, explains the shear-thinning character of blood. Moreover, this process is time-dependent as the rouleaux structures form and dissolve at differing time scales, which are also flow-dependent, thus attributing to blood a time-dependent (apparent) viscosity and thus, thixotropy [Owens (2006)].

A significant effort has focused on the steady state shear blood flow behavior, as discussed at length in our recent publication [Apostolidis and Beris (2014)]. In that previous modeling work we showed how, based on a systematic study of available steady state shear data, the Casson viscoplastic model emerges naturally as the most suitable one to describe the blood rheology in steady state shear. The most important findings of those steady state experimental blood flow investigations were: the exhibition of yield stress [Cokelet *et al.* (1963); Chien *et al.* (1966); Merrill (1969);

Merrill *et al.* (1963, 1965)], the correlation between yield stress and the plasma fibrinogen concentration [Merrill *et al.* (1969); Morris *et al.* (1989)], the existence of a critical hematocrit [Meiselman *et al.* (1967); Merrill (1969); Merrill *et al*. (1963)], i.e. the demonstration for the existence of a threshold concentration of RBCs in the suspension in order for blood to exhibit a yield stress, and the transition from non-Newtonian to Newtonian flow in high shear rates [Merrill and Pelletier (1967)]. With the exception of the last one, our previous steady state model was able to account for all other effects successfully [Apostolidis and Beris (2014)]. Furthermore, the most significant contribution of that work was the development of parametric relationships expressing the dependence of the Casson model parameters (i.e. the Casson model viscosity and yield stress) on physiological conditions such as the hematocrit (Hct), the fibrinogen concentration in plasma (c_f), and the temperature (T).

However, the steady state shear behavior clearly represents a limiting case. In particular, the yield stress in dense soft colloidal suspensions, of which blood is one example, is typically attributed to an internal structure that develops, deforms and decays in a way that depends critically not only on the current flow kinematics but also on its history, thus giving rise to thixotropy [Mewis (1979); Barnes (1997); Mewis and Wagner (2012)]. Thus, while the study of steady state shear flows gave important insight into the non-Newtonian, viscoplastic, characteristics of blood, it is only the study of transient and time-dependent behavior that can allow for the system to exhibit its most complex, thixotropic and viscoelastic, rheological properties. Some of the most commonly employed methods to probe those properties are the use of triangular steps of shear rate (hysteresis experiments) and the application of oscillatory flow [Mewis and Wagner (2012)]. Only few experimental investigations have been so far devoted to

the description of these transient blood flow characteristics, and it would be safe to claim that the matter has not received the appropriate amount of attention, given the sparseness of results that have been reported so far. Some of the pertinent experimental investigations that need to be distinguished are those of Bureau *et al.* (1979, 1980), who systematically obtained, using a coaxial cylinder microviscometer, hysteresis and step-up curves of pathological and physiological human blood. Other important contributions on the experimental investigation of the viscoelasticity of human blood have been provided by Thurston (1972, 1975, 1976) who performed oscillatory flow experiments in cylindrical tubes. Moreover, in a recent study Sousa *et al.* (2013) were only the first to obtain whole blood Large Amplitude Oscillatory Shear (LAOS) data, reinforcing the notion that the transient rheology of blood has not been explored in depth. The evidence supplied in these studies provides useful information that can be used for validation purposes of blood flow models in the transient shear regimes.

Some of the most sophisticated non-Newtonian blood flow models have been developed in the last decade by Owens and coworkers [Fang and Owens (2006); Moyers-Gonzalez *et al.* (2008a, 2008b); Moyers-Gonzalez and Owens (2008);Owens (2006); Owens *et al.* (2008)]. In the first of these models, an attempt was made to take into account, through a set of viscoelastic phenomenological equations extracted through a polymer network theory analog, the aggregation and disaggregation of the erythrocytes [Owens (2006)]. This model was subsequently applied to simple shear flows [Owens (2006)] as well as to steady, oscillatory and pulsatile flow in rigid vessels [Fang and Owens (2006)]. Later, Moyers-Gonzalez *et al*. (2008a) developed a further refinement of that model to take into account inhomogeneous erythrocyte concentrations due to stress-induced migration, following the modeling described in

earlier work by Beris and Mavrantzas (1994). This allowed for the description of the Fahreus and Fahreus-Lindquist effects thereby the local hematocrit and the apparent blood viscosity, respectively, decrease with tube diameter, for sufficiently small vessels [Truskey *et al*. (2009)]. These sophisticated models have improved the modeling of the non-Newtonian blood flow, however, due to their viscoelastic origin they cannot explicitly account for a yield stress, the most important manifestation of the viscoplastic nature of blood.

Another remarkable attempt to describe general blood flow, this time through a generalized Oldroyd-B model, was made by Anand and Rajagopal (2004). This model, which was developed in the context of the general thermodynamic framework of Rajagopal and Srinivasa (2000), has been shown to produce results that correlate well with the steady state simple shear data of Yeleswarapu (1996) and the oscillatory tube flow data of Thurston *et al*. (1975). The authors [Anand and Rajagopal (2004)] claimed that the model can also describe the rheological hysteresis curves of Bureau *et al*. (1980), however such a comparison was not shown. Anand *et al*. (2013) further refined that work by accounting for a finite zero shear rate viscosity and by allowing for a smooth variation of viscosity at very low shear rates. These changes improved the numerical stability of the model when used in the simulations of straight and bent cylindrical tubes. In the same investigation, the model is used to fit the hysteresis data of Bureau *et al.* (1980), however the validation in transient shear flows is incomplete as the comparison was done only against one of the rheograms presented in the work of Bureau *et al*. (1980). Moreover, as also it was the case with the models referenced in the previous paragraph, these works of Anand and Rajagopal (2004) and Anand *et al.*

(2013) make use of a tensorial viscoelastic model and therefore do not explicitly take into account the viscoplastic nature of blood.

Unlike the general viscoelastic descriptions mentioned in the two previous paragraphs, thixotropic models account explicitly for the exhibited yield stress in viscoplastic systems. The most common thixotropic models are so far phenomenological, based on a constitutive equation that links a rheological stress response to a given level of microstructure, the latter being expressed by means of a scalar structural parameter [Mewis and Wagner (2012)]. Thixotropy is then accounted for via the time evolution equation of the structural parameter that is assumed to obey a relaxation equation with terms accounting both for the structural buildup as well as for the shear-induced structural breakdown. Modeling thixotropic systems, even at a phenomenological level, is still one of the most challenging problems in suspension rheology. The works of Mujumdar *et al*. (2002) and Dullaert and Mewis (2006) have provided some of the most popular structural models that have been successfully used to model thixotropic systems, while a comprehensive overview on the matter has been offered by Mewis and Wagner (2012). In the case of blood, however, despite its viscoplastic nature, there have been no attempts to describe systematically its transient rheology through a purely thixotropic model. To the best of our knowledge, the only model able to describe the thixotropy in blood, and therefore able to account explicitly for the exhibited yield stress, is the one proposed by Sun and De Kee (2001). The specific system, a first order kinetic model with a structural parameter, was developed to describe the flow of a wide class of materials, including biofluids. This model was shown to produce results that agree well both with steady state [Chien *et al*. (1971)] and transient [Bureau *et al*. (1980)] blood data. However, as first pointed out by Owens

(2006), there are questions related to the exact form of the model equations used and the parameters corresponding to these results. Furthermore, a fundamental pitfall pertaining to this, as well as all other modeling investigations of transient shear blood flow so far, is the lack of a systematic approach.

In the present paper we offer a systematic study of the rheology of blood in transient shear flows, based on a structural thixotropic model, fully capitalizing on the findings and the parametric relations of our previous steady-state viscoplastic shear flow model. The model developed in this work is a single scalar internal structural parameter thixotropic model, based on the model developed in our earlier work [Mujumdar *et al.* (2002)]. It has also been suitably modified to (a) exploit recent advances based on the kinematic hardening model of the elastic strain in plasticity theory [Dimitriou *et al.* (2013)] and (b) enforce the constraint that it reduces to the Casson model in steady state shear flows, at least for low shear rates. This constraint helped the present investigation in two significant ways. First, it allowed the selection of the proper forms in the evolution equation for the structural parameter as well as in the stress constitutive model so that this constraint is satisfied exactly, at least in the limit of low shear rates. Second, given this reduction, it allowed the full use of the previously developed and thoroughly tested parametric dependences. As a result, the new, extended, model proposed in the present work has only four additional parameters, of which one can be fit by looking at any deviations from the Casson steady state behavior realized at higher shear rates, such as those reported in Merrill and Pelletier (1967). Moreover, by using these data, the model can explain for the first time theoretically this effect that, albeit it has been observed a long time ago, has not as yet been theoretically understood. To fit the remaining three model parameters, all of which have concrete physical meaning and

tight limits, we used the transient data reported by Bureau *et al.* (1980) involving triangular changes in shear, at a slow shear rate transient shear flow. Furthermore, we systematically evaluated the model performance in additional, triangular changes in shear transient shear flow performed at a higher shear rate, as well as in step-up and step-down shear [Bureau *et al.* (1979)] all of them collected with the same blood samples. Finally, we also compared the predictions of our model against recent whole blood flow LAOS results [Sousa *et al.* (2013)]. Our aim is to model bulk phenomena in geometries of dimensions significantly larger to the diameter of the red blood cells, and for short times that do not facilitate significant concentration inhomogeneities. Thus we treat blood phenomenologically as a rheologically homogeneous medium.

The remaining sections of the paper are organized as follows. In the next section, Sec. II, we systematically develop the model equations, starting with a review of the steady state Casson model, to which the transient model reduces exactly in steady state simple shear flows at low shear rates. In Sec. III we show our results and discussion, starting with the high shear rate steady state behavior, and then presenting all the transient shear results, first those used to fit the model parameters and then the rest used for model validation. The final section, Sec. IV, presents our conclusions.

4.2 Model Equations

The starting point for the transient model development is the constraint that for steady-state shear flows it reduces to the Casson model, for which our previous work [Apostolidis and Beris (2014)] (a) has shown to arise naturally from the consideration of previous literature data and (b) has developed expressions for its model parameters

in terms of physiological parameters. For completion, we review the final results from this analysis.

4.2.1 Overview of the steady state model

Following the Casson model (1959), the steady state shear stress τ_s is described for positive shear rates $\dot{\gamma}_s > 0$ as:

$$\sqrt{\tau_s} = \sqrt{\tau_y} + \sqrt{\mu \dot{\gamma}_s} \ , \ \tau_s > \tau_y \ , \tag{4.1}$$

where τ_y represents the yield stress and μ the model viscosity. Apostolidis and Beris (2014) developed parametric expressions for the model parameters in terms of the physiological blood parameters, namely the blood hematocrit, *Hct*, the fibrinogen concentration, c_f, and the temperature, *T*, as follows. First, the yield stress parametric form is given as:

$$\tau_y = \begin{cases} [(Hct - Hct_c)^2 \times (0.5084 c_f + 0.4517)^2 & Hct > Hct_c \\ 0 & Hct \le Hct_c \end{cases} , \tag{4.2}$$

where the yield stress, τ_y, is in $dyne/cm^2$ and the fibrinogen concentration, c_f, in g/dl, and Hct_c represents the critical hematocrit value for yield stress given as:

$$Hct_c = \begin{cases} 0.3126 {c_f}^2 - 0.468 c_f + 0.1764 & c_f < 0.75 \\ 0.0012 & c_f \ge 0.75 \end{cases} . \tag{4.3}$$

Second, the viscosity parametric form is given as:

$$\mu = n_p\left(1+2.0703\times Hct+3.7222\times Hct^2\right)\times\exp\left(-7.0276\left(1-\frac{T_0}{T}\right)\right), \qquad (4.4)$$

where T_0 is the reference temperature of 273.16+23=296.16 ^oK (at which the plasma reference viscosity $n_p = 1.67\times10^{-2}\ dyne\times s/cm^2$ is measured), and T is the blood absolute temperature (in ^oK). An extensive verification and validation of the proposed model is presented in Apostolidis and Beris (2014).

4.2.2 Development of a thixotropic model for transient shear blood flow

The development of the fully time-dependent thixotropic model for blood is based on a single scalar structural parameter thixotropic model---see, for example, Mewis and Wagner (2012) and references therein. These models attempt to describe thixotropy (i.e. the dependence on the deformation-history in viscoplastic materials) phenomenologically by expressing the parameters of inelastic viscoplastic equations (such as the Bingham or Hershel Bulkley models [Bird *et al.* 1987)] parametrically in terms of a scalar structural parameter λ. For example, the shear stress can be represented in a shear flow (assuming, for simplicity, a positive shear rate $\dot{\gamma}$) as a linear superposition of the yield stress and a viscous contribution as [Mewis and Wagner (2012)]:

$$\tau = \lambda\tau_y + \left(1-\lambda\right)K\dot{\gamma}^n. \qquad (4.5)$$

In turn, λ is assumed to obey a relaxation evolution equation that, in addition to a relaxation term back to its static equilibrium value (typically taken as 1) also includes a flow-induced structure breakdown term [Mewis and Wagner (2012)]:

$$\frac{d}{dt}\lambda = k_1\left(1-\lambda\right) - k_2\dot{\gamma}\lambda\,, \tag{4.6}$$

where k_1 and k_2 are rate coefficients describing the recovery of the structure and the shear induced break down, respectively. A further development on these structural thixotropic models was made when the elastic contribution to the shear stress (i.e. the term $\lambda\tau_y$ in the stress Eq. (4.5)) was substituted by a modulus $G = G(\lambda)$ times an elastic strain γ_e:

$$\tau = G(\lambda)\gamma_e + \left(1-\lambda\right)K\dot{\gamma}^n\,. \tag{4.7}$$

In turn, $G(\lambda)$ was postulated to have a certain functional relationship whereas the evolution of the elastic strain was described in terms of the imposed strain rate. The details vary depending on the model. For the "Delaware model", developed by Mujumdar *et al*. (2002) for a thixotropic concentrated ceramic suspension, we have:

$$\frac{d}{dt}\gamma_e = \begin{cases} \dot{\gamma} & \left|\gamma_e\right| < \gamma_{\max}(\lambda) \\ 0 & \left|\gamma_e\right| = \gamma_{\max}(\lambda) \end{cases} \tag{4.8}$$

where $\gamma_{\max}$ is the upper limit of the sustained elastic strain within the material. As the structure breaks down this limit may change and it is represented within the model as a power law with respect to the structural parameter:

$$\gamma_{\max}(\lambda) = \gamma_0\lambda^m \tag{4.9}$$

where γ_0 is the zero shear rate elastic strain and m is an exponent characteristic to the material. The "Delaware model" predicts that the elastic strain increases as the material is strained from rest until it reaches the critical limit strain, $\gamma_{\max}$, thus reaching the yield point. Past the yield point, the elastic strain follows the critical strain in the post-yield phase.

Finally, the "Delaware" model introduces a functional relationship for the dependence of the elastic modulus on the fluid's structure:

$$G(\lambda) = G_0 \lambda , \tag{4.10}$$

where G_0 is the zero shear rate value of the modulus.

We have used the "Delaware model" as a prototype to model the thixotropic blood rheology, through suitable modifications and extensions. We first implemented an improvement on the elastic strain evolution equation extending that developed by Dimitriou *et al.* (2013) based on the kinematic hardening theory of plasticity. First, the total strain is assumed to be decomposed into the sum of an elastic and a plastic part:

$$\gamma = \gamma_e + \gamma_p \Leftrightarrow \dot{\gamma} = \dot{\gamma}_e + \dot{\gamma}_p . \tag{4.11}$$

Second, the rate of change of the elastic strain is determined, following a straightforward extension of the kinematic hardening model [Dimitriou *et al.* (2013)] to allow for a variable maximum elastic strain, as

$$\dot{\gamma}_e = \dot{\gamma}_p - \frac{\gamma_e}{\gamma_{max}} \left| \dot{\gamma}_p \right| , \tag{4.12}$$

where γ_{max} represents the maximum allowed elastic strain. For the blood flow model we propose the following relationship

$$\gamma_{max} = \min\left(\frac{\gamma_0}{\lambda^2}, \gamma_\infty\right), \tag{4.13}$$

where γ_0, γ_∞ are two dimensionless parameters representing the zero-shear rate and infinite shear rate limiting values for the maximum elastic strain supported within the material, respectively. Note that as λ, the structural parameter characterizing the material, varies between the 1 and 0 limits, achieved at the zero-shear rate and infinite shear rate limiting values, respectively, the γ_∞ value is necessary in order to avoid allowing unrealistically high (even infinite!) values for the elastic strain within the material at high shear rates. The values for $\gamma_0 < \gamma_\infty$ are expected to range between order 0.01 and 1, roughly.

If Eq.(4.12) is now substituted into the second one of Eq.(4.11) we can get the relationship between the rate of change for the plastic strain and the shear rate:

$$\dot{\gamma}_p = \begin{cases} \dfrac{\dot{\gamma}}{\left(2 - \dfrac{\gamma_e}{\gamma_{\max}}\right)} & \dot{\gamma} \geq 0 \\ \dfrac{\dot{\gamma}}{\left(2 + \dfrac{\gamma_e}{\gamma_{\max}}\right)} & \dot{\gamma} < 0 \end{cases}. \tag{4.14}$$

Second, based on this elastic-plastic strain decomposition, we replaced the previous stress equation, Eq. (4.7), by one relating the shear stress, τ, to the elastic

strain, γ_e, and the plastic strain rate, $\dot{\gamma}_p$. For blood, which behaves like a Newtonian viscous fluid in the limit of high shear rates this leads to:

$$\tau = G\gamma_e + \mu\dot{\gamma}_p, \tag{4.15}$$

where *G* represents a structure-dependent elastic modulus which now is assumed to obey a relaxation equation:

$$\frac{d}{dt}G = \frac{\tau_0}{\mu}k_G\lambda\left(G_e - G\right), \tag{4.16}$$

where τ_0 is the zero shear rate yield stress of the material

$$\tau_0 \equiv G_0\gamma_0, \tag{4.17}$$

and G_e represents an equilibrium value assumed to depend proportionally to a structural parameter λ and its zero shear rate value G_0:

$$G_e = \lambda G_0, \tag{4.18}$$

and where k_G is a dimensionless, order 1, kinetic coefficient. Note that from this equation the modulus of elasticity is assumed to relax to its equilibrium value based on a characteristic rate that changes, as the equilibrium modulus value in Eq.(4.18), i.e. at a rate proportional to the structural parameter λ.

The last, and probably most important, of the governing equations for the transient blood behavior is that corresponding to the relaxation of the λ structural parameter. This is assumed to follow a modified relaxation equation:

$$\frac{d}{dt}\lambda = \frac{\tau_0}{\mu} k_\lambda \left((1-\lambda) - \lambda \sqrt{\frac{4\mu\dot{\gamma}_p}{\tau_0}} \right), \tag{4.19}$$

where k_λ a dimensionless kinetic parameter characterizing the structural rebuild, of order 1. Note that, in Eq. (4.19), the square root dependence on the (plastic) shear rate, as well as the ratio of the kinetic coefficients for the breakdown vs. rebuild (represented by the term $\sqrt{\frac{4\mu}{\tau_0}}$) are so chosen so that the following steady state simple shear flow solution for λ, λ_s is obtained by zeroing the left hand side of Eq. (4.19):

$$\lambda_s = \frac{1}{\sqrt{\frac{4\mu\dot{\gamma}_s}{\tau_0}} + 1}, \tag{4.20}$$

When this solution is introduced into the constitutive relations for G_e and γ_{max}, Eqs. (4.18) and (4.13), respectively, and those in turn are substituted into the constitutive equation for the shear stress, Eq. (4.15), the Casson model expression, Eq. (4.1), arises naturally, provided that $\frac{\gamma_0}{\lambda^2} \le \gamma_\infty \Leftrightarrow \sqrt{\frac{4\mu\dot{\gamma}_s}{\tau_0}} \le \sqrt{\frac{\gamma_\infty}{\gamma_0}} - 1$ (see Appendix A).

What we see therefore is that, at the end, the proposed thixotropic model satisfies the constraint that it reduces to the Casson model only for small shear rates where the

above inequality is satisfied. Indeed, the full steady state simple shear flow solution for the shear stress that is obtained is given by the following expression:

$$\sqrt{\tau_s} = \begin{cases} \sqrt{\tau_0} + \sqrt{\mu}\sqrt{\dot{\gamma}_s}\,; & \sqrt{\dfrac{4\mu\dot{\gamma}_s}{\tau_0}} < \sqrt{\dfrac{\gamma_\infty}{\gamma_0}} - 1 \\ \sqrt{\left(\dfrac{\tau_0}{\sqrt{\dfrac{4\mu\dot{\gamma}_s}{\tau_0}} + 1} \dfrac{\gamma_\infty}{\gamma_0} + \mu\dot{\gamma}_s \right)}\,; & \sqrt{\dfrac{4\mu\dot{\gamma}_s}{\tau_0}} \geq \sqrt{\dfrac{\gamma_\infty}{\gamma_0}} - 1 \end{cases} . \qquad (4.21)$$

Note that this leads asymptotically at high shear rates to a Newtonian behavior with the same viscosity as the Casson model viscosity. This deviation from the Casson model behavior is unavoidable as long as one has a finite magnitude infinite shear strain, γ_∞, which, however, is the only natural solution. Therefore, what we find is that the introduction of a finite magnitude infinite shear rate elastic strain in Eq. (4.13), which is necessary in order to avoid an unnatural infinite elastic strain within the material, also distorts the equilibrium value of the structural λ parameter, offered by Eq. (4.20) and from there the steady simple shear flow solution.

However, rather than being a model deficiency, as it turns out, this issue develops as a distinct model advantage, as a closer look at the previous literature indicates that such departures from the Casson model behavior have been previously experimentally observed [Merrill and Pelletier (1967)]. In fact, our model offers the first theoretical explanation of such effects. Simultaneously, when these higher shear rates experimental results are taken into account they can be used to fit the ratio γ_∞ / γ_0 in addition to the Casson model parameters (τ_0, μ)---see next section. Thus, at the end,

the proposed thixotropic model introduces only three additional parameters on top of those that can be determined solely from steady state experiments: One dimensionless strain, γ_0 and two dimensionless kinetic coefficients, k_L, k_G . To determine these one needs to use some transient shear data, as shown in the next section.

4.3 Results and Discussion

Comparison of the model predictions to steady state and selective transient data are needed in order to fit the model parameters and validate its performance. For low shear rate steady state simple shear flows one can further take advantage of the parameterization of the Casson model parameters in terms of physiological data, as developed in Apostolidis and Beris (2014), also shown in Eqs. (4.3) and (4.4). That leaves the steady state simple shear flow behavior at higher shear rates (which is needed for the determination of the ratio γ_∞ / γ_0) as shown in section A below. Then, selective, low shear rate transient shear flow data are used in Section 4.3.2 for determining the three additional thixotropic model parameters, dimensionless strain, γ_0 and two dimensionless kinetic coefficients, k_L, k_G . In the same section, comparison of the model predictions to the experimental data based on those parameter values, as well as to additional transient data, are used to determine the model verification and validation, respectively.

This effect, though explicitly emphasized in an early experimental investigation (Merrill and Pelletier, 1967), it has so far been neglected from a theoretical point of view. To the best of our knowledge, there have been no attempts to explain or predict,

under steady state flow, the transition from a Casson to a Newtonian behavior. As mentioned in the previous section, this feature arises naturally as a consequence of the physical picture (from the finite magnitude of the elastic strain) associated with the proposed thixotropic model. In fact, as seen in Fig. 1 where a comparison of a fit with $\gamma_\infty/\gamma_0 = 100$ to the original Merrill and Pelletier (1967) data is shown, the proposed model not only predicts the deviation from the Casson flow behavior at high shear rates and the transition to a Newtonian behavior qualitatively, but also quantitatively.

4.3.1 Steady state simple shear flow: Deviation from the Casson flow behavior at high shear rates

This effect, though explicitly emphasized in an early experimental investigation (Merrill and Pelletier, 1967), it has so far been neglected from a theoretical point of view. To the best of our knowledge, there have been no attempts to explain or predict, under steady state flow, the transition from a Casson to a Newtonian behavior. As mentioned in the previous section, this feature arises naturally as a consequence of the physical picture (from the finite magnitude of the elastic strain) associated with the proposed thixotropic model. In fact, as seen in Fig. 4.1 where a comparison of a fit with $\gamma_\infty/\gamma_0 = 100$ to the original Merrill and Pelletier (1967) data is shown, the proposed model not only predicts the deviation from the Casson flow behavior at high shear rates and the transition to a Newtonian behavior qualitatively, but also quantitatively.

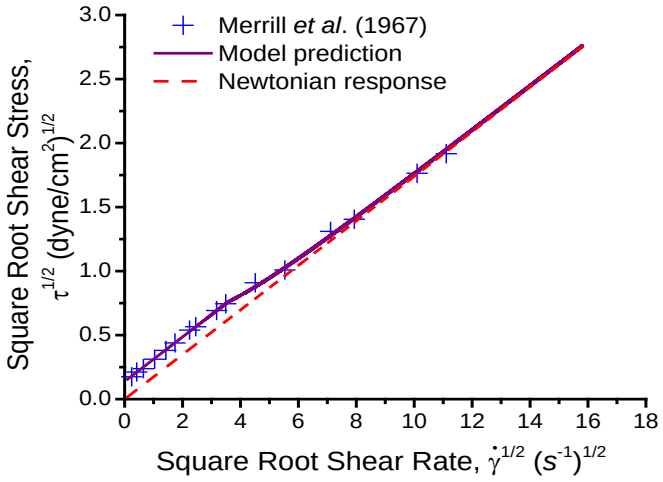

Figure 4.1. Steady state Couette viscometry data of Merrill et al. (1967) (Hct 45%, temperature 37 °C, fibrinogen concentration 0.27 g/dl) vs. our updated steady state model predictions. The transition from the Casson to Newtonian viscosity starts at shear rate ~20 s^{-1}. The dashed line represents the Newtonian response.

4.3.2 Transient shear flow

With the consideration of the high shear rate steady state simple shear flow data, the thixotropic model adds only 3 new parameters (γ_0 or γ_∞, $k_{L,}$ and k_G). In the absence of steady state data, as mentioned above, Eqs. (4.3) and (4.4) can be used for the determination of the zero shear rate yield stress and the Casson viscosity parameters, τ_0 and μ, respectively. However, note that this assumes that all the relevant physiological parameters, i.e. the hematocrit (Hct), fibrinogen concentration (c_f) and the temperature are known. In principle, they are measurable quantities and should be

normally reported with all blood flow related studies. However, when some of these parameters are not reported, as is often the case with the fibrinogen concentration, then these are treated as fitting parameters (within a physiological range of variation).

In the following, the proposed model is used to describe experimental shear data emanating from the following transient shear protocol: a triangular step change in shear rate (hysteresis data) [Bureau *et al.* (1980)], a rectangular step change [Bureau *et al*. (1979)], and LAOS [Sousa *et al*. (2013)]. Bureau *et al*. (1979, 1980) have studied the response of specific normal blood samples subjected to both types of step change rheological experiments. This is important from a modeling point of view, as it poses the constraint of fitting the two sets of experimental data with the same model parameters.

4.3.3 Blood hysteresis in triangular change in shear rate experiments

The variation of shear rate in this type of experiments can be described through a set of linear equations:

$$\begin{cases} \dot{\gamma} = \alpha t, & for\ 0 < t < t_m \\ \dot{\gamma} = \alpha\left(2t_m - t\right), & for\ t_m < t < 2t_m \end{cases}. \tag{4.22}$$

Bureau *et al*. (1979, 1980) have shown that the shape of the hysteresis curves observed in the measured shear stress depends sensitively on the two experimental parameters: the rate of change of shear rate (α) and the duration of shear in each direction (t_m). Based on this observation, Bureau *et al*. (1979, 1980) chose two sets of parameters for the examination of all blood samples, leading to two types of rheograms, A and B (see Fig. 4.2). The investigators examined both pathological and physiological

cases and in each case the respective set of rheograms was reported. Here we use three sets of rheograms, all corresponding to normal (physiological) human blood. For each set of parameters defining the triangular change in shear rate, that is (α, t_m) in Eq. (4.22) , a comparison between the experimental data obtained from each one of the three normal blood samples shows that there is significant variability in the reported results---see Fig. 4.2.

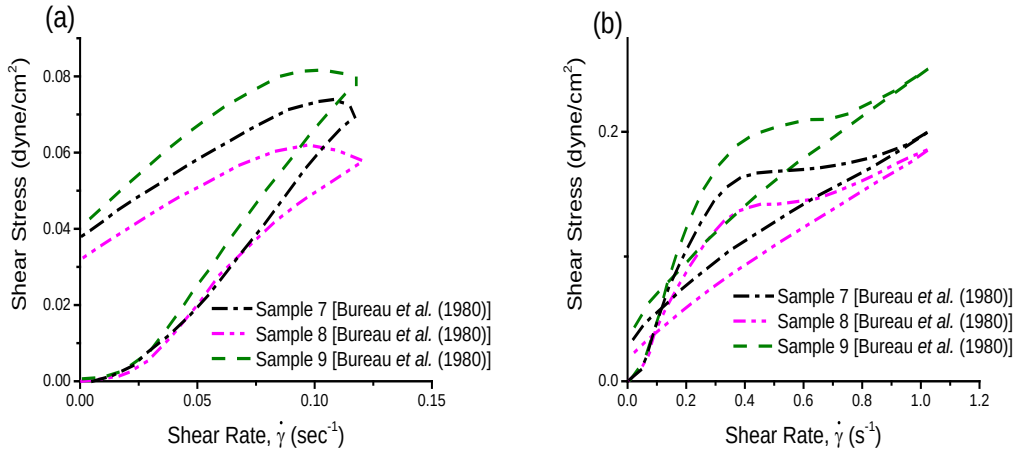

Figure 4.2. Hysteresis curves of three normal blood samples obtained by Bureau *et al*. (1980) corresponding to a triangular change in the shear rate following Eq. (4.22) . (a) Type A rheogram (α =0.0185 sec^{-2}, t_m =6.5sec), (b) Type B rheogram (α =0.043sec^{-2}, t_m =23.8 sec). The hematocrit of each sample was adjusted at 0.45 and the measurements were done at T=25 $\pm$ 0.5 ^{o}C. The numbering of the samples in the legends corresponds to the figures from which the raw data where drawn from, in the original work of Bureau *et al*. (1980).

We postulate that the variability shown in rheological responses of different normal blood samples in Fig. 4.2 is due to the different physiological parameters of each

sample. Since for all cases the hematocrit was adjusted to 45% and the temperature of all measurements was also the same, then the physiological parameter of importance is the protein content, and in particular the fibrinogen concentration. While it is possible that other proteins, such as the immunoglobulins, or acute phase proteins [Weng *et al.* (1996)], impact the rheology of blood, our model accounts only for the fibrinogen concentration.

In order to compare our model predictions to the reported set of hysteresis curves, we first fit the rheogram A data for each blood sample and then, using the same model parameter values, we predict the respective rheogram B data. The fit of the rheogram A data is a non-linear parametric fit which is based on a global optimization routine that has been developed by Armstrong *et al.* (2014). This analysis was done for all three data sets appearing in Fig. 4.1. In Fig. 4.3 the fits for sample 8 and sample 9 are shown. The results were very similar for sample 7 (data not shown).

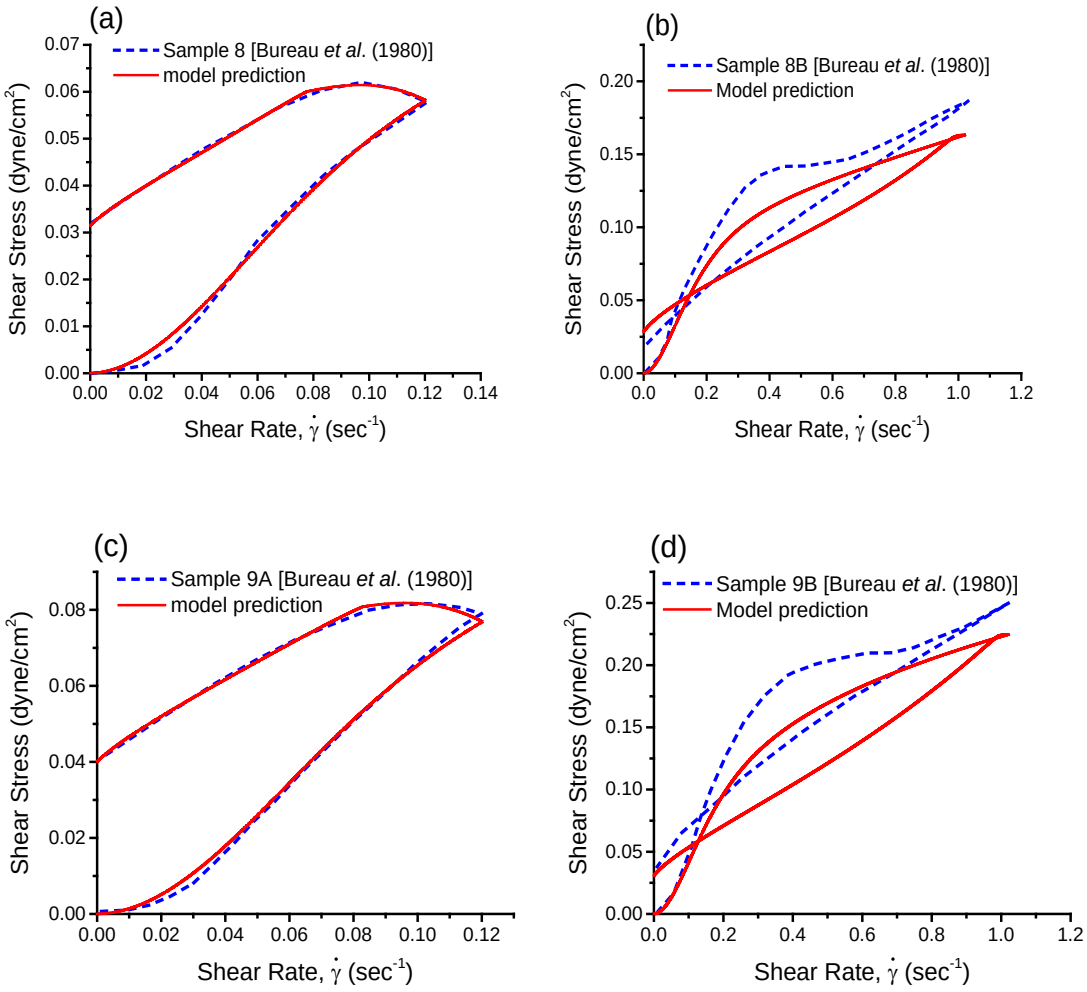

Figure 4.3. Comparison of model predictions (continuous lines) against experimental hysteresis data (dashed lines) of normal human blood, $Hct = 0.45, T = 25°C$. Following Eq. (4.20) the experimental parameters are (a), (c): Type A rheogram (α =0.0185 sec^{-2}, t_m =6.5sec); (b), (d): Type B rheogram (α =0.043sec^{-2}, t_m =23.8 sec). The model parameters used to fit the data were: (a)-(b): Sample 8 of Bureau *et al*. (1980), $c_f = 0.125,\ \gamma_0 = 0.039,\ k_\lambda = 1.214,\ k_G = 0.595$; (c)-(d): Sample 9 of Bureau *et al*. (1980), $c_f = 0.173,\ \gamma_0 = 0.039,\ k_\lambda = 1.207,\ k_G = 0.216$.

The fibrinogen concentration values of the blood samples that have been used in the investigation of Bureau *et al*. (1980) were not reported. As a result, c_f was used here as an additional fitting parameter in the thixotropic model. In addition, since no steady state data were reported for any of the blood samples, a $\gamma_\infty / \gamma_0 = 100$ was used that was obtained from the steady state stress vs shear rate data of another normal blood sample (see Fig. 4.1). In any case, in the present experiments, since the values of the elastic strain were always modest, and if we accept that they remain below γ_∞ (which it is always the case for $\gamma_\infty / \gamma_0 = 10$ or higher) its exact value plays no role in the model predictions.

For both sets of data in Fig. 4.3 the model describes accurately the rheogram A data, while the correlation with the rheogram B data is lower. This is the case for sample 7 as well (data not shown). This consistent difference in the quality of the fit can be explained by the fact that the rheogram B data correspond to, on the average, higher shear rate values, i.e. to conditions under which one expects additional nonlinearities to kick-in that our simple model cannot capture. In principle, we could improve the fitting by introducing higher nonlinearities into the model, but this would have only come at the expense of introducing additional parameters. In any case, at higher shear rates one anticipates that the isotropicity assumption for the samples structure, which is implicit to the use of a single, scalar, internal structural parameter, starts to fail.

Despite these shortcomings, we feel that the model, in addition to being able to fit the lower shear rate data almost exactly, it also captures well all the significant trends seen in the experiment upon increasing the shear rate. In particular, the dramatic shape changes seen between rheograms A and B are predicted with just three additional

parameters over those needed for the steady state and only requiring the data from rheogram A to fit those extra parameters. Furthermore, comparing the fitted parameter values between samples 8 and 9, it is worth noting that (a) the fitted values to the fibrinogen concentration ended up well within the allowed physiological range (0.1 to 0.4 g/dl) and (b) out of the other three transient parameters, one ended up with exactly the same value for both samples (the zero shear rate maximum elastic strain $\gamma_0 = 0.039$) and of the right physical magnitude (a few percent), another ended up to have very close, order one, values (the dimensionless kinetic coefficient for the structural parameter, $k_\lambda = 1.214$ or 1.207), and only the third showed some significant variation, (the dimensionless kinetic coefficient for the elastic modulus relaxation $k_G = 0.595$ or 0.216), still without deviating more than a factor of 5 from unity. In retrospect, it makes sense to see the most sensitivity to the parameter associated with the elasticity of the sample, as (a) this is expected to be affected the most by the difference seen in the fibrinogen concentration values, as fibrinogen is implicated in regulating the forces between the red blood cells and their aggregation which is ultimately responsible for the viscoplasticity of blood and (b) other proteins, whose concentration may also have been different between the two samples, may also be implicated in controlling the relaxation of the elastic modulus and thus k_G.

Overall, it was very encouraging to find naturally, through the fitting process, those reasonable parameter values. Still, as we can see from Fig. 4.3, they were able to (a) fit almost exactly the low shear rate hysteresis curves (rheogram A) and (b) show the trends correctly observed upon increasing the shear rate (and getting a hysteresis curve of very different shape, that corresponding to rheogram B). Furthermore, the small variations in parameter values were sufficient to explain the significant variations

seen between different samples (see Fig. 4.2). Those differences are to be attributed to a great extent to natural differences observed in normal blood at the fibrinogen concentration levels, without also excluding the possibility that for the transient blood flow behavior, other proteins, beyond fibrinogen, may also play a role. This clearly points to the need for a much better characterization of the blood samples used in rheological experiments.

An advantage of possessing a mathematical model for the structure development and rheological response is that one can use it after fitting the data to further analyze the observed response and thus improve the understanding of the underlying mechanisms. In particular, the use of a thixotropic viscoplastic model, like the one suggested in this investigation, allows to probe further the shear stress development in terms of analyzing it into its natural constituents, namely its elastic and viscous contributions. This is exactly what is shown in Fig. 4 where the time evolution of the total shear stress, as well as that for its elastic and viscous contributions, are offered over the total time of the experiment for both rheograms A and B. For brevity, only the results from the modeling one of the samples shown in Fig. 4.2 (sample 8) are shown; very similar results are obtained with the other samples. As we can see in Fig. 4.4, in both experiments the stress contribution is predominantly elastic. This is more the case in Fig. 4.4a than in Fig. 4.4b as the maximum shear rate for rheogram A is 0.12 s^{-1} as opposed to the 1 s^{-1} in rheogram B where the viscous stress contribution is significantly enhanced. Comparing the two contributions, it is instructive that the viscous one in both rheograms is symmetric, linearly increasing with shear rate, as it should, based on the constitutive equation used, Eq. (4.15). The elastic stress response is more nonlinear, distinctly asymmetric, and showing a history dependence that makes it is the source of the

observed hysteresis. Nevertheless, in both rheograms, the elastic stress also assumes its maximum at the maximum shear rate.

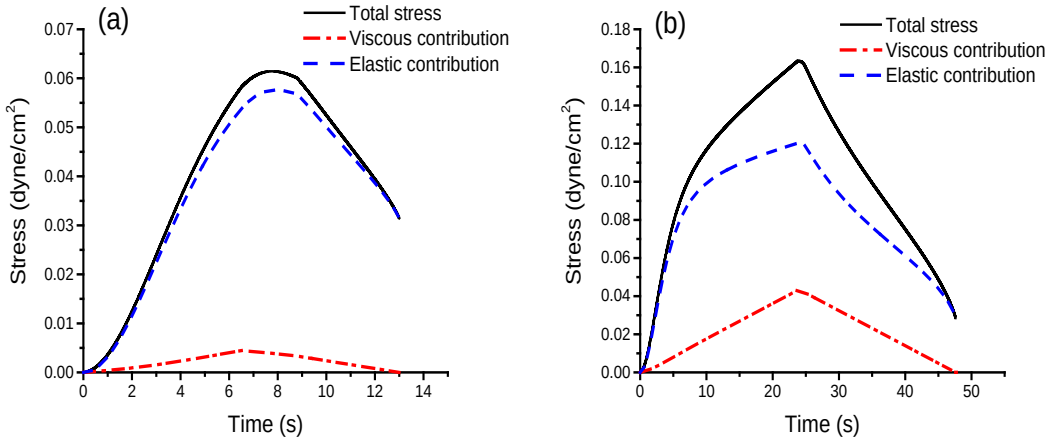

Figure 4.4. Model predictions for the elastic stress, the viscous stress and the total stress response of the normal blood sample 8 as a function of time in (a) rheogram A, corresponding to Fig. 3 (a), and (b) rheogram B, corresponding to Fig. 3 (b). The experimental conditions and the model parameters used are those indicated in Fig. 3.

To further understand how those asymmetric and history-dependent elastic stresses develop it is of interest to examine the development over time of their constituents, i.e. the elastic strain and the modulus of elasticity. Those are shown in Fig. 4.5 and Fig. 4.6, respectively. There we see the effects of the flow. First, as far as the elastic strain is concerned, this is almost symmetric, increasing with increasing time up to the time the maximum shear rate is reached, and then decreasing afterwards. In contrast, the modulus of elasticity shows a distinct asymmetry while it keeps decreasing

(albeit by a smaller relative rate as the increase observed in elastic strain) almost through the whole triangular change in shear experiment. Furthermore, as rheogram B corresponds to higher shear rates we see larger changes in both the elastic strain and modulus.

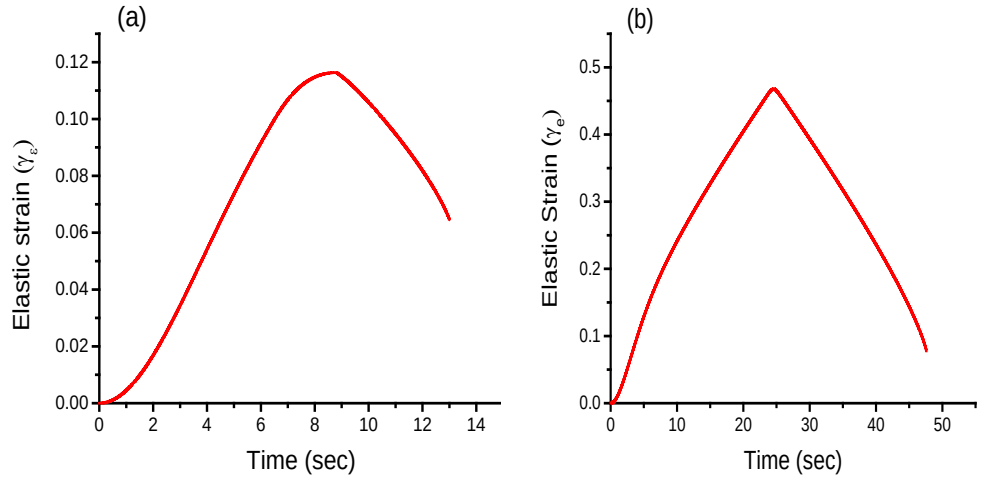

Figure 4.5. Model predictions for the time evolution of the elastic strain γ_e during the hysteresis experiment of sample 8 in (a) rheogram A and (b) rheogram B. The experimental conditions and the model parameters used are those indicated in Fig. 4.3(a) and 4.3(b), respectively.

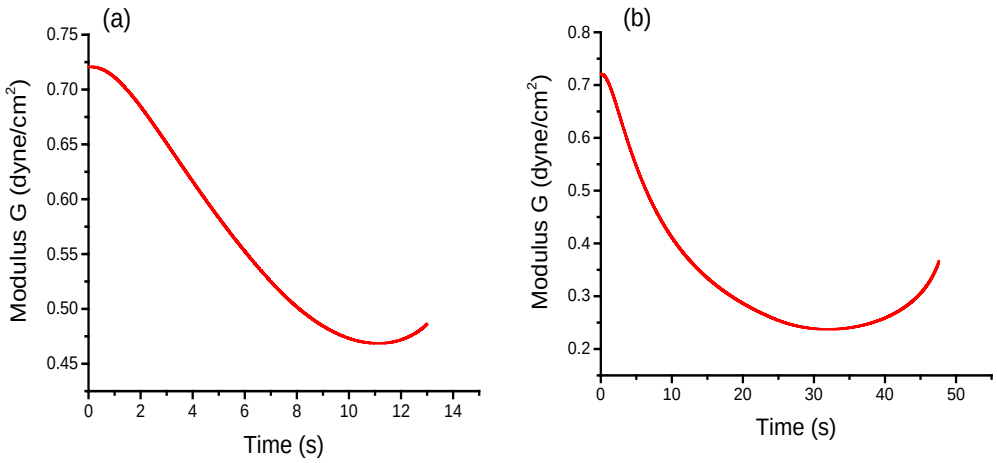

Figure 4.6. Model predictions for the time evolution of the modulus G during the hysteresis experiment of sample 8 in (a) rheogram A and (b) rheogram B. The experimental conditions and the model parameters used are those indicated in Fig. 4.3(a) and 4.3(b), respectively.

To further understand the observed changes in the elastic strain and the modulus of elasticity it is instructive to follow the changes in the structure. This is possible as the thixotropic model involves the λ structural parameter, ranging from the value of 1 (for a virgin structure) to 0 (for a fully broken structure obtained in the limit of high shear rates). Thus, following the evolution in time of the structural parameter in Fig. 4.7 below allows us to evaluate changes in the structure during the triangular change in shear hysteresis experiments. As we can see in Fig. 4.7 there are significant differences between the two rheogram experiments. As the maximum shear rate for rheogram A is 0.12 s^{-1}, as opposed to the 1 s^{-1} in rheogram B, the structural parameter in A assumes larger values (closer to the virgin sample). While

in both cases the structural parameter achieves its minimum value close to the maximum shear rate, achieved in the middle of each experiment, the variation is more asymmetric in the first case (low shear rates) than in the second (higher shear rates). This asymmetry in the structural parameter, caused by the relaxation-type evolution of the structure, in connection to the relaxation-type helps explain the previously seen in Fig. 4.6 asymmetry in the modulus that in turn helps explain the strong hysteresis of the stress observed in Fig. 4.3.

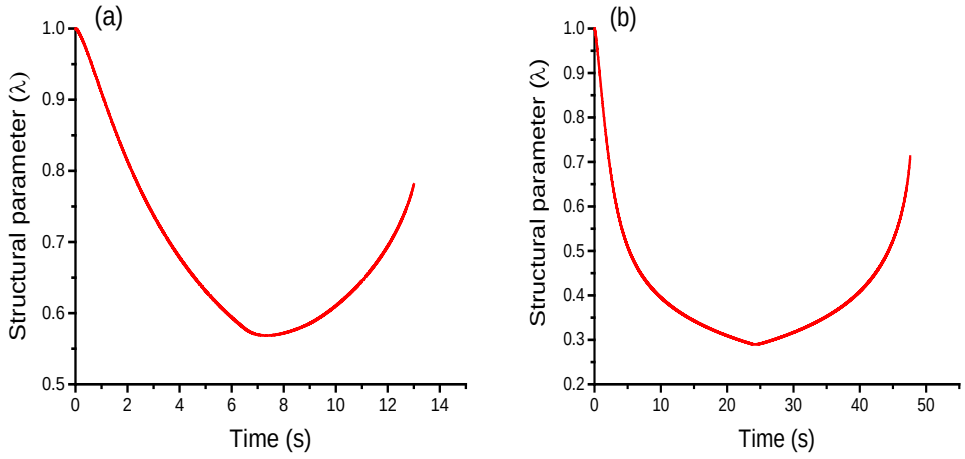

Figure 4.7. Model predictions for the time evolution of the structural parameter λ during the hysteresis experiment of sample 8 in (a) rheogram A and (b) rheogram B. The experimental conditions and the model parameters used are those indicated in Fig. 3(a) and 3(b), respectively.

4.3.4 Rectangular step-change in shear-rate experiments

In addition to the triangular change in shear rate hysteresis experiments, in an earlier work Bureau *et al.* (1979) have also studied the rheological response of normal and pathological human blood to step-change in shear rate experiments. As with the case of the hysteresis experiments, the investigators subjected each sample to two step-changes of different magnitude; a 0.05 s^{-1} and 1 s^{-1} shear rates were applied, leading to the formation of two types of rheograms, rheogram I (see Figs. 4.8a & 4.8c) and rheogram II (see Figs. 4.8b & 4.8d), respectively. The notation of the type of rheograms (e.g. Rheogram I or II) and the numbering of the samples in Fig. 8 corresponds to the annotation used in the original work by Bureau *et al*. (1979).

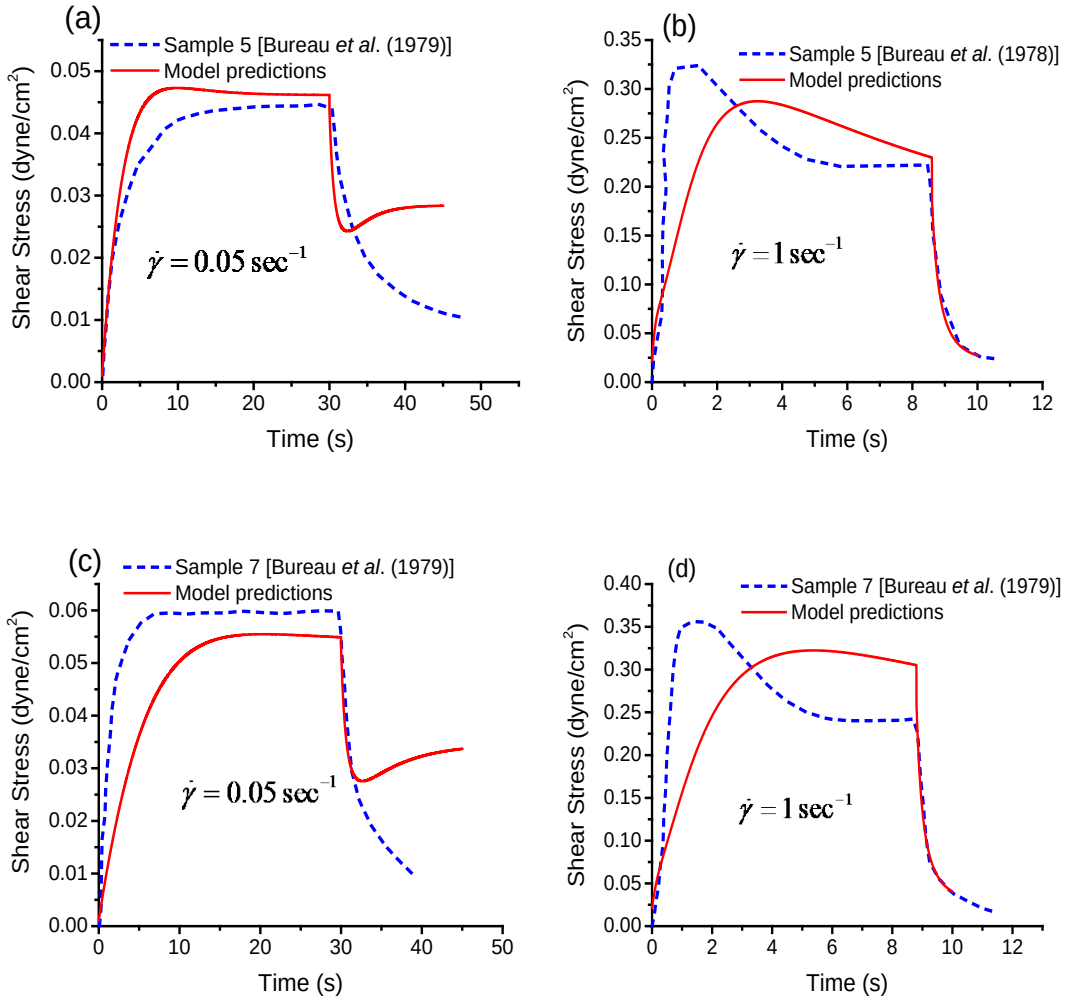

Figure 4.8. Comparison of model predictions (continuous lines) against experimental step-change in shear rate data (dashed lines) of normal human blood, $Hct = 0.45, T = 25°C$. Starting from rest, the final shear rate values are (a), (c): Type I rheogram, $\dot{\gamma} = 0.1\ s^{-1}$; (b), (d): Type II rheogram, $\dot{\gamma} = 1\ s^{-1}$. Samples 5 and 7 from [Bureau *et al*. (1979)] correspond to samples 8 and 9 from [Bureau *et al.* (1980)] and therefore the model predictions are based on the same parameters as

those used in Fig. 4.3: (a)-(b): $c_f = 0.125,\ \gamma_0 = 0.039,\ k_\lambda = 1.214,\ k_G = 0.595,$ $\gamma_\infty = 1$, (c)-(d): $c_f = 0.173,\ \gamma_0 = 0.039,\ k_\lambda = 1.207,\ k_G = 0.216,\ \gamma_\infty = 1.$

Each set of rheograms presented in Fig. 4.8 corresponds to data collected from the same human blood sample that was respectively used to obtain the two sets of hysteresis curves in Fig. 4.3. More specifically, sample 8 in Fig. 4.3 consists of the same blood as sample 5 in Fig. 4.8, and sample 9 in Fig. 3 is the same as sample 7 in Fig. 4.8. Therefore, the data in Fig. 4.8a-4.8b were compared against model predictions which were based on same parameters to those that were obtained from the fit of the data shown in Fig. 3a. Similarly, we compare the experimental data of sample 7 to the model predictions obtained with the parameters from the fit of sample 9 data shown in Fig. 4.3c.

As it can be seen from Fig. 4.8 we do get a semi-quantitative agreement in all cases: At the lower shear rate, the model predictions for both samples are monotonically increasing until saturation in the step-up case, as are the experimental data. Similarly, at the higher shear rate, the model predictions show an overshoot as the steady state results are approached and so do the data. However, there are also quantitative differences. Those need to be explained by the fact that we have opted, for the sake of simplicity and in order to minimize the number of adjustable parameters, to use the simplest possible expressions for the various material functions. Furthermore, note that at the end of the experiments (relaxation after the shear rate is decreased to zero) the model predictions are very good. Some discrepancies observed there at the later stages of the relaxation process in association with the lower shear rate experiment (Figs. 4.8a and 4.8c) need to be attributed to experimental artifacts rather than genuine differences,

as the discrepancies arise right at the point where the yield stress value is reached. This is a robust feature of the model and ought also to be respected in the experiment; the fact that lower values than the expected yield stress values are obtained experimentally should therefore be attributed to the way the stress is actually monitored in the experiment upon cessation of the flow.

Table 4.1. Model parameters obtained from the non-linear parametric fit of the hysteresis curve-rheogram A of sample 8 and sample 9 [Bureau *et al*. (1980)], in Figure 4.3. Each set of parameters is used to predict the response of the respective blood under different conditions (i.e. a triangular step-change of larger magnitude –see Fig. 4.3b and Fig. 4.3d which correspond to rheogram B) or even different type of experiments (i.e. rectangular step-change in shear rate, in Fig. 4.8 –also obtained LAOS predictions with these two sets of parameters, however the LAOS data do not correspond to the same blood sample).

Parameters	Sample 8 (Figure 3a)	Sample 9 (Figure 3c)
c_f (g/dl)	0.125	0.173
γ_0	0.039	0.039
k_λ	1.214	1.207
k_G	0.595	0.216
γ_∞	1	1

4.3.5 LAOS experiments

Finally the developed model was tested by comparing its predictions against very recent experimental results obtained with whole blood under Large Amplitude Oscillatory Shear flow (LAOS) reported by Sousa *et al*. (2013). The experimental conditions of large amplitude oscillatory shear flow consist of a sinusoidal strain as shown in Eq. (4.23). The corresponding shear rate is simply the first derivative of the strain with respect to time as shown in Eq. (4.24). The strain amplitude is given by γ_L while ω is the oscillation frequency.

$$\gamma(t) = \gamma_L \sin(\omega t) \ , \tag{4.23}$$

$$\dot{\gamma}(t) = \gamma_L \omega \cos(\omega t) \ . \tag{4.24}$$

As the provided data involved samples other than the ones for which the model parameters have been developed (samples 8 and 9 of Bureau *et al*. (1980)) and as, again, no values for the samples fibrinogen concentration have been reported, we first used available steady state data in order to obtain the steady state Casson model parameters. Those data (from Sousa *et al.* (2013)) are plotted in Fig. 4.9 in Casson-appropriate coordinates (i.e. as the square root of the shear stress with respect to the square root of the shear rate).

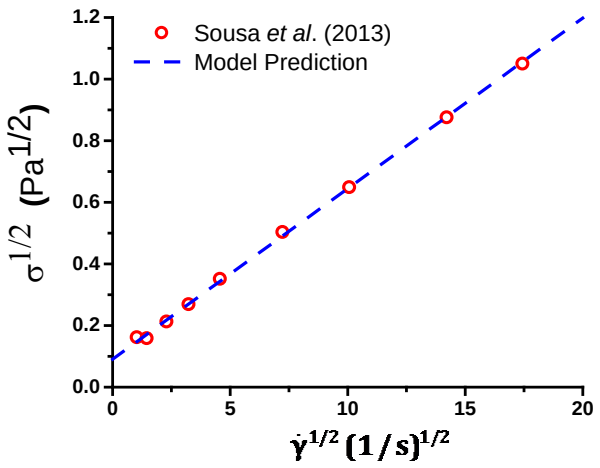

Figure 4.9. Fitting of blood steady shear data to obtain the steady state model parameters. The data correspond to Donor A from the work of Sousa *et al*. (2013), with Hct=41.6% and T=37 ^{o}C.

First, as Fig. 4.9 shows, the data fall almost perfectly on a straight line. Thus, one sees again evidence for the appropriateness of the Casson model to represent the steady state shear blood flow behavior, consistent to the findings of our previous work [Apostolidis and Beris (2014)]. Based on a least squares fit of the data, the model viscosity, μ, is found to be 0.0030 Pa·s, while the yield stress is 0.00823 Pa. Note that almost the same viscosity value (0.00302 Pa s) is predicted from our previously developed parametric relationship, Eq.(4.4), for the reported hematocrit and temperature values, providing, again, independent evidence for the validity of that expression. Using Eqs. (4.2) and (4.3), and the yield stress value obtained from the Fig. 4.9 fit through extrapolation, we back-calculated the fibrinogen concentration, c_f as $c_f = 0.512\, g/dl$. Although this value came out to be a little high it is still close enough to the

physiological range (between 0.1 and 0.4) to be acceptable. Also, note that as the provided steady state shear data, as shown in Fig. 4.9, do not show within the experimental range of shear rates covered a transition to a Newtonian behavior similar to the one corresponding to the data of Merrill and Pelletier (1969) shown in Fig. 4.1, we used a very high value for γ_∞ that does not come to affect the predictions of the model.

As we do not have an independent transient experiment for low shear rates to fit the remaining three of the transient model parameters, $\gamma_0, k_{L,}$ and k_G, we used the values corresponding to either one of the Bureau *et al.* (1980) samples, 8 and 9, as obtained from the rheograms shown in Fig. 4.3a and 4.3c, respectively. We then compared the model predictions obtained with these two sets of parameters (on top of the same steady state parameters evaluated as discussed above) against the LAOS data reported by Sousa et al. (2013). For that comparison, we used the Lissajous-Bowditch representations, both with respect to the shear as well as shear rate, two different frequencies, $\omega = 0.251\,\text{rad/s}$ and $\omega = 0.631\,\text{rad/s}$, as well as two different strain amplitudes, $\gamma_L = 1.0$ and $\gamma_L = 0.1$. The comparisons are shown for the two different values of the frequency in Figs. 4.10 and 4.11, respectively, with the continuous and the dashed lines denoting the predictions obtained with the transient parameters developed from samples 8A and 9A, respectively.

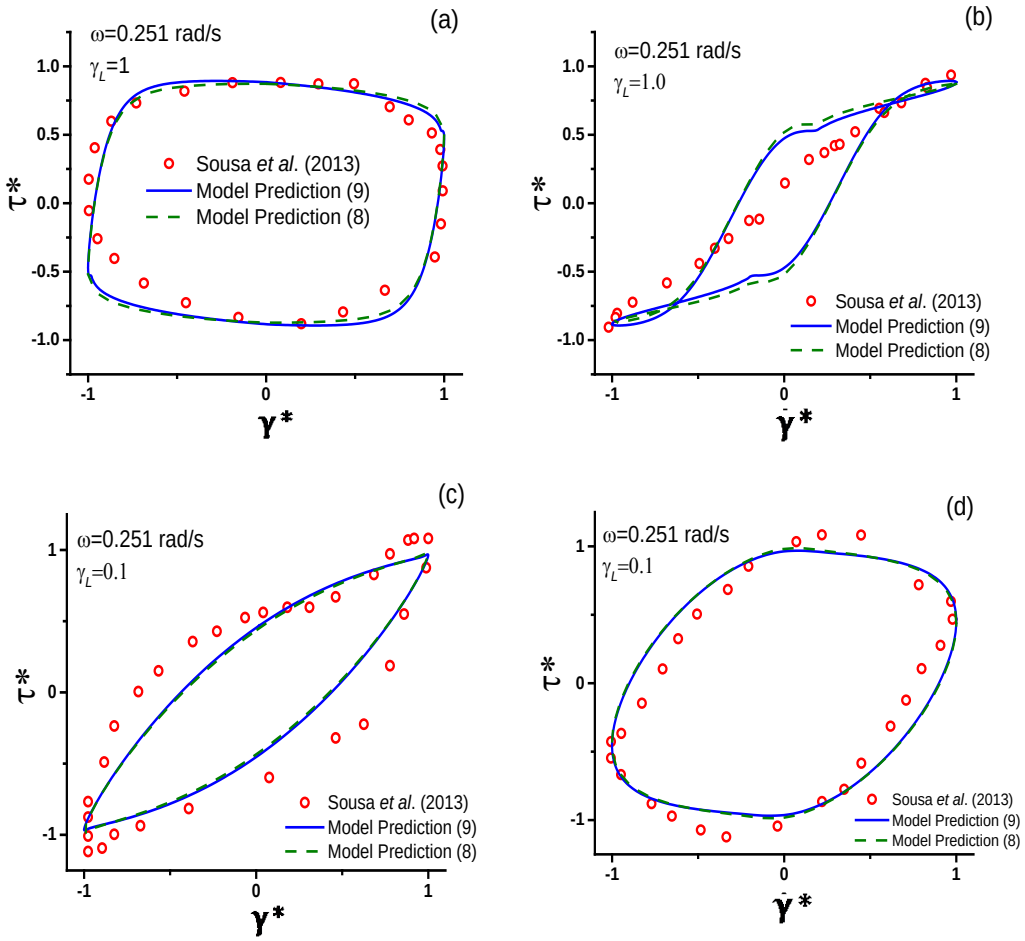

Figure 4.10. Non-dimensionalized elastic (a, c) and viscous (b, d) projections of the Lissajous-Bowditch diagrams for ω =0.251 rad/s and (a, b) γ_L =1 or (c, d) γ_L =0.1. With the continuous and the dashed lines we denote the model predictions obtained both with the same steady state parameters μ = 0.0030 Pa·s and τ_0 = 0.00823 Pa and with the transient parameters developed from samples 8 and 9 of Bureau *et al.* (1980), as obtained from the rheograms A shown in Fig. 3a and 3c, respectively, whereas with the symbols we denote the experimental data of Sousa *et al.* (2013).

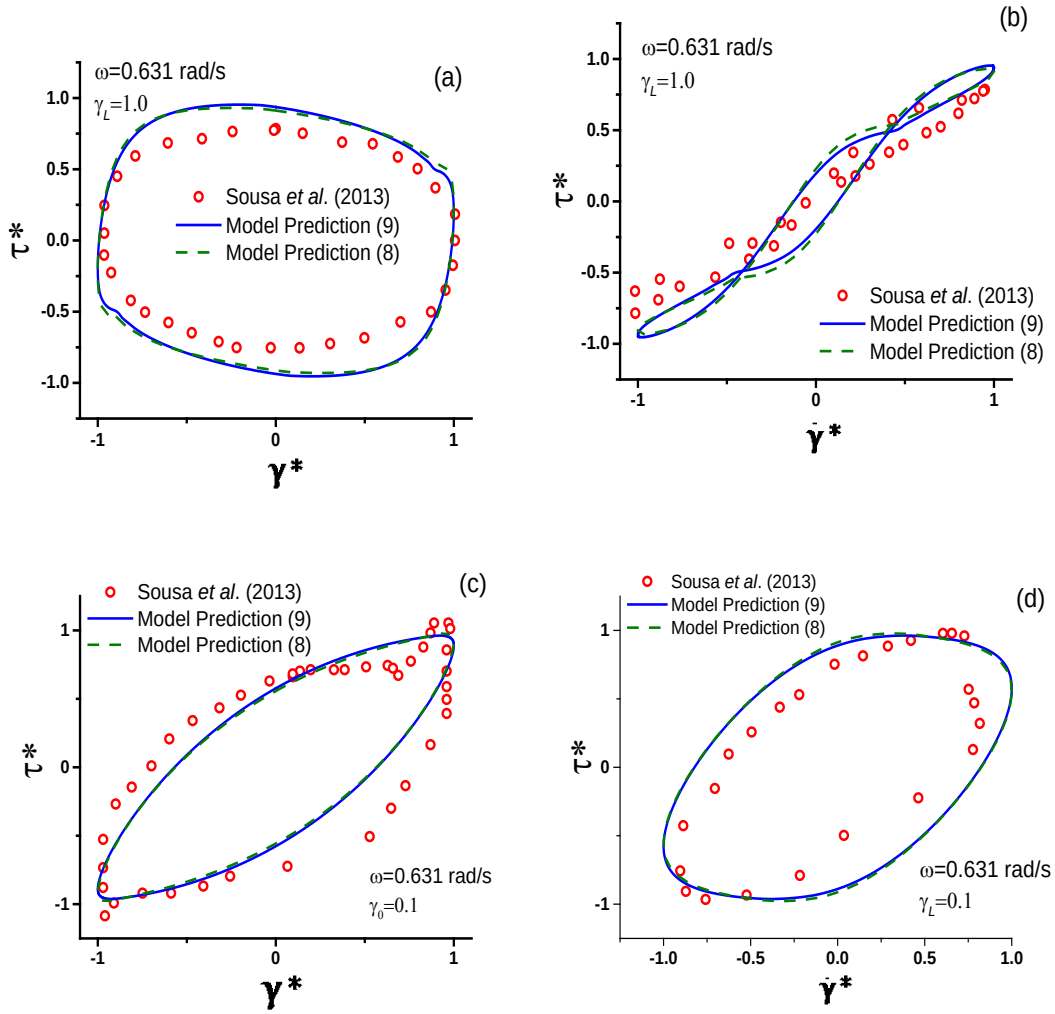

Figure 4.11. Non-dimensionalized elastic (a, c) and viscous (b, d) projections of the Lissajous-Bowditch diagrams for ω =0.631 rad/s and (a, b) γ_L =1 or (c, d) γ_L =0.1. With the continuous and the dashed lines we denote the model predictions obtained both with the same steady state parameters μ = 0.0030 Pa·s and τ_0 = 0.00823 Pa and with the transient parameters developed from samples 8 and 9 of Bureau *et al.* (1980), as obtained from the rheograms A shown in Fig. 3a and 3c, respectively, whereas with the symbols we denote the experimental data of Sousa *et al.* (2013).

The LAOS data and model predictions are shown in Figs. 4.10 and 4.11 via a series of two dimensional Lissajous-Bowditch diagrams whereby the non-dimensional stress vs. non-dimensional strain is the elastic projection and the non-dimensional stress vs. non-dimensional shear rate is the viscous projection. The strain and shear rate are scaled by maximum values, while the stress is non-dimensionalized by the first harmonic of the stress decomposition given by

$$\sigma(t) = \gamma_L \sum_{n=1(odd)} \left[G_n^{'} \sin(n\omega t) + G_n^{''} \cos(n\omega t) \right] . \tag{4.25}$$

As we can see in Figs. 4.10 and 4.11, most of the LAOS features are adequately captured by the model. Of course, once more we cannot expect to see quantitative agreement, not only for the reasons stated before (simplicity of the model, involving few parameters, as well as an anticipated limited region of applicability due to the isotropicity assumed for the structure) but also because the transient model parameters are not obtained through a fit to pertinent to the LAOS experimental data. Nevertheless, it is instructive to see that all the major trends seen in the LAOS experimental data as different parameters are modified are also seen in the model predictions: Namely, as the amplitude of the imposed oscillation decreases from 1 to 0.1 we see very similar changes taking place in both the model predictions and the experimental data for either the elastic or viscous projection; similarly the changes affected by changes in the frequency are also well captured. The only major discrepancy is observed with the viscous projection associated with $\omega = 0.251$ rad/s and $\gamma_L = 1$ (see Fig. 4.10b) where the data seem to fall on a line whereas the model predictions show a rather large loop in the center. To see whether this is a fundamental flaw of the model or rather a mismatch

of parameter values, we undertook an additional sensitivity study of the model predictions to the imposed strain amplitude with the results shown in Fig. 4.12.

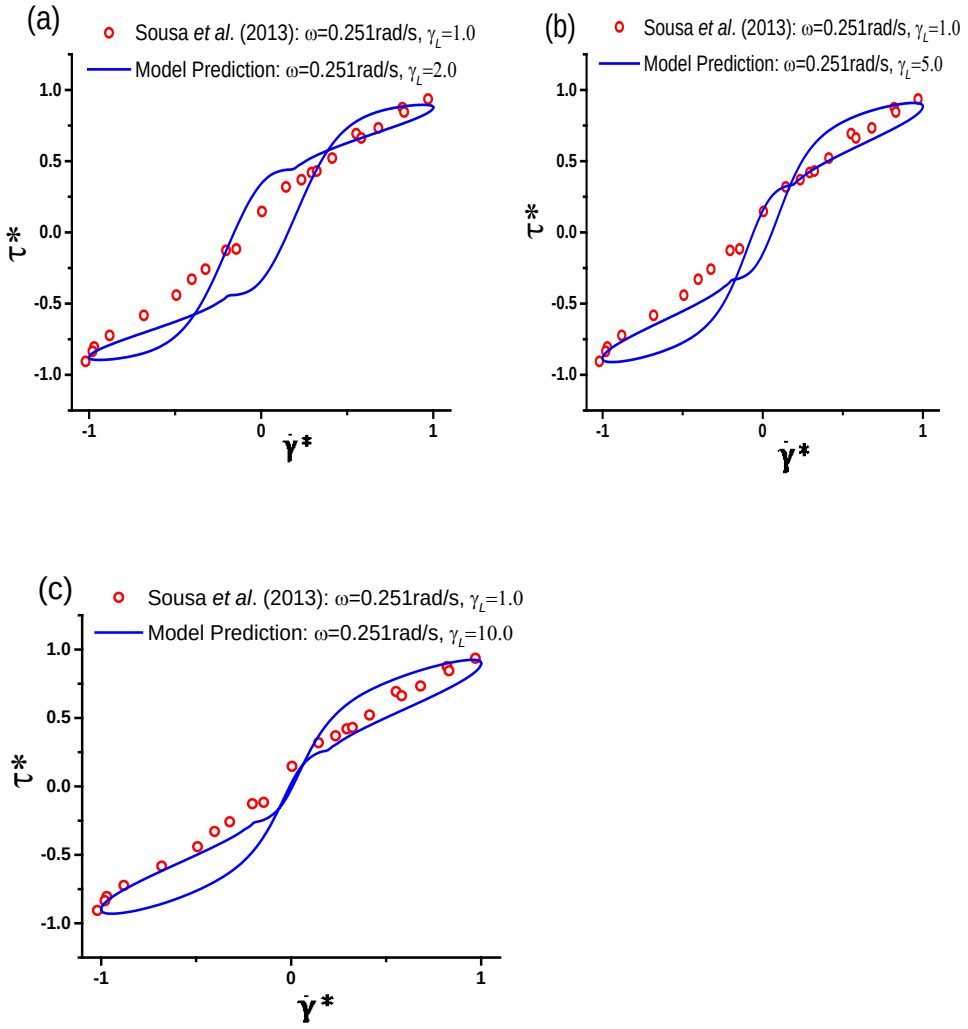

Figure 4.12. Non-dimensionalized viscous projections of the Lissajous-Bowditch diagrams for ω =0.251 rad/s and γ_L =0.1 of the experimental data of Sousa *et al.* (2013), denoted by the symbols, compared against model predictions, denoted by the continuous lines, obtained with the steady state parameters μ = 0.0030 Pa·s and τ_0 = 0.00823 Pa and with the transient parameters developed from sample 8 of

Bureau *et al.* (1980), as obtained from the rheogram A shown in Fig. 3a, evaluated at different strain amplitudes: (a) $\gamma_L = 2$; (b) $\gamma_L = 5$ and (c) $\gamma_L = 10$.

What Fig. 4.12 shows is that the model predictions depend sensitively to the imposed amplitude of the oscillations. As this amplitude increases there is a clear tendency for the loop in the viscous Lissajous-Bowditch projection to shrink considerably (see, for example, Fig. 4.12b) thereby the model predictions approaching considerably closer to the data. It is therefore still considered a reasonable prediction of the observed trends, despite the above-mentioned model limitations.

4.4 Conclusions

In this work we showed how a structurally-based, albeit phenomenological, thixotropic viscoplastic model can be developed and used to explain the main thixotropic characteristics associated with blood flow rheology in transient shear flows involving low and moderate shear rates. The model not only duly reduces to the Casson model under steady-state, simple shear, flow conditions (at least for low to moderate shear rate values) but also allows for the previously observed, but so far unexplained, transition to a Newtonian behavior exhibited at high shear rates to take place [Merrill and Pelletier (1967)]. Furthermore, we have shown that this transition happens naturally as a consequence of the finiteness of the elastic strain assumed within the material. This is one of the most important contributions of the model, which therefore also gives credence to its main assumptions, i.e. that the shear stress can be analyzed into an elastic and a viscous contribution with the elastic one been further described in terms of the product of an elastic modulus and an elastic strain. The kinematic theory of plasticity

of Dimitriou *et al*. (2013) has been used for the description of the elastic strain evolution suitably modified to allow for a variable maximum elastic strain value. Then, both that maximum elastic strain as well as the equilibrium value of the elastic modulus are assumed to be functions of the scalar structural parameter λ . Finally, both the structural parameter and the modulus of elasticity are assumed to obey suitably defined relaxation equations.

The structure of the model is such to allow full use of previously established parametric relations for the Casson model based on steady state shear data. Furthermore, the deviations from the Casson behavior allow to fix one more parameter. Thus, only three parameters remain to be fit and all of those have physical meaning with well-established limited range of values. That makes the model simple and efficient to use. We demonstrated that by successfully fitting available data for a triangular shear rate transient experiment of [Boureau *et al*. (1980)]. The data at low shear rate that we used to fit our additional model parameters were almost perfectly reproduced by the model. In addition, the model parameter values were all within the expected range. Furthermore, we validated the model, by comparing it against either additional triangular data obtained at higher shear rates, or data obtained in step change of shear rate, all of them using the same blood samples. In all cases the agreement was good, semi-quantitative, capturing all the experimentally observed trends. In addition, we were able to show all the experimentally observed trends observed in very recent LAOS whole blood experiments by Sousa *et al.* (2013). It was the first time that LAOS data were reported and in the present work it is the first time that those data have been compared rather successfully against the predictions of an independently developed model.

Still, due to the model simplicity and phenomenology, its predictions were found to deteriorate at higher shear rates. It is therefore best considered as an intermediate model, applicable primarily at low and perhaps up to moderate shear rates (order 1 s^{-1}) only. Nevertheless, it has helped to interpret physically many complex transient flow results and it provides a significant improvement over previous models with a significantly wider capability of fitting transient data and thixotropy with the use of a very modest number of adjustable parameters.

Chapter 5

A CONVERGENCE STUDY FOR THE PROPER IMPLEMENTATION OF BOUNDARY CONDITIONS IN SIMULATIONS OF ARTERIAL FLOW: GEOMETRIC AND NON-NEWTONIAN EFFECTS

5.1 Introduction

The decreasing ratio of hardware costs to computational power has seen Computational Fluid Dynamics (CFD) bloom in the past decades. While at the early stages the applications of CFD pertained primarily to high-tech engineering problems, the past two decades CFD has given rise to a large number of medical related studies, such as the analysis of the flow in specific arteries. Cardiovascular diseases are affected by the hemodynamics within the arteries, while low wall shear stress values (WSS) have been correlated with atherogenesis, the initial stages of atherosclerosis [Cecchi *et al*. (2011)]. Therefore, CFD can be used to obtain detailed flow information, such as the WSS distribution, in the vessels of investigation.

Despite the rapidly increasing number of such investigations, it can be argued that CFD is still emerging in the biomedical field [Byoung-Kwon (2011)]. The physiological relevance of hematological data acquired from simulations can be questionable. The commonly accepted limiting factors that decide the accuracy of the results of CFD simulations in the biomedical field are the accuracy of the geometric model, the complexity of fluids in the human body, and the imposed boundary conditions (BCs) [Byoung-Kwon (2011)].

State of art technologies have offered significant improvements in overcoming some of these limitations. Medical imaging techniques, such as computed tomography,

ultrasound imaging, and magnetic resonance imaging offer very detailed, personalized geometrical models that are used for CFD simulations. Therefore, the geometric representation no longer constitutes a significant limitation. Similarly, existing technologies, such as Doppler ultrasound, pressure wire, and non-invasive techniques, provide pressure and flow information at specific locations of the arterial network, which then can be used as BCs in CFD simulations. However, even though these techniques provide accurate pressure and flow measurements, the information obtained in each case reflects the data of a specific case, at a specific time. These technologies cannot be used to examine what-if scenarios or else, for modeling practices [Johnson *et al*. (2011a); Taylor and Draney (2004)]. Thus, imposing the appropriate BCs in simulations of arterial flow still constitutes a limitation in the field.

The proper implementation of BCs in simulations of flow in a specific artery requires that the impact of the rest of the arterial network be taken into consideration [Formaggia *et al*. (2009)]. This can be achieved by using boundary conditions that, instead of absolute values, describe a correlation between outlet flow and pressure [Johnson *et al*. (2011a); Formaggia *et al*. (2009)]. Such correlations represent flow information for the arterial network that extends beyond the boundary points of the simulation, and they are typically the product of a 1D-network model that is used to represent the flow in an extended part of, or even the entire, arterial system. The two main approaches that have been used for the implementation of more sophisticated boundary conditions are only distinguishable based on the complexity of the network model involved and they range from a linear resistance or lumped parameter/Windkessel (0D) model to a 1D full arterial network [Johnson *et al*. (2011a)].

In the first of these cases, the lumped parameter models represent a truncation of the subnetwork resistance by making use of a lumped and regressed parameter set. As a consequence, such models may be limited in their predictive capability, especially in time-dependent simulations, and by necessity involve parameters lacking a physiological meaning. The second approach, which bases the outlet BCs on the predictions of an approximate flow model for the entire arterial network, is more rigorous and became more popular in the past decade. However, the use of a complete set of BCs as predicted from 1D network model requires a sophisticated coupling of the 1D model predictions to the 3D simulations, which can only be made possible through the use of proprietary, in-house developed codes. Detailed discussions on the coupling between the 3D domain and the lower order models can be found in literature [Johnson *et al*. (2011a); Formaggia *et al*. (2009); Esmaily-Moghadam *et al*. (2013); Formaggia *et al*. (2001)].

Johnson et al. [Johnson *et al*. (2011a)] proposed a more versatile approach which decouples the detailed 3D simulation upstream from the more approximate 1D network downstream. The 1D model used is an impedance model, the output of which is a prediction of the pressure/flow relationships for the entire arterial network, yielded in the form of complex impedance coefficients in the Fourier domain [Johnson *et al*. (2011b)]. Then, the decoupling is achieved through the intermediate use of an approximate "simulant" model (run in Matlab environment), based on the lubrication approximation, which corresponds to the full 3D and time-dependent numerical simulation. The simulant model makes use of a correction term which accounts for the observed differences between the simulant predictions (based on the lubrication approximation) and the 3D simulations results. This scheme, which is applied

iteratively until convergence is reached, was demonstrated with simulations of the flow in the left coronary artery [Johnson *et al*. (2011a)]. However, the geometric models used in that study were simplistic and not capturing important effects that can impact the dynamics of the flow, such as the curvature of the vessels. Moreover, the simulations were based solely on the Newtonian assumption of the fluid, therefore neglecting the complex rheology of blood [Apostolidis and Beris (2014); Apostolidis *et al*. (2015)].

The complex nature of the fluids in the human body is a main reason of concern for the reliability of the results of blood flow simulations. For the simulations of the human right coronary arteries, Johnston *et al*. (2006) showed that, "when studying the wall shear stress distribution for transient blood flow in arteries, the use of a Newtonian blood flow model is a reasonably good approximation. However, to study the flow within the artery in greater detail, a non-Newtonian model is more appropriate". The non-Newtonian characteristics are prevalently demonstrated at low shear rates which can exist near bifurcation sites and at recirculation zones developing in the arteries. Since the generation of atherosclerosis, i.e. atherogenesis, has been correlated with low (<0.5 Pa) WSS values [Cecchi *et al*. (2011); Chaichana *et al*. (2012); Soulis *et al*. (2008); Wentzel *et al*. (2012)], it becomes clear that non-Newtonian models need to be employed. This has been done with increasing frequency for flow simulations of various vascular components, such as the aorta [Karimi *et al*. (2014); Morbiducci *et al*. (2013); Liu *et al*. (2011)], the cerebral [Bernabeu et al. (); Campo-Deaño *et al*. (2015)], and the coronary arteries [Johnston *et al*. (2006); Lassaline *et al*. (2014); Chaichana *et al*. (2012); Soulis *et al*. (2008)]. In all of these cases, generalized Newtonian expressions are adopted which can better capture the complex behavior of the fluid

under steady state conditions. However, while a variety of constitutive models is examined in literature, there is strong evidence that the steady state rheology of blood is best described by the Casson model [Apostolidis *et al*. (2015)].

The goal of this investigation is to further develop and validate an efficient implementation of proper outflow boundary conditions (OBCs) for CFD simulations of arterial flow. The OBCs are obtained from a 1D-network model of the arterial system [Johnson *et al*. (2011)], while the system of investigation is the left coronary artery (LCA). The geometric model includes significant improvements to previously developed geometries that were used to test the simulant-based approach for the efficient implementation of OBCs, which was first introduced by Johnson *et al*. (2011a). The proposed scheme guarantees that the outward flow rate is related to the outlet pressures in a way consistent with rest of the network, and independent to the flow geometry and the fluid rheology model employed. The functionality of the scheme is validated through three examples: a Newtonian simulation of a healthy system patterned after the LCA, a Newtonian simulation of a diseased case where an occlusion is developed in the LCA, and a Casson simulation of the healthy LCA.

The rest of the chapter is organized as follows: in Section 5.2 we discuss the materials and methods used; this entails the construction of geometrical models, an overview of the Casson parametric model for blood flow, a briefing of the simulant model, the numerical stability analysis and the acceleration of the scheme convergence via numerical analysis. The results of the simulations are presented in Section 5.3, and the discussion on the impact of this work is included in Section 5.4.

5.2 Material and Methods

5.2.1 Geometrical models

The present investigation regards the examination of 3D arterial flow problems. The particular simulated vascular geometry in this study is the left coronary artery (LCA), which consists of the left main artery (LM) that bifurcates into the left anterior descending (LAD) and the left circumflex (LCX). In this work, we consider two geometrical models: a healthy or physiological LCA geometry, which is a prototype asymmetric arterial bifurcation, and a modified or pathological geometry, so as to model the effects of a hypothetical stenosis in the LAD resulting to a lumen narrowing of approximately 82%. The two geometries are presented in Fig. 5.1.

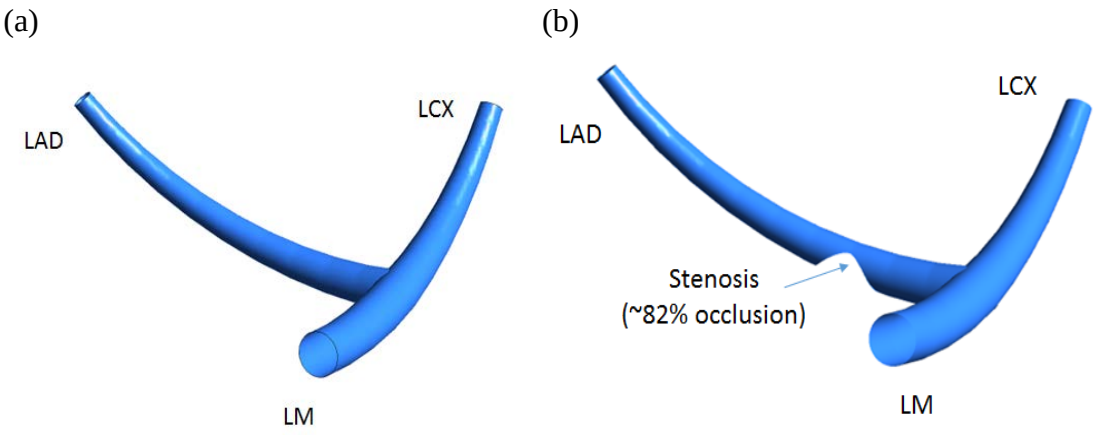

Figure 5.1. Geometries of left coronary artery used for the simulations: (a) Physiological case, and (b) Pathological case with a stenosis causing ~ 82% occlusion of the LAD artery.

The simplified vascular geometries have been developed based on anatomically accurate dimensions of the LCA, as reported in literature [Dodge *et al*. (1992)]. The dimensions of the constructed vessel geometries are presented in Table 5.1. Tapering effects were included in the construction of the LAD and LCX arteries, while a branching angle of 90^{o} was used between the LCX and the LAD [Dong *et al*. (2015)]. Finally, an important feature, and an improvement to the previously used geometries of our LCA investigations [Johnson *et al*. (2011a)], is the inclusion of curvature in the geometry vessels. The curvature originates from the modeling of the heart as a sphere, therefore requiring that the arteries existing on the surface of the heart be curved as well.

The geometries as well as the meshes were developed with the use of the commercial software ANSYS ICEM CFD version 12 (ANSYS, Inc., Canonsburg, PA, USA).

Table 5.1. Characteristic lengths of geometrical model

Vessel	Diameter (mm)		Length	Curvature
	In	Out		
LM	4	4	10	34.92
LCX	3.4	1.6	17	34.92
LAD	3.8	2	30	34.92

5.2.2 Application of physiological parameters

The physiological parameters of importance in simulations of blood flow are the temperature, T, the hematocrit, Hct, and the fibrinogen concentration, c_f. Fibrinogen is known to play a key role in bridging the adjacent red blood cells (RBCs) and therefore giving rise to RBC aggregates. The presence of RBC networks explains the complex rheology of blood, manifested by the exhibition of yield stress, a property that is strongly dependent on c_f. The results obtained in the current investigation correspond to average, normal values of physiological parameters (Hct =40%, T = 37C, c_f = 0.3 g/dl).

We have carried out simulations for blood density of 1060 kg/m3 both under the Newtonian assumption, and by taking into consideration the non-Newtonian rheology of blood, in the form of a Generalized Newtonian model. In the first case, a constant viscosity, μ, of 0.003 was used. In the second, we employed a parametric form of the Casson constitutive equation that we recently developed [Apostolidis and Beris (2014)]. This model has been extensively validated against experimental data, while comparisons with other models frequently used in blood flow simulations, such as the Herschel Bulkley and the Bingham model, show that the Casson describes best the rheology of blood [Apostolidis and Beris (2014)]. The Casson parametric model is defined as:

$$\sqrt{\tau} = \sqrt{\tau_y} + \sqrt{\mu\,\dot{\gamma}}\ ,\ \tau \geq \tau_y\ , \tag{5.1}$$

$$\tau_y = \begin{cases} [(Hct - Hct_c)^2 \times (0.5084 c_f + 0.4517)^2 & Hct > Hct_c \\ 0 & Hct \leq Hct_c \end{cases}\ , \tag{5.2}$$

$$Hct_c = \begin{cases} 0.3126{c_f}^2 - 0.468c_f + 0.1764 & c_f < 0.75 \\ 0.0012 & c_f \geq 0.75 \end{cases}, \tag{5.3}$$

$$\mu = \eta_p \left(1 + 2.0703 \times Hct + 3.7222 \times Hct^2\right) \times \exp\left(-7.0276\left(1 - \frac{T_0}{T}\right)\right), \tag{5.4}$$

where τ_y, $\dot{\gamma}$, and Hct_c denote the yield stress, shear rate, and critical hematocrit, respectively. The critical hematocrit is the minimum hematocrit below which blood does not exhibit a yield stress. In this model, η_P represents the plasma viscosity and has a value of $1.67 \times 10^{-2}\ dyne{\times}s/cm^2$, while T_0 is the reference temperature of 296.16 *K*. For the physiological parameters reported above (Hct =40%, T = 37C, c_f = 0.3 g/dl), the model predicts a yield stress 0f 0.00412 Pa and a viscosity of 0.00295 $Pa \cdot \sec$.

5.2.3 Efficient implementation of outflow boundary conditions (OBCs)

While the inlet boundary condition is a periodic mass flux (period T=1.25 sec) readily obtained from Johnson *et al*. (2011a), and the typical no slip condition is applied on the vessel wall, the proper implementation of the outlet pressure BCs requires some attention. The complexity rises due to the inclusion of the proper closed network condition for the in vivo model of blood flow through the LM coronary artery system, which requires that the outlet pressure profiles are related to the outward flow rates in a fashion consistent with the rest of the network. The pressure/flow information for the vasculature that extends beyond the limits of the 3D simulated geometry are obtained from a 1D-network model [Johnson *et al*. (2011b)], in the form of complex impedances:

$$\hat{P}_{j,k} = \hat{Z}_{j,k}\hat{Q}_{j,k} \ , \tag{5.5}$$

In Eq. (5.5) $\hat{P}_{j,k}$ is the pressure, $\hat{Q}_{j,k}$ the flow rate, and $\hat{Z}_{j,k}$ the complex impedance. The symbol '^' is used to denote the Fourier transform in time, assuming a period of $T = 1.25s$ which corresponds to the period of the input flow profile, while k denotes the corresponding k-th mode in the Fourier space and j is the vessel of reference (LAD or LCX). The impedance model can be used to obtain the complex impedances at any point of the arterial network, thus providing in-vivo boundary conditions for the simulation of flow at the vascular component of interest. However, ensuring consistency between the outlet pressure profiles and the 1D-network derived impedances requires additional effort.

Johnson *et al*. (2011a) have shown how this consistency can be achieved through the intermediate use of an approximate simulant model of the outlet pressure/flow relationship corresponding to the full 3D and time-dependent numerical simulations. The proposed methodology involves an iterative approach, based on the simulant model, which results in the effective implementation of 1D outlet conditions corresponding to the network impedance model into full time-dependent 3D simulations. An elaborate explanation of the proposed scheme can be found in [Johnson *et al*. (2011a)]. A brief explanation of the simulant model and the implementation scheme are discussed in Sections 5.2.3.1-5.2.3.2.

5.2.3.1 The simulant model

The incompressibility condition allows for a reference pressure to be defined arbitrarily in time. Therefore, the outlet BCs can be simplified by using one of the

outlet pressures as a reference and subtracting it from all other pressures. In our simulations the LAD outlet pressure is chosen as a reference ($P_{LAD} = 0$). Then, the outflow conditions are given by:

$$\Delta P = P_{LCX} - P_{LAD} \ . \tag{5.6}$$

It is the proper specification of Eq. (5.6) that requires the development of the simulant model. The simulant model assumes pressure driven flow (Poiseuille) in each of the vessels, with only linear viscous forces to overcome. The mathematical formulation for this problem becomes:

$$u_j(t,z) = u_{M,j}(t,z) \cdot \left(1 - \frac{r}{R_j(z)}\right)^2 \ , \tag{5.7}$$

$$\begin{aligned} &\frac{dP_j}{dz} = \mu\left[\frac{1}{r}\frac{d}{dr}\left(r\frac{du_j}{dr}\right)\right] = -\frac{8\mu Q_j}{\pi (R_j(z))^4} \Rightarrow \\ &P_{j,2} - P_{j,1} = -\frac{8\mu Q_j}{\pi}\int_0^{L_j}\frac{dz}{(R_j(z))^4}, \end{aligned} \ , \tag{5.8}$$

where u is the velocity, P the pressure, μ the viscosity, Q the flowrate, L the length of the vessel, and R its diameter. $P_{j,1}$ and $P_{j,2}$ is the pressure at the beginning (point 1) and the end (point 2) of the j artery, respectively (see Fig. 5.1).

For the physiological geometry, an analytical expression for Eq. (5.8) can be obtained by assuming a linear tapering of the vessels and equal pressures at the branching point of the vessel ($P_{LCX,1} = P_{LAD,1}$). Then, Eq. (5.8) reduces to:

$$2\Delta P(t) = -\alpha \Delta Q(t) + \beta Q_{inl}(t) \ , \tag{5.9}$$

where $Q_{inl} \equiv Q_{LAD} + Q_{LCX}$ is the flow rate at the inlet, and α and β are constants and a function of geometrical parameters and the viscosity, given by:

$$\begin{aligned} \alpha &= \frac{8\mu}{3\pi}\left[L_{LAD}\left(\frac{R_{LAD,1}^2 + R_{LAD,1}R_{LAD,2} + R_{LAD,2}^2}{R_{LAD,1}^3 R_{LAD,2}^3} \right) + L_{LCX}\left(\frac{R_{LCX,1}^2 + R_{LCX,1}R_{LCX,2} + R_{LCX,2}^2}{R_{LCX,1}^3 R_{LCX,2}^3} \right) \right] \\ \beta &= \frac{8\mu}{3\pi}\left[L_{LAD}\left(\frac{R_{LAD,1}^2 + R_{LAD,1}R_{LAD,2} + R_{LAD,2}^2}{R_{LAD,1}^3 R_{LAD,2}^3} \right) - L_{LCX}\left(\frac{R_{LCX,1}^2 + R_{LCX,1}R_{LCX,2} + R_{LCX,2}^2}{R_{LCX,1}^3 R_{LCX,2}^3} \right) \right] \end{aligned} \ , \tag{5.10}$$

The final step in the development of the simulant model is the inclusion of a non-linear corrective term, $\delta(t)$. This term accounts for the observed differences between the lubrication approximation based simulant model and the 3D simulation results. Then, the final form of the simulant model becomes:

$$2\Delta P(t) = -\alpha \Delta Q(t) + \beta Q_{inl}(t) - \alpha \cdot \delta(t) \, , \tag{5.11}$$

In the case of a pathological geometry, the occluded vessel is segmented into three parts: the unobstructed downstream, the occluded region (stenosis), and the unobstructed upstream. At each axial point along the LAD vessel, the hydrodynamic radius is calculated so that the pressure differential along the vessel can be computed from:

$$P_{j,2} - P_{j,1} = -\frac{8\mu Q_j(t)}{\pi}\left[\int_0^{stenosis,downstream} \frac{dz}{\left(R_j(z)\right)^4} + \int_{sten.,downstr}^{sten.,upstr} \frac{dz}{\left(R_{hyd,j}(z)\right)^4} + \int_{sten.,upstr}^{L_j} \frac{dz}{\left(R_j(z)\right)^4}\right] \quad (5.12)$$

As explained in detail in Section 5.2.3.2, the simulant is applied iteratively until convergence is reached. A detailed explanation, followed by a geometrical analysis that is required for the evaluation of the above integral (corresponding to the stenosis region), is presented in Appendix B.

5.2.3.2 Iterative implementation of OBCs using the simulant model

The proper enforcement of Eq. (5.11) as an outlet BC in simulations of arterial flow requires an iterative procedure. For the first iteration, an initial guess for the pressure difference between the two outlets, ΔP, is needed. The initial guess can be a time-dependent profile, e.g. with information obtained from a 1D network model, or even a constant, if such information is not available. Then, from the simulation output we can evaluate the corresponding ΔQ profile. To facilitate the calculations, given the expected pulsatile/periodic form of the vectors, we opt to perform the calculations in the Fourier domain. Thus, after taking the Fourier transform of ΔQ, $\Delta \hat{Q}$, we can subsequently estimate the correction term, $\hat{\delta}_k$. From Eqs. (5.5),(5.6) and (5.11) one can obtain an updated prediction of the flow rate, given by:

$$\Delta \hat{Q}_k = \frac{(\hat{Z}_{LAD,k} - \hat{Z}_{LCX,k} + \beta)\hat{Q}_{inl,k} - \alpha\hat{\delta}_k}{\hat{Z}_{LAD,k} + \hat{Z}_{LCX,k} + \alpha} \quad (5.13)$$

Finally, after applying an inverse Fourier transformation to return to the time domain, Eq. (5.13) yields the new outlet pressure BC, corresponding to the updated ΔQ. The new ΔP is then the updated outlet BC that is used in the second iteration. The flow diagram of the described process is shown in Fig. 5.2.

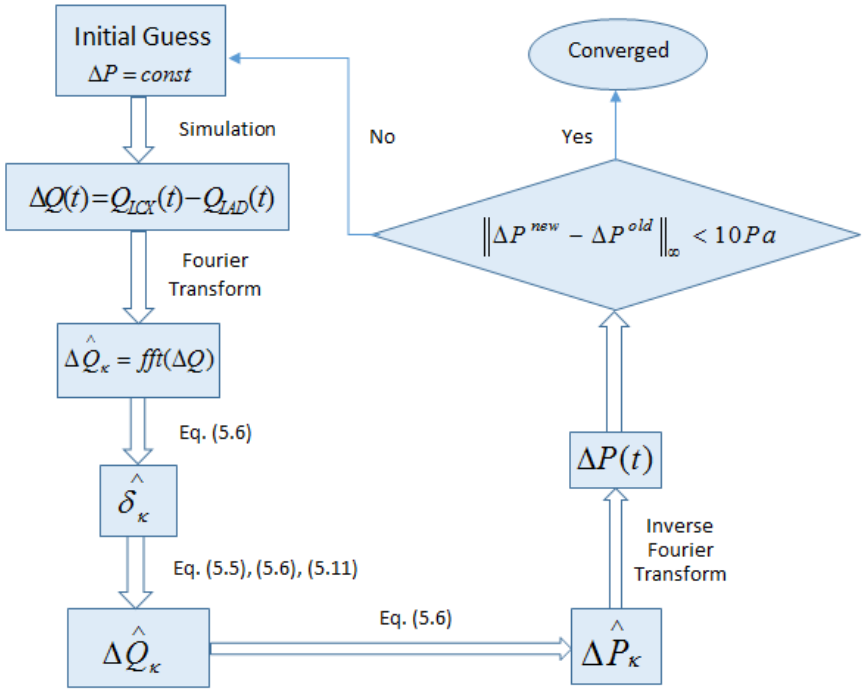

Figure 5.2. Logical diagram for the iterative application of the simulant model.

The proposed scheme converges in ~10 iterations, while the convergence rate is not significantly affected by the initial guess of ΔP (constant vs time dependent from 1D), which shows the robustness of the approach. However, the rather significant

number of iterations required for convergence leads to the examination of numerical techniques that can potentially accelerate the convergence rate.

5.2.3.3 Accelerated convergence of iterative scheme

Numerical analysis was applied in order to accelerate the convergence rate of the proposed iterative scheme. A non-linear series acceleration method, the Shanks transformation, was used to improve the rate of convergence. Based on the Shanks formulation, the transformation of a sequence A_n ($A_n = \sum_{m=0}^{n} a_m$) into another sequence, $S(A_n)$, is defined as:

$$S(A_n) = \frac{A_{n+1}A_{n-1} - A_n^2}{A_{n+1} - 2A_n + A_{n-1}} \ . \tag{5.14}$$

It can be shown that if the error convergence is of a power law form, i.e. $A_n = A_\infty + aq^n$,the transformation of Eq. (5.14) leads to a constant, perfectly converged series. Of course, this rarely happens in practice, but the transformation can lead close enough to perfectly converged series, so that the transformed sequence, $S(A_n)$, often converges faster than the original sequence, A_n. For the application in our system, the sequence A_n is replaced by the nth iteration's pressure profile, $\Delta P_n(t)$. If the initial guess of ΔP is a constant, then the minimum number of iterations required before the Shanks transformation can be applied is four. Then, the Shanks transformation yields:

$$S(\Delta P_3(t)) = \frac{\Delta P_4(t)\Delta P_2(t) - \Delta P_3(t)}{\Delta P_4(t) - 2\Delta P_3(t)\Delta P_2(t)} \tag{5.15}$$

Based on this numerical analysis, the Shanks transformation was applied (usually in the 3rd or the 4th simulation) to get an accelerated convergence of the pressure profile. Fig. 5.3 shows the pressure and flow profiles obtained for Newtonian simulations of the physiological (Fig 5.3a-Fig. 5.3b) and the pathological geometry (Fig.5.3c- Fig. 5.3d).

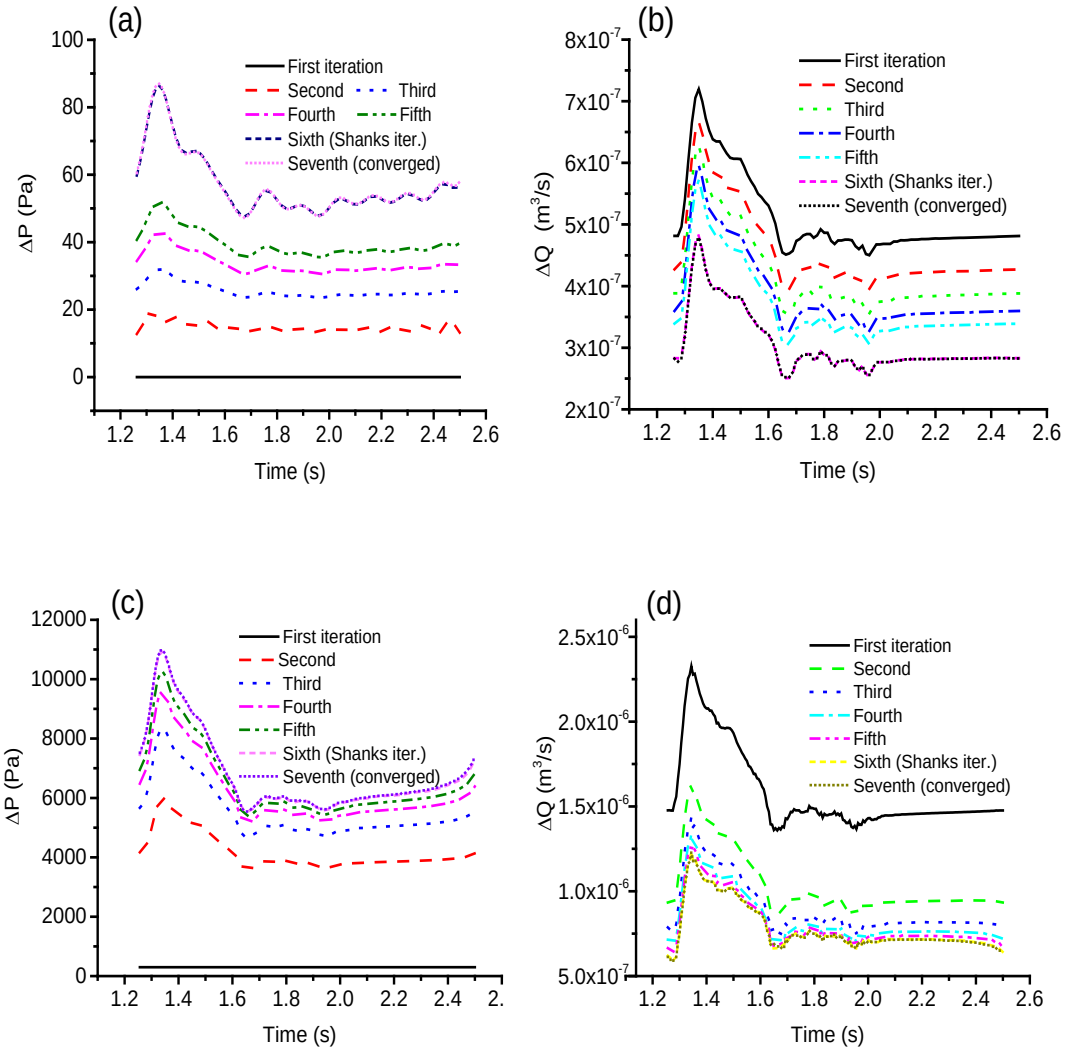

Figure 5.3. Pressure and flow profiles as obtained from the iterative procedure outlined in Section 5.2.3.2. (a), (b): Physiological geometry. (c),(d): Pathological

The Shanks transformation accelerates the convergence of both the pressure and flow profiles. The acceleration is more significant in the case of the physiological geometry where, depending on the simulation specifications (coarse vs base vs dense simulation), the scheme can require up to 16 iterations for convergence (data not shown). In that case, the Shanks transformation reduces the required number of iterations by 50%. The simulations of the stenosis geometry were accelerated by a maximum of ~30%. Based on these results, we conclude that the Shanks transformation can consistently accelerate the convergence rate of the proposed iterative scheme, and therefore reduce the computational demands of the analysis.

5.2.3.4 Numerical stability

It is common practice in CFD investigations to perform a sensitivity analysis in order to show that the obtained results are not significantly affected by numerical error. In the vast majority of the medical related CFD studies in literature, this analysis is restricted to the sensitivity of the simulation outcome to meshes of different densities. Moreover, the sensitivity is often tested only under steady state conditions. Such approaches neglect the impact of the pulsatile nature of blood flow on the numerical stability of the simulations, while the sensitivity to parameters other than the mesh density, such as the integration time step, is rarely examined. Performing a more holistic sensitivity analysis is crucial not only for the obvious reason, that of reliability of the yielded results, but also because, despite the decrease of hardware costs, the simulations of flow in vasculature remain computationally expensive, therefore adopting more

refined parameters than necessary can lead to a tremendous increase in time and/or computational needs.

We have adapted a more general stability analysis by systematically examining the impact of the mesh density, the integration time-step, and the number of iterations performed per time-step. For each of the simulated geometries, the healthy (physiological) and the stenosis (pathological), we are considering three progressively refined parameter cases: a coarse, a base, and a dense one. The analysis is also done for simulations of the physiological geometry with the Generalized Newtonian model, in order to ensure that the additional non-linearity of the Casson model does not influence the numerical stability. The parameters used in each case are presented in Table 5.2.

Table 5.2. Parameters used for the numerical stability analysis.

	Physiological			Pathological		
	Coarse	Base	Dense	Coarse	Base	Dense
Number of cells	4,534	123,12	244,918	128,543	220,138	363,841
Time-step	0.025	0.0125	0.00625	0.025	0.0125	0.00625
Number of steps	100	200	400	100	200	400
Iterations per time-step	40	80	160	40	80	160
Period	2	2	2	2	2	2

It is of importance to note that in order to compare results between two different density cases, for instance Newtonian-coarse versus Newtonian-base simulation results for the physiological geometry, the converged results need to be obtained in each case. This is done in an iterative fashion, as shown in Section 5.2.3.2 and presented in Fig. 3. The converged pressure and flux profiles for all nine cases (three physiological-Newtonian, three physiological-Casson, and three pathological-Newtonian) are shown in Fig. 4.

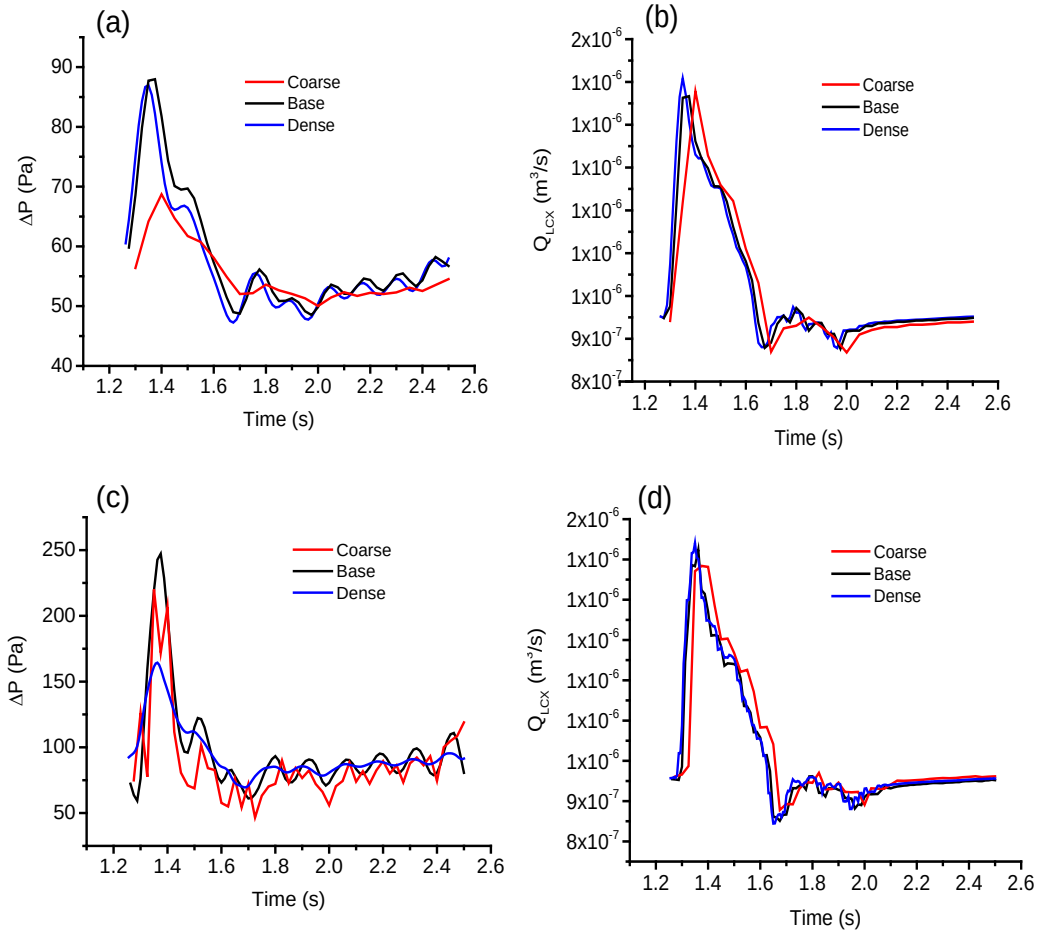

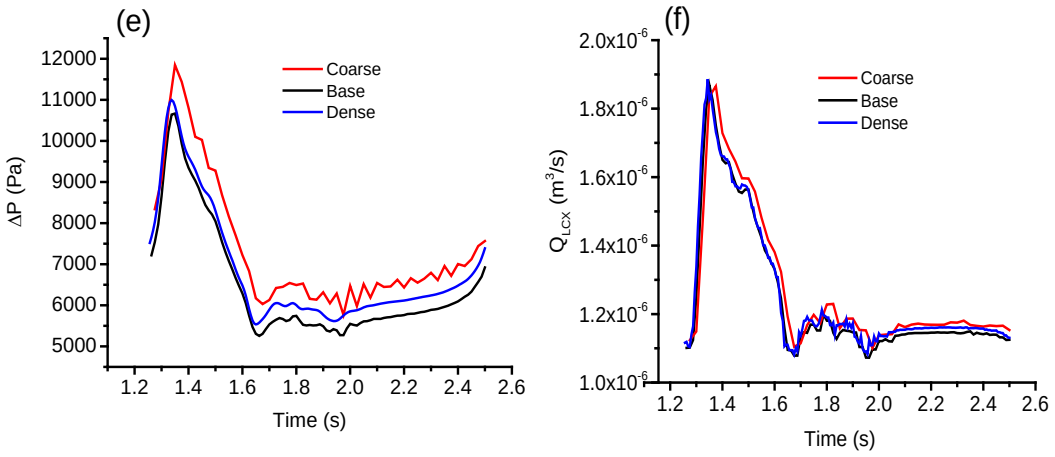

Figure 5.4. Comparison of the converged pressure profiles (a,c,e) and LCX flow rates (b,d,f) for all examined cases: i. Physiological geometry and Newtonian fluid assumption (a,b), ii. Physiological geometry and Casson fluid assumption (c,d), iii. Pathological geometry and Newtonian fluid assumption.

5.3 Results

The results of the flow simulations presented correspond to either the peak systole, reached at time (t_1) of 0.0625 sec, or to the late diastole instant, corresponding to a time (t_2) of 0.6875 sec (see Fig. 5.5a). Moreover, for the post-processing of the physiological model results we have created cross-sections A_1 and A_2, located along the LAD and the LCX artery, respectively (Fig. 5.5b). Finally, all of the presented results correspond to the converged solutions obtained after the iterative application of the simulant model.

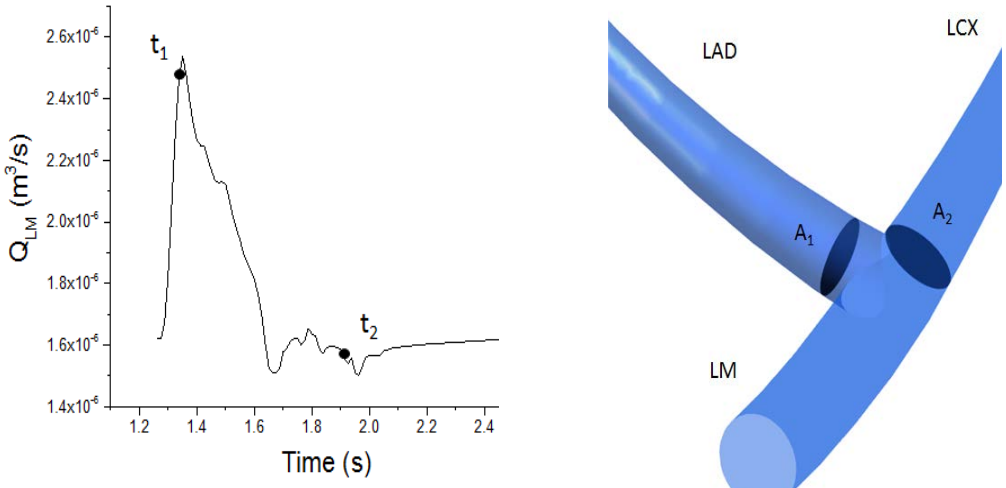

(a) (b)

Figure 5.5. (a): The periodic, transient volumetric flow rate at the left main artery that is used as the inlet boundary condition [Johnson *et al*. (2011a)]. The peak systole and late diastole times, t_1 and t_2, respectively, are marked, (b): cross-sections A_1 and A_2, near the bifurcation site, that are used for the post-processing of the simulation results.

The peak systole results are obtained for comparison purposes, as we are mostly interested in the late diastole findings. The non-Newtonian rheology is expected to be more prominent at low shear rates, which is when the stress and velocity profiles are at a minimum. The same reasoning holds for the selection of the particular locations of the cross-sections A_1 and A_2. Near the bifurcation site we expect the formation of recirculation zones (due to flow separation), and therefore the appearance of zones of low shear rates.

5.3.1 Physiological geometry: Newtonian vs Casson

For the physiological geometry, the comparison between Newtonian and Casson simulations shows important differences between the two cases. To compare the two models we have plotted in Fig. 5 the WSS distribution along the circumference of the cross-sections A_1 and A_2, as predicted in each case (Newtonian vs parametric Casson).

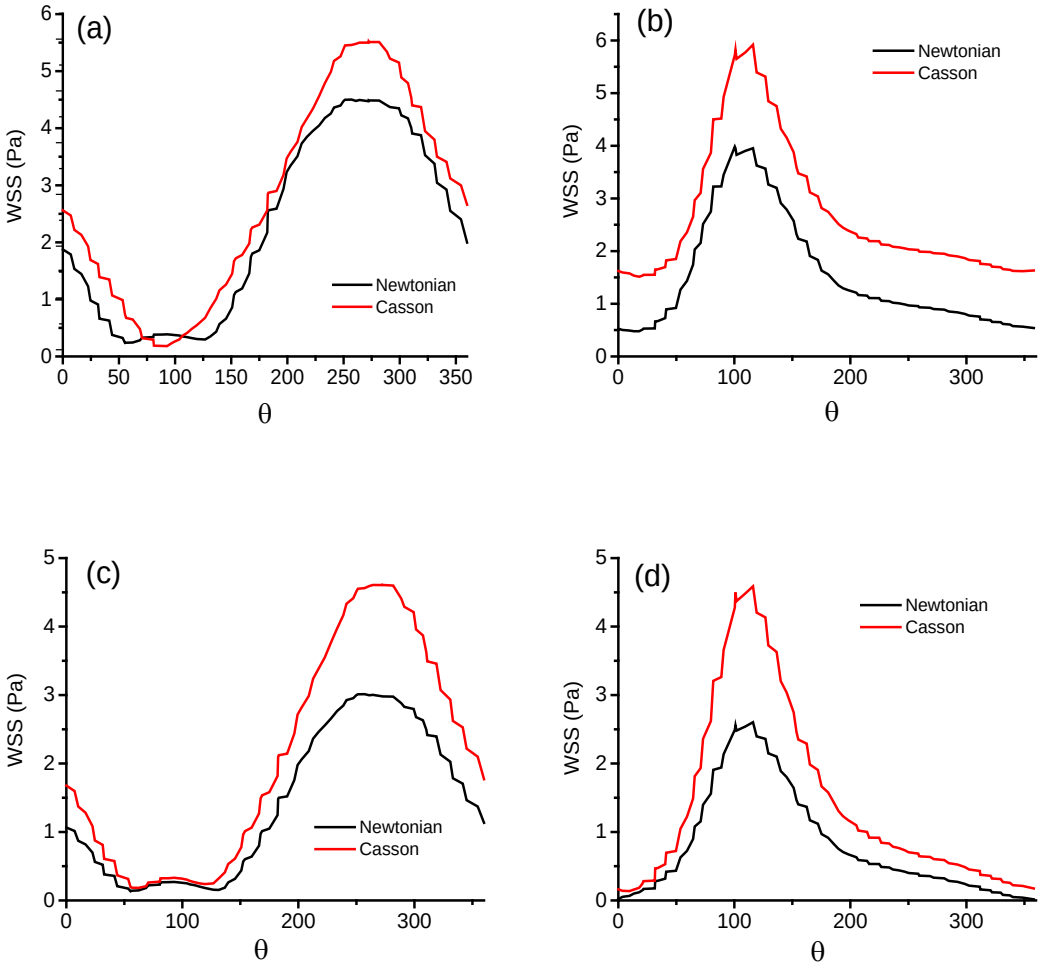

Figure 5.6. WSS distribution along the circumference of the cross-sections A_1 (a,c) and A_2 (b,d), evaluated at t_1 (a,b) and t_2 (c,d).

Fig. 5.6 clearly demonstrates that the Newtonian predictions of WSS are consistently lower to those of the Casson model. This conclusion is in agreement with the predictions of Karimi *et al*. (2014) for the WSS distribution in the human aorta. In addition, we notice that for the circumference of both cross-sections the maximum deviation between the WSS predictions of the two models occurs, in both cases, at the late-diastole time, t_2 (Fig. 5.6 (c-d)). This result is attributed to the fact that the non-Newtonian rheology is primarily manifested at lower shear rates.

Significantly deviations between the Newtonian and the Casson model predictions were also apparent when comparing the predicted shear rate along the two cross-sections. The contours of shear rate for the two planes are shown in Fig. 5.7.

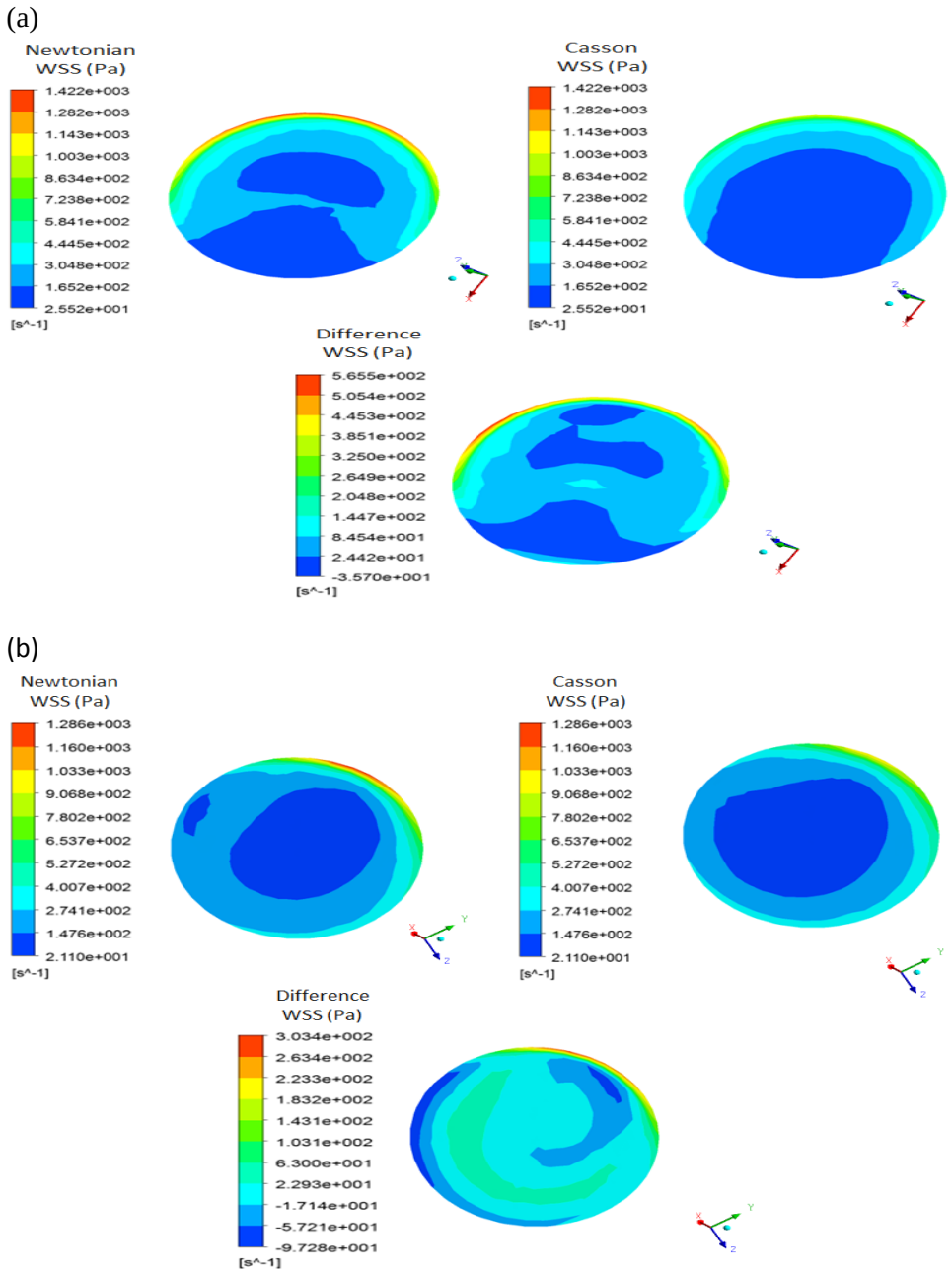

Figure 5.7. Shear rate contours of planes A_1 (a) and A_2 (b), evaluated with the Newtonian and the parametric Casson model, and their difference.

The maximum difference in shear rate estimations of the two models at cross-sections A_1 and A_2 is 40% and 24%, respectively. Thus, from the illustrations of Figures 5.6-5.7 it can be concluded that the rheology of blood impacts significantly the simulation outcome.

5.3.2 Pathological geometry

The proposed methodology for the appropriate implementation of BCs was also applied in the second geometrical model, the pathological coronary artery with a stenosis in the LAD branch (Fig. 5.1b). In Fig. 5.8 we present contours of WSS of the simulated geometry, with a comparison made between the contour of the converged iteration and that of the first iteration. This was done both for the peak systole (Fig. 5a) and the late diastole (Fig. 5b).

(a)

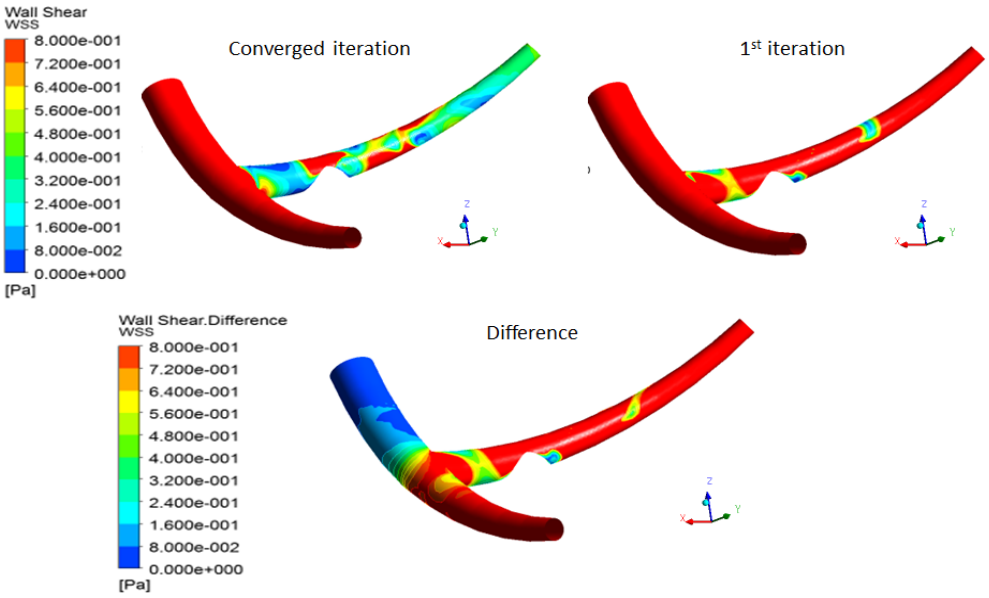

(b)

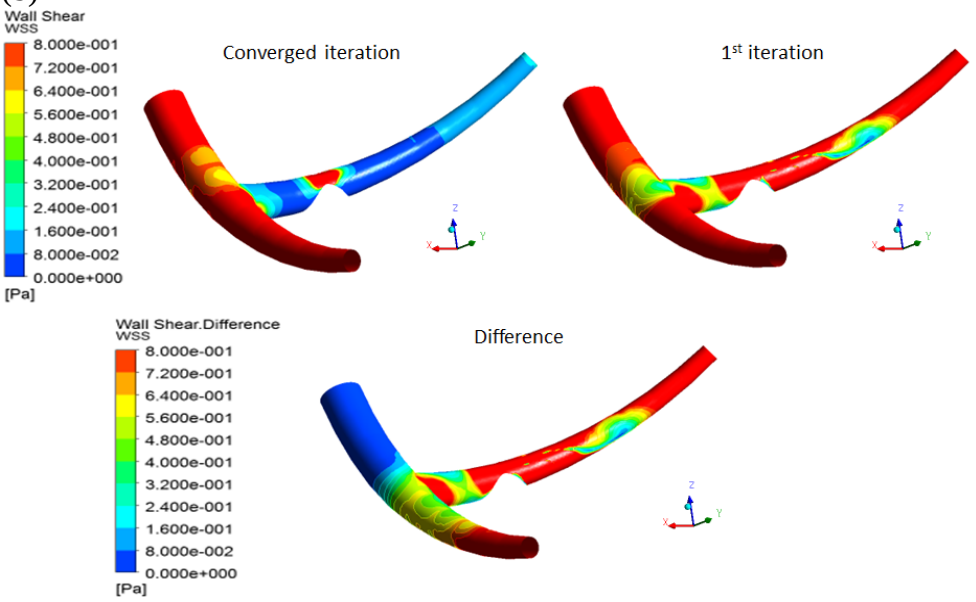

Figure 5.8. WSS contours of values up to 0.8Pa for pathological geometry evaluated at (a) the systolic time, t_1 and (b) the diastolic time, t_2. Comparison

between predictions of converged iteration and the first iteration (a,b). The global maximum WSS is 398Pa.

The illustrations of Fig. 8 show a remarkable difference between the predicted WSS values of the first iteration and those of the converged one. This difference emphasizes the need of adapting an iterative approach to ensure that the in-vivo conditions have been met. Moreover, by comparing the WSS contours of the converged iteration at Fig. 5a and 5b, we notice that higher stresses are predicted at the systolic time, which is in agreement with our results in Section 5.3.1.

5.4 Discussion

We have presented an efficient implementation of proper outlet BCs in simulations of blood flow in the left coronary artery. This is achieved through a hybrid approach, with a 1D impedance network model providing outlet conditions for the 3D simulations of interest. Emphasis is given to the development and application of an intermediate simulant model which ensures that the in-vivo BCs are consistently applied. We have followed the methodology first proposed by Johnson *et al*. (2011), albeit we have: (a) applied the analysis to more realistic geometrical models, (b) used the Shanks transformation to accelerate the convergence of the iteratively applied simulant model, and (c) performed a holistic numerical stability analysis to ensure that the displayed simulation results are not significantly affected by numerical error.

We have presented the results of this investigation in the form of two comparative cases. First, we compared the simulation output of a Newtonian fluid to that of a Casson fluid for a physiological (healthy) left coronary artery. This was done

to examine the impact of rheology on the CFD simulations and in particular on hematological parameters of interest, such as the WSS, low values of which are known to contribute to atherogenesis, the initial stage of atherosclerosis. The results have confirmed the importance of rheology in blood flow simulations, as evidenced by the important deviations between the WSS and the strain rate contours of the Newtonian and the Casson based simulations.

The second case regarded a comparison between the first and the converged iteration results of the simulation of flow in a pathological LCA geometry. Significant differences were observed in the magnitude of the reported WSS and the strain rate. These differences justify the use of the simulant model, whose purpose is to ensure that the application of the in-vivo boundary conditions, as obtained from the 1D-network impedance model, is performed in a consistent fashion. Moreover, the computational load required for the iterative application of the simulant model has been significantly decreased (at least 30%) by application of the Shanks transformation.

The accuracy of hybrid blood flow simulations can be improved by accounting for the main features of the proposed scheme, that is the rheology of blood through the Casson equation and a simulant model for the proper implementation of BCs. This would ensure that more accurate in vivo conditions are reached in the simulation, and that local fluid dynamics are better ascertained if correlation back to experimental and physical relevance is sought.

Chapter 6

CONCLUSIONS AND FUTURE WORK

6.1 Conclusions

In this thesis we have undertaken the task of improving the accuracy of blood flow simulations, with the ultimate goal of using blood flow modeling to improve diagnostic capabilities of cardiovascular-related diseases. The main avenue through which we have tried to achieve this goal is by offering a faithful representation of blood rheology.

In Chapter 2 we presented a systematic investigation of the rheology of normal human blood under steady state shear flow. Based on a comparison between a homogeneous (Couette) and non-homogeneous (Poiseuille) flows, we first showed that the simple flow hypothesis constitutes a reasonable assumption for blood under steady-shear flow. Then, we unequivocally showed that the Casson viscoplastic model is the one that naturally emerges as the best approximation of available experimental data. Consequently, we developed a parametrization of the Casson model parameters, the yield stress and the Casson viscosity, in terms of the physiological parameters of importance. A key contribution of this work is the realization that yield stress is an onset phenomenon only occurring when the hematocrit exceeds a critical value that depends on the fibrinogen concentration. Most importantly, we have established a relationship that connects the critical hematocrit with the fibrinogen concentration. Albeit the connection of yield stress to fibrinogen (a key plasma protein responsible for the development of red blood cell aggregates) is not new, it is the first time that this is made in such a direct, quantitative, fashion. Furthermore, beyond the onset, the dependence of the yield stress on the hematocrit is found to be through the square of its

difference from its critical value, further reinforcing the interpretation of yield stress as a critical, percolation-type, phenomenon. By adding the aforementioned features, the proposed Casson parametric model constitutes a complete, updated, and reliable model for the prediction of the rheology of normal (healthy) human blood.

Upon completion of the examination of normal human blood, we investigated the impact of particular pathological conditions on the steady state shear rheology. Specifically, we examined the impact that results from abnormal concentrations, both low and high, of cholesterol and triglycerides in human blood. While we showed that the Casson constitutive equation remains an appropriate model for the description of blood's rheology, it was clear that, due to the significant effects emanating from the abnormal levels of cholesterol and triglycerides, a new parametrization of the Casson viscosity and the yield stress was required. Our analysis has shown that the same ratios that physicians have found to be of importance in assessing the risks of hypercholesterolemia and hypertriglycerolaemia (LDL/HDL and TG/HDL) are also important in assessing the cholesterol and triglyceride effects on the model parameters. The natural emergence of certain ratios in the viscosity and yield stress correlations, such as LDL/HDL = 3.623, and TG/HDL = 3.2, point out naturally emerging target values that may end up having future medical significance.

Chapter 4 is one of the most important contributions of this thesis. We have presented the development of a thixotropic model that can be used to describe the transient shear flow of blood. The thixotropic approach allows the phenomenological description of the reversible aggregation of RBCs, and its use is even more justified in systems that exhibit a yield stress, as is the case with blood. A key feature of the proposed model is that under steady state conditions it reduces to the Casson parametric

model, which confirms the consistency of the proposed work. Furthermore, the new model makes use of only three additional parameters, with a specific physical meaning (a zero shear rate maximum strain, and two kinematic coefficients) and a known order of magnitude. Moreover, this is the first time that a blood flow model is validated extensively against a variety of transient blood flow data. The model shows good agreement with blood data stemming from triangular step-change, rectangular step-change, and LAOS experiments. In the last case, the predictions are rather semi-quantitative, however this can be justified by the incomplete characterization of the reported data (no steady state data and no fibrinogen concentration reported).

Finally, in Chapter 5 we examined the impact of the described shear rheology in arterial simulations of blood flow. We have simulated the flow in the left coronary artery (LCA), considering a healthy geometry and a pathological one with a stenosis developing in the left anterior descending (LAD) branch of the artery. The impact of the rheology was demonstrated by comparing the results of Newtonian simulations to those based on the Casson parametric model. In all of the examined cases, higher values of pressure profiles and the wall shear stress were predicted by the Casson model. This information can be of importance in the investigation of cardiovascular diseases (CVDs), as the WSS in human arteries is used as a hematological factor to assess the risk of atherogenesis, the initial stage of atherosclerosis. Furthermore, in the same work we have presented an efficient implementation of outflow boundary conditions in simulations of arterial flow. The proposed scheme relies on an iterative application of an intermediate simulant model which ensures consistency between the outflow conditions in the simulation and the hemodynamic predictions of a 1D network model for the same outlet. We have shown that there are important differences between

converged results with the use of the simulant model and the non-converged output which corresponds to the conventional way of carrying out arterial flow simulations. This is another factor affecting the accuracy, and therefore the physiological relevance, of the output of blood flow simulations.

The conclusions of this thesis are presented in compact form in Fig. 6.1.

Chapter 2

- Blood can be approximated as a simple fluid in steady state shear flows
- The Casson model is the best approximation of available experimental normal blood data in steady shear flows
- Parametrized the Casson model parameters (viscosity, yield stress) with respect to the physiological conditions (hematocrit (Hct), temperature, fibrinogen concentration)
- Modeled yield stress as an onset phenomenon, only occurring when Hct exceeds a critical value (Hct_C)
- Incorporated the effect of fibrinogen concentration in a direct, quantitative fashion **
- Accounted for the critical hematocrit and offered a connection of Hct_C to the fibrinogen concentration **

Chapter 3

- Investigated the impact of low and high cholesterol and triglycerides levels on human blood steady shear rheology
- The Casson constitutive eq. remains an appropriate model for the description of the rheology but a new parametrization of viscosity and yield stress is required
- The same ratios that physicians have found to be of importance in assessing the risks of hypercholesterolemia and hypertriglycerolaemia (LDL/HDL and TG/HDL), are also important in assessing the cholesterol and triglyceride effects on the model parameters **
- Naturally emerging target values of LDL/HDL and TG/HDL may end up having future medical significance

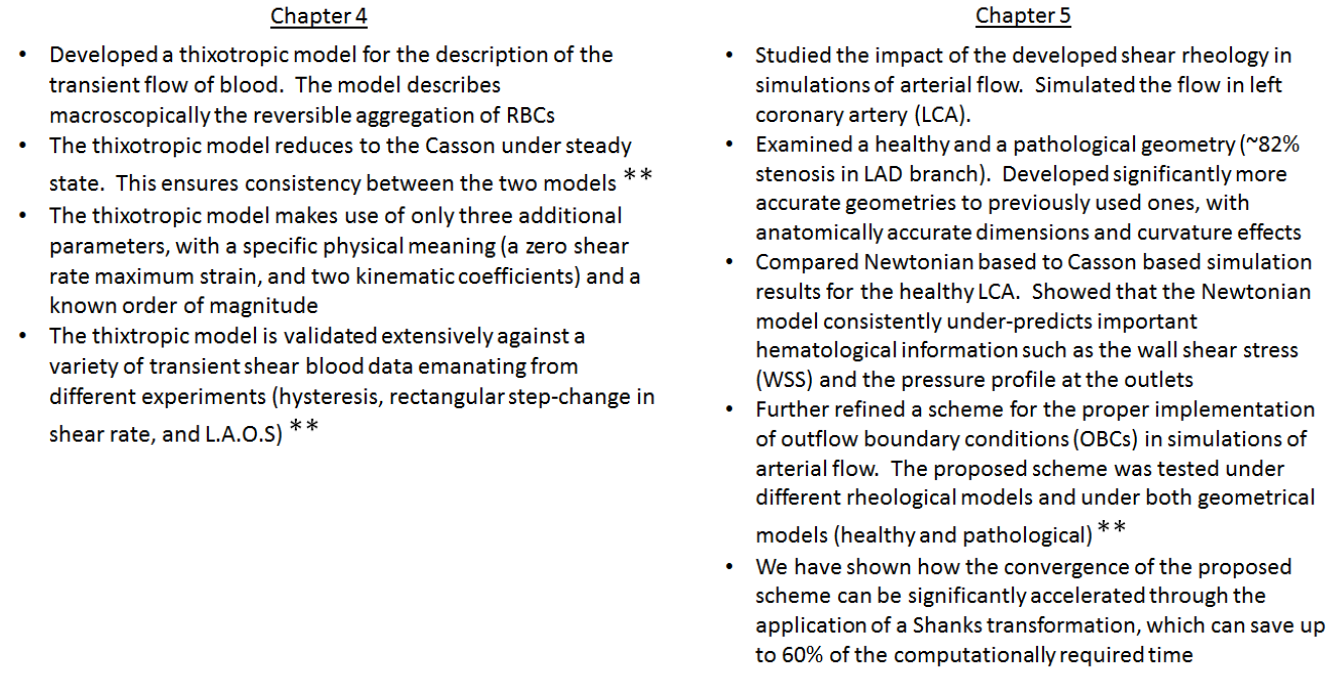

Figure 6.1. Summarized conclusions. The double asterisk symbol (**) denotes results/conclusions of this work that, to the best of our knowledge, constitute contributions to the field that are made for the first time.

4

6.2 Future Work

The conclusions of this work offer a better understanding of the rheology of blood, and therefore can lead to more accurate simulations of arterial flow. However, further improvements need to be made in the future, so that the model predictions can have a significant impact in the medical field, and in clinical applications.

In Chapter 3 we examined the impact of certain pathological conditions on the exhibited shear rheology of blood, under steady state conditions. The analysis conducted in Chapter 3 can serve as an example for future investigations. Merrill (1969)

has reported various pathologies that are invoked from abnormal levels of plasma proteins, such as hyperfibrinogenemia, anemia, polycythemia, hyperlipemia and others. Similarly to the work of Chapter 3, investigators can re-parametrize an existing rheological model so that they describe the reported data or they identify new correlations, as the ratio indices that emerged in Chapter 3, that are relevant to the respective pathologies. Such updated rheological models would contribute accumulatively to a deeper understanding of blood's rheology. Moreover, this is another example of how the rheology of blood can contribute towards the improvement of diagnostic capabilities. For instance, if a ratio of the concentration of certain proteins is found to correlate strongly with a specific pathological behavior, and this correlation is not known a priori, then this information can be used to detect or predict the occurrence of a pathology.

Then, in Chapter 4, we undertook the important task of describing macroscopically the rheology of blood under transient shear conditions. The work of Chapter 4 has unveiled important limitations in the rheological reports of transient blood flow studies. For instance, while the important role of plasma proteins, such as the fibrinogen, is documented in theory, such information is rarely reported in rheological studies. This is also the case with the lipoproteins and cholesterol concentrations, which, as shown in Chapter 3, can significantly affect the rheology of blood. Such information should be reported not only when studying pathological cases, but also in the case of physiological studies, as in that case: a. the reported data would serve as a verification of the fact that the respective blood sample is indeed normal, and b. the reported protein concentrations could be used for the improvement

of existing models or for the development of more reliable ones. Therefore, there is a need for a more complete characterization of blood samples, in rheological studies.

The frequently incomplete characterization of blood in the rheological studies limits the reliability and the predictability of the developed blood flow models. While Chapters 2-4 offer, for the first time, a complete and systematic description of the shear flow of blood under both steady state (Chapters 2-3) and transient (Chapter 4) conditions, extending this analysis to complex, general flows, while maintaining the systematic approach that we have thus far followed, seems impossible. Even in sophisticated tensorial blood models that have been proposed for the description of complex flow, arbitrary parameters that lack a physical meaning are typically employed. This occurs despite the fact that the proposed models aim at the description of specific blood samples and are not a product of a systematic approach that aims at parameterizing the main features of a model so that it can be used to describe the flow of any blood sample. Obviously, the level of difficulty in the latter case would be higher, and so is the need of more blood data that are fully characterized. However, provided that such information can be obtained in the short future, the development of a tensorial, and thermodynamically consistent model would significantly improve the predictability of blood's rheology in the human arterial network.

The relevance of CFD investigations of arterial flow, and the acquired physiological data such as the pressure and flow data or the WSS profiles, can be further improved in the future. The next step in capturing the complex blood rheology in simulations of flow is to account for the time-dependent rheological effects, i.e. the thixotropy of blood. This is a feature that is currently not addressed in CFD simulations as, in the best case, the investigators incorporate generalized Newtonian

models which, by definition, cannot describe time-dependent effects, such as the history-dependent flow of materials. The challenge in this case would be to account for this feature without adding the need of excessive computational demands, as such a development would limit the scope of translating our work into an easily accessed diagnostic tool. Thus, a phenomenological way of incorporating thixotropy into CFD would need to be employed. Of course, to ensure realistic results, the rheology features discussed in this thesis would need to merge with the fluid-structure interactions (FSI) so as to account for important physiological features like the vessel compliance and tethering.

REFERENCES

Alastruey, J., K.H. Parker, J. Peiró, S.M. Byrd, and S.J. Sherwin, “Modeling the circle of Willis to assess the effects of anatomical variations and occlusions on cerebral flows,” J. Biomech. **40**, 1794-1805 (2007).

Alastruey, J., S. M. Moore, K.H. Parker, T. David, J. Peiró, and S.J. Sherwin, “Reduced modeling of blood flow in the cerebral circulation: Coupling 1-D, 0-D and cerebral autoregulation models,” Int. J. Numer .Meth. Fluids **56**, 1061-1067 (2008).

Anand, M., and K. Rajagopal, ‘‘A shear-thinning viscoelastic fluid model for describing the flow of blood,’’ Int. J. Cardiovascular Medicine and Science **4**, 59-68 (2004).

Anand, M., J. Kwack, and A. Masud, "A new generalized Oldroyd-B model for blood flow in complex geometries," International Journal of Engineering Science **72**, 78-88 (2013).

Apostolidis, A. J., and A. N. Beris, “Modeling of the blood rheology in steady-state shear flows,” J. Rheol., **58**, 607-633 (2014).

Apostolidis, A. J., M. J. Armstrong, and A. N. Beris, “Modeling of human blood rheology in transient shear flows,” J. Rheol. **59**, 275-298 (2015).

Armstrong, M.J., Beris, A.N. and Wagner, N.J., “Dynamic Data-Driven Parameter Estimation of Nonlinear Models Based on a Parallel Simulated Annealing Method,” submitted to Computers in Chemical Engineering, Nov. 2014 Ms. Ref. No.: CACE-D-14-00579.

Balescu, R., *Statistical Dynamics. Matter out of Equilibrium* (Imperial College Press, London, 1997).

Barbee, J. H. and G. R. Cokelet, “Prediction of blood flow in tubes with diameters as small as 29 microns,” Microvascular Research **3**, 17-21 (1971).

Barbee, J. M., “The flow of human blood through capillary tubes with inside diameters between 8.7 and 221 microns,” Ph.D. Thesis, California Institute of Technology (1971).

Barnes, H. A, “The yield stress—a review or ‘πάντα ρει’—everything flows?,” J.Non-Newtonian Fluid Mech. **81**, 133-178 (1999).

Barnes, H. A., "Thixotropy: A review," J. Non-Newtonian Fluid Mech. **70**, 1-33 (1997).

Batzel, J.J., F. Kappel, D. Schneditz, and H.T. Tran, *Cardiovascular and Respiratory Systems. Modeling, Analysis, and Control.* SIAM: Philadelphia (2007).

Beris, A.N. and V.G. Mavrantzas, "On the compatibility between various macroscopic formalisms for the concentration and flow of dilute polymer solutions," J. Rheol. **38**, 1235-1250 (1994).

Beris, A.N., and B.J. Edwards, Thermodynamics of Flowing Systems with Internal Microstructure. Oxford U. Press: New York (1994).

Bernabeu, M. O., R. W. Nash, D. Groen, H. B. Carver, J. Hetherington, T. Krüger, and P. V. Coveney, "Impact of blood rheology on wall shear stress in a model of the middle cerebral artery," Interface Focus **3**, 20120094 (2013)

Bevan, R.L.T., P. Nithiarasu, R. Van Loon, I. Sazonov, H. Luckraz, and A. Garnham, "Application of a locally conservative Galerkin (LCG) method for modelling blood flow through a patient-specific carotid bifurcation," Int J Numer Meth Fluids **64**, 1274-1295 (2010).

Bird, R. B., R. C. Armstrong, and O. Hassager, *Dynamics of Polymeric Liquids 1. Fluid Mechanics* (Wiley, New York, 1977).

Bird, R.B., G.C. Dai, and B.J. Yarusso, "The rheology and flow of viscoplastic materials," Reviews in Chem Engrg 1, 1-70 (1983).

Bird, R.B., R.C. Armstrong, and O. Hassager, Dynamics of Polymeric Fluids. vol. 1, 2nd ed., Wiley-Interscience: New York (1987).

Boutsianis, E., S. Gupta, K. Boomsma, and D. Poulikakos, "Boundary Conditions by Schwarz-Christoffel Mapping in Anatomically Accurate Hemodynamics," Annals of Biomedical Engineering **36**(12), 2068–2084 (2008).

Brinkman, A.M., P.B. Baker, W.P. Newman, R. Vigorito, and M.H. Friedman, "Variability of human coronary artery geometry: An angiographic study of the left anterior descending arteries of 30 autopsy hearts," Annals of Biomedical Engineering **22**, 34-44 (1994).

Bureau, M., J. C. Healy, D. Bourgoin, and M. Joly, "Etude rhéologique en régime transitoire de quelques échantillons de sangs humains artificiellement modifiés," Rheologica Acta **18**, 756-768 (1979).

Bureau, M., J. C. Healy, D. Bourgoin, and M. Joly, ''Rheological Hysteresis of Blood at Low Shear Rate,'' Biorheology **17**, 191-203 (1980).

Byoung-Kwon, L. “Computational Fluid Dynamics in Cardiovascular Disease,” Korean Circulation Journal **41**, 423-430 (2011).

Campo-Deaño, L., M. S. N. Oliveira, and F. T. Pinho, “A review of computational hemodynamics in middle cerebral aneurysms and rheological models for blood flow,” Appl. Mech. Rev., **67** (3), 1-16 (2015).

Casson, N., “Flow equations for pigment-oil suspensions of the printing ink type,” in *Rheology of Dispersed Systems*, edited by C. C. Mill (Pergamon Press, New York, (1959), pp. 84-104.

Cebral, J. R., P. J. Yim, R. Löhner, O. Soto, and P. L. Choyke, “ Blood flow modeling in carotid arteries with computational fluid dynamics and MR imaging,” Acad. Radiol. **9**, 1286-99 (2002).

Cecchi, E., C. Giglioli, S. Valente, C. Lazzeri, G. F. Gensini, R. Abbate, and L. Mannini, “Role of hemodynamic shear stress in cardiovascular disease,” Atherosclerosis **214**, 249–256 (2011).

Chaichana, T., S. Zhonghua, and J. Jewkes, “Computational fluid dynamics analysis of the effect of plaques in the left coronary artery,” Comput. Math. Methods Med., 2012:504367 (2012).

Chandran, K.B., S.E. Rittgers, and A.P. Yoganathan, *Biofluid Mechanics. The Hyman Circulation, 2nd Ed.* CRC Press: Boca Raton (2012).

Changizi, M.A., and C. Cherniak, “Modeling the large-scale geometry of human coronary arteries,” *Canadian Journal of Physiology and Pharmacology* **78**, 603-611 (2000).

Cheer, A.Y., and C. P. van Dam (Eds.), *Fluid Dynamics in Biology (Contemporary Mathematics vol. 141).* American Mathematical Society: Providence (1993).

Chien, S., S. Usami, H. M. Taylor, J. L. Lundberg, and M. I. Gregersen, “Effects of hematocrit and plasma proteins on human blood rheology at low shear rates,” J. Appl. Physiol. **21**, 81-87 (1966).

Chien, S., S. Usami, R. J. Dellenback, and C. A. Bryant, "Comparative Hemorheology-Hematological implications of species differences in blood viscosity," Biorheology **8**, 35-57 (1971).

Chien, S., S. Usami, R.J. Dellenback, M.I. Gregersen, “Shear dependent deformation of erythrocytes in rheology of human blood,” Am. J. Physiol. **219**,136-142 (1970).

Cho, Y.I., and K.R. Kensey KR, “Effects of the non-Newtonian viscosity of blood on flows in a diseased arterial vessel. Part 1: steady flows,” Biorheology **28**,241–262 (1991).

Clipp, R.B., and B.N. Steele, “Impedance Boundary Conditions for the Pulmonary Vasculature Including the Effects of Geometry, Compliance, and Respiration,” IEEE Transactions On Biomedical Engineering **56**(3): 862-870 (2009).

Cokelet, G. R., E. W. Merrill, E. R. Gilliland, H. Shin, and A. Britten, “The rheology of human blood – Measurement near and at zero shear rate,” Trans. Soc. Rheol. 7, 303-317 (1963).

Cowan, A. Q., D. J. Cho, and R. S. Rosenson RS, “Importance of blood rheology in the pathophysiology of atherosclerosis,” Cardiovasc. Drugs Ther. **26**, 339-348 (2012).

Crowley, J.P., J. Metzger, A. Assaf, R.C. Carleton, E. Merrill, and C.R. Valeri, “Low density lipoprotein cholesterol and whole blood viscosity,” Ann. Clin. Lab. Sci. **24**, 533–541 (1994).

Dimitriou C. J., R. H. Ewoldt, and G. H. McKinley, "Describing and prescribing the constitutive response of yield stress fluids using large amplitude oscillatory shear stress (LAOStress)," Journal of Rheol. **57**(1), 27-70 (2013)

Dintenfass, L., “Thixotropy of Blood and Proneness to Thrombus Formation,” Circ. Res. **11**, 233-239 (1962).

Dodge, J.T. Jr., B. G. Brown, E. L. Bolson, H. T. Dodge, “Lumen diameter of Normal Human Coronary Arteries. Influence of age, sex, anatomic variation, and left ventricular hypertrophy or dilation,” Circulation **86**, 232-246 (1992).

Dong, J., Z. Sun, K. Inthavong, and J. Tu, “Fluid-structure interaction analysis of the left coronary artery with variable angulation,” Comput. Methods Biomech. Biomed. Engin. **18**(14), 1500-1508 (2015).

Drzewiecki, G.M., and J.K.-J. Li, Analysis and Assessment of Cardiovascular Function. Springer-Verlag: New York (1998).

Dullaert, K., and J. Mewis, "A structural kinetics model for thixotropy," J. Non-Newtonian Fluid Mech. **139**, 21-30 (2006).

Edwards, A. L., *Multiple Regression and the Analysis of Variance and Covariance* (W. H. Freeman and Co., San Francisco, 1979).

erythrocyte aggregation,” Am. J. Physiol. **271**, H2346-H2352 (1996).

Esmaily-Moghadam, M., I. E. Vignon-Clementel, R. Figliola, and A. L. Marsden, “A modular numerical method for implicit 0D/3D coupling in cardiovascular finite element simulations,” Journal of Computational Physics, **244**, 63-79 (2013).

Fähraeus, R. “The suspension stability of blood,” Physiol. Rev. **9**, 241-274 (1929).

Fähraeus, R., and T. Lindqvist, “The viscosity of blood in narrow capillary tubes,” Am. J. Physiol. **96**, 562-568 (1931).

Fahy, P., P. Delassus, P. McCarthy, S. Sultan, N. Hynes, and L. Morris, ”An In Vitro Assessment of the Cerebral Hemodynamics Through Three Patient Specific Circle of Willis Geometries,” J. Biomech. Engrg -Transactions Of The ASME **136**, 011007 (2014).

Fang, J. N., and R. G. Owens, ‘‘Numerical simulations of pulsatile blood flow using a new constitutive model,’’ Biorheology **43**, 637-660 (2006).

Fedosov, D. A., B. Caswell, and G. Em. Karniadakis, “A multiscale red blood cell model with accurate mechanics, rheology and dynamics,” Biophysical Journal **98**, 2215-2225 (2010).

Fedosov, D. A., W. Pan, B. Caswell, G. Gompper, and G. Em. Karniadakis, “Predicting human blood viscosity in silico,” PNAS **108**, 11772-11777 (2011).

Fedosov, D.A., B. Caswell, A.S. Popel, and G.E. Karniadakis, “Blood Flow and Cell-Free Layer in Microvessels,” Microcirculation **17**, 615-628 (2010).

Fedosov, D.A., H. Noguchi, and G. Gompper, “Multiscale modeling of blood flow: from single cells to blood rheology,” Biomech. Model Mechanobiol. **13**, 239-258 (2014).

Figueroa, C.A., I.E. Vignon-Clementel, K.E. Jansen, T.J.R. Hughes, and C.A. Taylor, “A Coupled Momentum Method for Modeling Blood Flow in Three-Dimensional Deformable Arteries,” Comput. Methods Appl. Mech. Eng., **195**(41–43), 5685–5706 (2006).

Formaggia, L., A. Quarteroni, and A. Veneziani (eds). “Cardiovascular Mechanics; Volume 1. Modeling and Simulation of the Circulatory System,” Springer: Italia, Milano (2009).

Formaggia, L., J. F. Gerbeau, F. Nobile, and A. Quarteroni, “On the coupling of 3D and 1D Navier–Stokes equations for flow problems in compliant vessels,” Computational Methods on Applied Mechanics and Engineering, **191**, 561–582 (2001).

Forti, N., and J. Diament "High-density lipoproteins: metabolic, clinical, epidemiological and therapeutic intervention aspects. An update for clinicians," Arq. Bras. Cardiol. **87**, 614-622 (2006).

Frauenfelder, T., E. Boutsianis, T. Schertler, L. Husmann, S. Leschka, D. Poulikakos, B. Marincek, and H. Alkadhi, "In-vivo flow simulation in coronary arteries based on computed tomography datasets:feasibility and initial results," Eur. Radiol. **17**, 1291–1300 (2007).

Friedman, M.H., P.B. Baker, Z. Ding, B.D. Kuban, "Relationship between the geometry and qualitative morphology of the left anterior descending coronary artery," Arteriosclerosis **125**, 183-192 (1996).

Fung, Y.C., *Biomechanics. Circulation, 2nd Ed.* Springer-Verlag: New York (1997).

Galdi, G.P., R. Rannacher, A.M. Robertson, and S. Turek S, (Eds.), *Hemodynamical Flows. Modeling, Analysis and Simulation.* Birkhäuser: Basel (2008).

Galindo-Rosales, F.J., L. Campo-Deaño, P.C. Sousa, V. M. Ribeiro, M.S.N. Oliveira, M.A. Alves, and F.T. Pinho, "Viscoelastic instabilities in micro-scale flows," Experimental Thermal and Fluid Science 59, 128-129 (2014)

Gay, M., and L. Zhang, "Numerical studies of blood flow in healthy, stenosed, and stented carotid arteries," International Journal for Numerical Methods in Fluids **61**, 453-472 (2009).

Gijsen, F. J. H., F. N. van de Vosse, and J. D. Janssen, "The influence of the non-Newtonian properties of blood on the flow in large arteries: Steady flow in a carotid artery bifurcation model," Journal of Biomechanics **32**, 601-608 (1999).

Gijsen, F.J.H., E. Allanic, F.N. van de Vosse, J.D. Janssen, "The influence of the non-Newtonian properties of blood on the flow in large arteries: unsteady flow in a 90 degrees curved tube," Journal of Biomechanics **32**, 705-713 (1999b).

Gonzalez, H.A., and N.O. Moraga, "On predicting unsteady non-Newtonian blood flow," Appl. Math. Comput. **170**(2), 909–923 (2005).

Grinberg, L., and G.E. Karniadakis, "Outflow boundary conditions for arterial networks with multiple outlets," Annals of Biomedical Engineering 36(9), 1496-1514 (2008).

Happel, J., and H. Brenner, *Low Reynolds number hydrodynamics* (Martinus Nijhoff Publishers, Hague, Netherlands, 1983).

Haynes, R.H., and A.C. Burton, “Role of the non-Newtonian behavior of blood in hemodynamics,” Am. J. Physiol. **197**(5), 943-950 (1959).

Herschel, W. H. and R. Bulkley, "Konsistenzmessungen von Gummi-Benzollösungen", Kolloid Zeitschrift **39**, 291–300 (1926).

Huang, C.R., W.D. Pan, H.Q. Chen,, and A.L. Copley, “Thixotropic properties of whole blood,” Biorheology **24**, 795-801 (1987).

Hutchins, G.M., M.M. Miner, and J.K. Boitnott, “Vessel caliber and branch-angle of human coronary artery branch-points,” Circulation Research **38**, 572-576 (1976).

Iida, N. “Influence of plasma layer on steady blood flow in microvessels,” Jpn. J. Appl. Phys. **17**, 203–214 (1978).
J. Rheol. 57, 27-70 (2013); doi: 10.1122/1.4754023

Johnson, D. A., J. R. Spaeth, W. C. Rose, U. P. Naik, and A. N. Beris, “An impedance model for blood flow in the human arterial system. Part I: Model development and MATLAB implementation,” Computers and Chemical Engineering, **35**, 1304-1316 (2011b).

Johnson, D. A., U. P. Naik, and A. N. Beris, “Efficient implementation of the proper outlet flow conditions in blood flow simulations through asymmetric arterial bifurcations,” International Journal for Numerical Methods in Fluids, 66, 1383-1408 (2011a).

Johnston, B. M., P. R. Johnston, S. Corney, and D. Kilpatrick, “Non-Newtonian blood flow in human right coronary arteries: Transient simulations,” Journal of Biomechanics, **39**, 1116-1128 (2006)

Joseph, D.D., Fluid Mechanics of Viscoelastic Liquids. Springer-Verlag: New York (1990).

Jung, J., and A. Hassanein, “Three-phase CFD analytical modeling of blood flow,” Medical Engineering & Physics **30**, 91-103 (2008).

Kabinejadian, F., and D. V. Ghista, “Compliant model of a coupled sequential coronary arterial bypass graft: Effects of vessel wall elasticity and non-Newtonian rheology on blood flow regime and hemodynamic parameters distribution,” Medical Engineering & Physics, **34**, 860-872 (2012).

Kamenskiy A.V., J.N. MacTaggart, I.I. Pipinos, J. Bikhchandani, and Y.A. Dzenis, “Three-Dimensional Geometry of the Human Carotid Artery,” J Biomech Engrg - Transactions ASME **134**, 064502 (2012).

Kampmeyer, P. M., "The temperature dependence of viscosity for water and mercury," J. Appl. Phys. **23**, 99-102 (1952).

Karimi, S., M. Dabagh, P. Vasana, M. Dadvar, B. Dabir, and P. Jalali, "Effect of rheological models on the hemodynamics within human aorta: CFD study on CT image-based geometry," Journal of Non-Newtonian Fluid Mechanics, **207**, 42-52 (2014).

Kato, M., K. Dote, S. Habara, H. Takemoto, K. Goto, and K. Nakanoka, "Clinical implications of carotid artery remodeling in acute coronary syndrome. Ultrasonographic assessment of positive remodeling," J. Am. College Cardiology **42**, 1026-1032 (2003).

Keener, J., and J. Sneyd, Mathematical Physiology. Springer, New York (1998).

Kensey, K. R. "Rheology: An overlooked component of vascular disease," Clin. Appl. Thrombosis/Hemostasis **9**(2), 93-99 (2003).

Koenig, W., M. Sund, E. Ernst, W. Mraz, V. Hombach, and U. Keil, "Association between rheology and components of lipoproteins in human blood - results from the MONICA project," Circulation **85**(6), 2197-2204 (1992).

Korson, L., W. Drosthan, and F. J. Millero, "Viscosity of water at various temperatures," Journal of Physical Chemistry **73**, 34-39 (1969).

Ku, D.N., "Blood flow in arteries," Annual Review of Biomedical Engineering **29**, 399-434 (1997).

Ku, D.N., D.P. Giddens, C.K. Zarins, and S. Glagov, "Pulsatile flow and atherosclerosis in the human carotid bifurcation-positive correlation between plaque location and low oscillating shear stress," Arteriosclerosis, **5**, 293-302 (1985).

Kwiterovich Jr, P. O. "The metabolic pathways of high-density lipoprotein, low-density lipoprotein, and triglycerides: a current review," Am. J. Cardiol. **86**, 5L-10L (2000).

Lassaline, J. V., and B. C. Moon, "A computational fluid dynamics simulation study of coronary blood flow affected by graft placement," Inter. Cardiovasc. Thorac. Surg., 1-5 (2014) .

Lee, B. K., S. Xue, J. Nam, H. Lim, and S. Shin, "Determination of the blood viscosity and yield stress with a pressure-scanning capillary hemorheometer using constitutive models," Korea-Australia Rheology Journal **23**, 1-6 (2011).

Lee, J. S., "Pressure-flow relationships of single vessels and organs," in Microcirculation, edited by G. Kaley, and B. M. Altura (University Park Press, Baltimore, 1977), Vol. 1, pp. 365-390.

Lee, K. W., and X. Y. Xu, "Modelling of flow and wall behavior in a mildly stenosed tube," Medical Engineering and Physics **24**, 575-586 (2002).

Lee, S.W., and D.A. Steinman, "On the relative importance of rheology for image-based CFD models of the carotid bifurcation," J. Biomech. Engrg-Transactions ASME **129**, 273-278 (2007).

Lei, H., and G. Em. Karniadakis, "Quantifying the rheological hemodynamics characteristics of sickle cell anemia," Biophysical Journal **102**, 185-194 (2012).

Levesque, M.J., D. Liepsch, S. Moravec, and R.M. Nerem, "Correlation of endothelial cell shape and wall shear stress in a stenosed dog aorta," Arteriosclerosis, Thrombosis, and Vascular Biology **6**, 220-229 (1986).

Li, J.K.-J., "Dynamics of the Vascular System (Series on Bioengineering and Biomedical Engineering – Vol. 1)," World Scientific: Singapore (2004).

Li, J.K.-J., "The Arterial Circulation. Physical Principles and Clinical Applications," Humana Press: Totowa, New Jersey (2000).

Li, X.J., Z.L. Peng, H. Lei, M. Dao, and G.E. Karniadakis, "Probing red blood cell mechanics, rheology and dynamics with a two-component multi-scale model," Philosophical Transactions Of The Royal Society A-Mathematical Physical And Engineering Sciences **372**: SI Article Number: 20130389 (2014).

Li, Y., X.X. Tian, T. Liu, and R.T. Wang, "Association between whole blood viscosity and arterial stiffness in patients with type 2 diabetes mellitus," Endocrine **49**(1), 148-154 (2015).

Liu, X., Y. Fan, X. Deng, and F. Zhan, "Effect of non-Newtonian and pulsatile blood flow on mass transport in the human aorta," J. Biomech., **44**, 1123–1131 (2011).

Malek, A.M., S. L. Alper, and S. Izumo, "Hemodynamic shear stress and its role in atherosclerosis," Journal of American Medical Association **282**(21), 2035-2042 (1999).

Marcinkowska-Gapińska A., J. Gapiński, W. Elikowski, F. Jaroszyk, and L. Kubisz, "Comparison of three rheological models of shear flow behavior studied on blood samples from post-infarction patients," Med. Bio. Comput., **45**, 837-844 (2007).

Marsden, A., and M. Esmaily-Moghadam, “Multiscale Modeling of Cardiovascular Flows for clinical decision support,” Applied Mechanics Review **67**(3), 030804 (2015).

Meiselman, H. J., E. W. Merrill, E. W. Salzman, E. R. Gillilan, and G. A. Pelletier, ‘‘Effect of Dextran on Rheology of Human Blood - Low Shear Viscometery,’’ Journal of Applied Physiology **22**, 480-486 (1967).

Merrill, E. W., ‘‘Rheology of Blood,’’ Physiological Reviews **49**, 863-888 (1969).

Merrill, E. W., A. M. Benis, E. R. Gillilan, T. K. Sherwood, and E. W. Salzman, ‘‘Pressure-Flow Relations of Human Blood in Hollow Fibers at Low Rates,’’ Journal of Applied Physiology **20**, 954-967 (1965).

Merrill, E. W., and G. A. Pelletier, “Viscosity of human blood: transition from Newtonian to non-Newtonian,” Journal of Applied Physiology **23**, 178-82 (1967).

Merrill, E. W., C. S. Cheng, and G. A. Pelletier, ‘‘Yield Stress of Normal Human Blood as a Function of Endogenous Fibrinogen,’’ Journal of Applied Physiology **26**, 1-3 (1969).

Merrill, E. W., E. R. Gilliland, G. Cokelet, H. Shin, A. Britten, and R. E. Jr. Wells, “Rheology of human blood, near and at zero flow: Effects of temperature and hematocrit level,” Biophysical Journal **3**, 199-213 (1963a).

Merrill, E. W., E. R. Gilliland, T. S. Lee, and E. W. Salzman, “Blood Rheology: Effect of Fibrinogen Deduced by Addition,” Circ. Res. **18**, 437-446 (1966).

Merrill, E. W., G. C. Cokelet, A. Britten, and R. E. Wells Jr., “Non-Newtonian rheology of human-blood-Effect of fibrinogen deduced by “Subtraction,” Circ. Res. **13**, 48-55 (1963b).

Merrill, E. W., H. Shin, G. Cokelet, E. R. Gilliland, R. E. Wells, and A. Britten, ‘‘Rheology of Human Blood, near and at Zero Flow - Effects of Temperature and Hematocrit Level,’’ Biophysical Journal **3**, 199-213 (1963).

Merrill, E.W., A.M. Benis, E.R. Gilliland, T.K. Sherwood, and E.W. Salzman, “Pressure-flow relations of human blood in hollow fibers at low flow rates,” J. Appl. Physiol. **20**, 954-967 (1965).

Mewis, J., "Thixotropy: A general review," J. Non-Newtonian Fluid Mech. **6**, 1-20 (1979).

Mewis, J., and N. J. Wagner, Colloidal Suspension Rheology (Cambridge University, Cambridge, UK, 2012).

Milner, J.S., J.A. Moore, B.K. Rutt, and D.A. Steinman, "Hemodynamics of human carotid artery bifurcations: Computational studies with models reconstructed from magnetic resonance imaging of normal subjects," J. Vasc. Surg. **27**, 143-56 (1998).

Moore, S., T. Davida, J.G. Chasea, J. Arnolda, and J. Fink, "3D models of blood flow in the cerebral vasculature," J. Biomech. **39**, 1454–1463 (2006).

Morbiducci, U., D. Gallo, D. Massai, R. Ponzini, M.A. Deriu, L. Antiga, A. Redaelli, and F.M. Montevecchi, "On the importance of blood rheology for bulk flow in hemodynamic models of the carotid bifurcation" J. Biomech. **44**, 2427-2438 (2011).

Morbiducci, U., R. Ponzini, D. Gallo, C. Bignardi, and G. Rizzo, "Inflow boundary conditions for image-based computational hemodynamics: impact of idealized versus measured velocity profiles in the human aorta," J. Biomech., **46**, 102-109 (2013).

Moreno, L., F. Calderas, G. Sanchez-Olivares, L. Medina-Torres, A. Sanchez-Solis, and O. Manero, "Effect of cholesterol and triglycerides levels on the rheological behavior of human blood," Korea-Australia Rheol. J. **27**(1), 1-10 (2015).

Morris, C. L., D. L. Rucknagel, R. Shukla, R. A Gruppo, C. M. 2nd Smith, and P. Jr. Blackshear, "Evaluation of the Yield Stress of Normal Blood as a Function of Fibrinogen Concentration and Hematocrit," Microvascular Research **37**, 323-338 (1989).

Moyers-Gonzalez, M., R. G. Owens, and J. F. Fang, ''A non-homogeneous constitutive model for human blood. Part 1. Model derivation and steady flow,'' Journal of Fluid Mechanics **617**, 327-354 (2008).

Mujumdar, A., A. N. Beris, and A. B. Metzner, ''Transient phenomena in thixotropic systems,'' Journal of Non-Newtonian Fluid Mechanics **102**, 157-178 (2002).

Nemerson, Y., and V.T. Turrito, "The effect of flow on hemostasis and thrombosis," Thrombosis and Haemostasis **66**, 272-276 (1991).

Nguyen, K.T., C.D. Clark, T.J. Chancellor, and D.V. Papavassiliou, "Carotid geometry effects on blood flow and on risk for vascular disease," Journal of Biomechanics **41**, 11-19 (2008).

Nichols, W.W., and M.F. O'Rourke, *McDonald's Blood Flow in Arteries. Theoretical, Experimental and Clinical Principles, 4th Ed.* Arnold: London (1998).

Nissen, S.E., J.C. Gurley, C.L. Grines, D.C. Booth, R. McClure, M. Berk, C. Fischer, and A.N. DeMaria, "Intravascular ultrasound assessment of lumen size and wall

morphology in normal subjects and patients with coronary artery disease," Circulation **84**, 1087-1099 (1991).

Olufsen, M. S., C. S. Peskin, W. Y. Kim, E. M. Pedersen, A. Nakim, and J. Larsen, "Numerical simulation and experimental validation of blood flow in arteries with structured-tree outflow conditions," Ann. Biomed. Eng. **28**, 1281-1299 (2000).

Owens, R. G., ''A new micro structure-based constitutive model for human blood,'' Journal of Non-Newtonian Fluid Mechanics **140**, 57-70 (2006).

Owens, R. G., M. Moyers-Gonzalez, and J. Fang, ''On the simulation of steady and oscillatory blood flow in a tube using a new non-homogeneous constitutive model,'' Biorheology **45**, 83-84 (2008).

Passerini, T., M. de Luca, L. Formaggia, A. Quarteroni, and A. Veneziani, "A 3D/1D geometrical multiscale model of cerebral vasculature," Journal of Engineering Mathematics **64**, 319-330 (2009).

Peattie, R.A., R.J. Fisher, J.D.Bronzino, and D.R. Peterson, *Transport Phenomena in Biomedical Engineering. Principles and Practices.* CRC Press: Boca Raton, Florida (2013).

Pedley, T., *The Fluid Mechanics of Large Blood Vessels*. Cambridge University Press (1980).

Perktold, K., M. Hofer, G. Rappitsch, M. Loew, B.D. Kuban, and M.H. Friedman, "Validated computation of physiologic flow in a realistic coronary artery branch," Journal of Biomechanics **31**, 217-228 (1998).

Picart, C., J. M. Piau, and H. Galliard, "Human blood shear yield stress and its hematocrit dependence," Journal of Rheology **42**, 1-12 (1998).

Picart, C., P. H. Carpentier, H. Galliard, and J.-M. Piau, "Blood yield stress in systemic sclerosis," Am. J. Physiol. Heart Circ. Physiol. **276**, 771-777 (1999)

Pries, A. R., D. Neuhaus, and P. Gaehtgens, "Blood viscosity in tube flow: dependence on diameter and hematocrit," Am. J. Physiol. **263**, 1770-1778 (1992).

Pries, A. R., T.W. Secomb, P. Gaehtgens, and J. F. Gross, "Blood flow in microvascular networks. Experiments and simulation," Circ. Res. **67**, 826-834 (1990).

Quarteroni, A., and A. Veneziani, "Analysis of a geometric model based on the coupling of ODEs and PDEs for blood flow simulations," Multiscale Modeling and Simulation **1**, 173-195 (2003).

Quemada, D. “Rheology of concentrated disperse system. III. General features of the proposed non-Newtonian model. Comparison with experimental data,” Rheol. Acta **17**, 643–653 (1978b).

Quemada, D. “Rheology of concentrated disperse systems. II. A model for non-Newtonian shear viscosity in steady flows,” Rheol. Acta **17**, 632-642 (1978a).

Rajagopal, K. R., and A. R. Srinivasa, ‘‘A thermodynamic frame work for rate type fluid models,’’ Journal of Non-Newtonian Fluid Mechanics 88, 207-227 (2000).

Ramaswamy, S.D., S.C. Vigmostad, A. Wahle, Y.-G. Lai, M.E. Olszewski, K.C. Braddy, T.M.H. Brennan, J.D. Rossen, M. Sonka, K.B. Chandran, “Fluid Dynamic Analysis in a Human Left Anterior Descending Coronary Artery with Arterial Motion,” Annals of Biomedical Engineering **32**(12), 1628–1641 (2004).

Rao, M.A., Rheology of Fluid, Semisolid, and Solid Foods: Principles and Applications. Springer: New York (2014).

Remington, J. W., and E. H. Wood, “Formation of peripheral pulse contour in man,” Journal of Applied Physiology **9**, 433-442 (1956).

Reymond, P., F. Perren, F. Lazeyras, and N. Stergiopulos, “Patient-specific mean pressure drop in the systemic arterial tree, a comparison between 1-D and 3-D models,” J. Biomech **45**, 2499-2505 (2012).

Rindt, C.C.M., A.A. van Steehoven, “Unsteady flow in a rigid 3-D model of the carotid artery bifurcation,” Journal of Biomechanical Engineering **118**, 149-159 (1996).

Robertson, A.M. “Hemorheology. In: Hemodynamical Flows. Modelling, Analysis and Simulation,” Oberwolfach Seminars, Vol. **37**, 63-120. (2008)

Rosenson, R.S., S. Shott, and C.C. Tangney “Hypertriglyceridemia is associated with an elevated blood viscosity. Rosenson: triglycerides and blood viscosity,” Atherosclerosis. **161**(2), 433-439 (2

Scott, M., “The modeling of blood rheology in small vessels,” PhD Thesis, University of Waterloo, (2005).

Seo, T., “Numerical simulations of blood flow in arterial bifurcation models,” Korea-Australia Rheology Journal **25**, 153-161 (2013).

Seron, F.J., E. Garcia, and J. del Pico, “MOTRICO project - geometric construction and mesh generation of blood vessels by means of the fusion of angiograms and IVUS,” IbPRIA, 951-961 (2003).

Shi, Y., P. Lawford, and R. Hose, “Review of zero-D and 1-D models of blood flow in the cardiovascular system,” BioMedical Engineering OnLine **10**, 1-38 (2011).

Sochi, T, “Non-Newtonian rheology in blood circulation,” (2014). arXiv:1306.2067.

Soulis, J. V., G. D. Giannoglou, Y. S. Chatzizisis, K. V. Seralidou, G. E. Parcharidis, and G. E. Louridas, “Non-Newtonian models for molecular viscosity and wall shear stress in a 3D reconstructed human left coronary artery,” Med Eng Phys, **30**, 9–19 (2008)

Sousa, P. C., J. Carneiro, R. Vaz, A. Cerejo, F. T. Pinho, M. A. Alves, and M. S. N. Oliveira, ‘‘Shear viscosity and nonlinear behavior of whole blood under large amplitude oscillatory shear,’’ Biorheology **50**, 269-282 (2013).

Spilker, R.L., J.A. Feinstein, D.W. Parker, V.M. Reddy, and C.A. Taylor, “ Morphometry-Based Impedance Boundary Conditions for Patient-Specific Modeling of Blood Flow in Pulmonary Arteries,” Annals of Biomedical Engineering **35**(4), 546-559 (2007).

Stamos, T.D., R.S. Rosenson “Low high density lipoprotein levels are associated with an elevated blood viscosity,” Atherosclerosis **146**(1), 161–165 (1999).

Steinman, D.A., Thomas, J.B., H.M.Ladak, J.S. Milner, B.K. Rutt, and J.D. Spence JD, “Reconstruction of carotid bifurcation hemodynamics and wall thickness using computational fluid dynamics and MRI,” Magnetic Resonance in Medicine **47**, 149-159 (2002).

Sun, N. and D. De Kee, "Linear viscoelasticity and stress growth in blood, " Canadian Journal Of Chemical Engineering **80**, 495-498 (2002).

Sun, N., and D. De Kee, "Simple shear, hysteresis and yield stress in biofluids, " Canadian Journal Of Chemical Engineering **79**, 36 – 41 (2001).

Tanaka, N., and T. Takano, “Microscopic-scale simulation of blood flow using SPH method,” International Journal of Computational Methods **2**, 555-568 (2005).

Tang, D., C. Yang, S. Kobayashi, J. Zheng, and R. P. Vito, “Effect of stenosis asymmetry on blood flow and artery compression: a three-dimensional fluid-structure interaction model,” Annals of Biomedical Engineering **31**, 1182-1193 (2003).

Taylor, C. A., and M. T. Draney, “Experimental and computational methods in cardiovascular fluid mechanics,” Annual Review of Fluid Mechanics, **36**, 197-231 (2004).

Taylor, C.A., T.J.R. Hughes, and C.K. Zarins, “Finite element modeling of three-dimensional pulsatile flow in the abdominal aorta: Relevance to atherosclerosis,” Annals of Biomedical Engineering **26**, 975-987 (1998).

Thiriet, M., Biology and Mechanics of Blood Flows. Part I: Biology. Springer: New York (2008).

Thurston, G. B., ‘‘Effects of Frequency of Oscillatory Flow on Impedance of Rigid, Blood-Filled Tubes,’’ Biorheology **13**, 191-199 (1976).

Thurston, G. B., ‘‘Elastic Effects in Pulsatile Blood-Flow,’’ Microvascular Research **9**, 145-157 (1975).

Thurston, G.B. “Viscoelasticity of human blood,” Biophys. J. **12**,1205–1217 (1972).

Torii, R., N.B. Wood, N. Hadjiloizou, A.W. Dowsey, A.R. Wright, A.D. Hughes, J. Davies, D.P. Francis , J. Mayet, G.-Z. Yang, S.A. McG Thom, and X.Y. Xu, “Fluid–structure interaction analysis of a patient-specific right coronary artery with physiological velocity and pressure waveforms,” Commun. Numer. Meth. Engng. **25**, 565–580 (2009).

Trushar, G., R.H.P. McGregor, D. Szczerba, K. Burckhardt, K. Muralidhar, and G. Szekely “Simulation of oscillatory flow in an aortic bifurcation using FVM and FEM: A comparative study of implementation strategies,” Inter J Numer Meth Fluids **66**, 1037-1067 (2011).

Truskey, G.A., F. Yuan, and D.F. Katz, Transport Phenomena in Biological Systems, 2nd ed. Prentice Hall: Upper Saddle River, NJ (2009).

Valencia, A., A. Zarate, M. Galvez, L. Badilla, “Non-Newtonian blood flow dynamics in a right internal carotid artery with a saccular aneurism,” International Journal for Numerical Methods in Fluids **50**,751-764 (2006).

Vignon, I. E., C.A. and Taylor, “Outflow Boundary Conditions for One-Dimensional Finite Element Modeling of Blood Flow and Pressure Waves in Arteries,” Wave Motion **39**(4), 361–374 (2004).

Vignon-Clementel, I.E., C.A. Figueroa, K.E Jansen, and C.A. Taylor, “Outflow Boundary Conditions for Three-Dimensional Finite Element Modeling of Blood Flow and Pressure in Arteries,” Comput. Methods Appl. Mech. Eng. **195**(29–32), 3776–3796 (2006).

Vitkova, V., M. A. Mader, B. Polack, C. Misbah, and T. Podgorski, “Micro-Macro Link in Rheology of Erythrocyte and Vesicle Suspensions,” Biophysical Journal, **95**, L33-L35 (2008).

Waite, L., and J. Fine, *Applied Biofluid Mechanics.* McGraw Hill: New York (2007).

Wake, A.K., J.N. Oshinski, A.R. Tannenbaum, and D.P. Giddens, “Choice of In Vivo Versus Idealized Velocity Boundary Conditions Influences Physiologically Relevant Flow Patterns in a Subject-Specific Simulation of Flow in the Human Carotid Bifurcation,” Journal of Biomechanical Engineering **131**(2), 021013 (2009).

Walburn, F.J., and D.J. Schneck “A constitutive equation for whole human blood,” Biorheology **13**, 201–210 (1976).

Walwander, W. P., T. Y. Chen, and D. F. Cala, “An approximate Casson fluid model for tube flow of blood,” Biorheology **12**, 111-119 (1975).

Wang, S.Z., J.L. Chen, G.H. Ding, G. Lu, X.L. Zhang, “Non-Newtonian computational hemodynamics in two patient-specific cerebral aneurysms with daughter saccules,” J. Hydrodynamics **22**, 639-646 (2010).

Weng, X., G. Cloutier, R. Beaulieu, and G. O. Roederer, “Influence of acute-phase proteins on erythrocyte aggregation,” Am. J. Physiol. **271**, H2346-H2352, 1996.

Wentzel, J. J., Y. S. Chatzizisis, F. J. Gijsen FJ, G. D. Giannoglou, C. L. Feldman, and P. H. Stone, “Endothelial shear stress in the evolution of coronary atherosclerotic plaque and vascular remodelling: current understanding and remaining questions,” Cardiovasc. Res. **96**, 234–243 (2012).

Wooten, D.M., and D.N. Ku, “Fluid mechanics of vascular systems, diseases and thrombosis,” Annual Review of Biomedical Engineering **1**, 299-329 (1999).

Xu, X.Y., Q. Long, M.W. Collins, M. Bourne, and T.M. Griffith TM, “Reconstruction of blood flow patterns in human arteries,” Proc. Instn Mech. Engrs **213**, Part H: 411-421 (1999).

Yeleswarapu, K. K., "Evaluation of continuum models for characterizing the constitutive behavior of blood," Ph.D. Thesis, University of Pittsburgh (1996).

Yeow, Y. L., S. R. Wickramasinghe, Y. K. Leing, and B. Han, “Model-independent relationships between hematocrit, blood viscosity and yield stress derived from Couette viscometry data,” Biotechnol. Prog. **18**, 1068-1075 (2002).

Yilmaz F., and M. Y. Gundogdu, “A critical review on blood flow in large arteries; relevance to blood rheology, viscosity models, and physiologic conditions,” Korea-Australia Rheology Journal **20**, 197-211 (2008).

Younis, H.F., M.R. Kaazempur-Mofrad, R.C. Chan, A.G. Isasi, D.P. Hinton, A.H. Chan, L.A. Kim, and R.D. Kamm, “Hemodynamics and wall mechanisms in human carotid artery bifurcation and its consequences for atherogenesis: Investigation of inter-individual variation,” Biomechanics and Modeling in Mechanobiology **3**(1), 17-32 (2004).

Zamir, M., *The Physics of Coronary Blood Flow*. AIP Press, Springer-Verlag: New York (2005).

Zamir, M., *The Physics of Pulsatile Flow*. AIP Press, Springer-Verlag: New York (2000).

Zydney, A. L., J. D. Oliver, and C. K. Colton, “A constitutive equation for the viscosity of stored red cell suspensions: Effect of hematocrit, shear rate, and suspending phase,” Journal of Rheology **35**, 1639-1679 (1991).

Appendix A

EVALUATING THE STEADY STATE SOLUTION OF THE PROPOSED THIXOTROPIC MODEL

A.1 Proving that the thixtropic model reduces to the Casson under steady state

We want to evaluate the steady state stress, τ_s, for a given shear rate, $\dot{\gamma}_s$. Throughout the analysis that is presented in the Appendix, we will be using the subscript "s" to denote steady state conditions.

From Eq. (4.15), the stress prediction of the thixotropic model under steady state is given by:

$$\tau_s = G_s \gamma_{e_s} + \mu \dot{\gamma}_{p_s} \tag{A.1}$$

where G_s is the elastic modulus, γ_{e_s} the elastic strain, μ the model viscosity and $\dot{\gamma}_{p_s}$ the plastic shear rate, all evaluated at steady state.

Under steady state conditions the elastic strain, γ_{e_s}, reaches its maximum value, that of the critical strain, γ_{max_s}:

$$\gamma_{e_s} = \gamma_{max_s} \tag{A.2}$$

Thus, based on Eq. (12), the model predicts that the elastic shear rate is zero, and then based on Eq. (11) we conclude that, under steady state conditions, the shear rate, $\dot{\gamma}_s$, is equal to the plastic shear rate, $\dot{\gamma}_{p_s}$:

$$\dot{\gamma}_{p_s} = \dot{\gamma}_s \tag{A.3}$$

The steady state solution (i.e. $\frac{d}{dt}\lambda_s = 0$) of the structural equation, Eq. (19), yields:

$$\lambda_s = \frac{1}{\sqrt{\frac{4\mu\dot{\gamma}_s}{\tau_0} + 1}}\,, \tag{A.4}$$

while from the modulus evolution equation, Eq. (16), we get:

$$G_s = G_{e_s}\,, \tag{A.5}$$

where G_{e_s} is the steady state equilibrium value of the modulus given by (see Eq. (18)):

$$G_{e_s} = \lambda_s G_0\,. \tag{A.6}$$

Thus, by combining Eq. (A4) - Eq. (A6) we get:

$$G_s = \lambda_s G_0 = \frac{1}{\sqrt{\frac{4\mu\dot{\gamma}_s}{\tau_0} + 1}} G_0\,. \tag{A.7}$$

The last piece of information needed to obtain the steady state predictions of the thixotropic model is the critical strain value. Based on Eq. (13), we need to examine two cases:

i. If $\frac{\gamma_0}{\lambda^2} \le \gamma_\infty \Rightarrow$

$$\gamma_{max_s} = \frac{\gamma_0}{\lambda_s^{\,2}} = \frac{\gamma_0}{\frac{1}{\left(\sqrt{\frac{4\mu\dot{\gamma}_s}{\tau_0}}+1\right)^2}} \tag{A.8}$$

Then, combining Eq. (A1)- (A3), and Eq. (A7)-(A8) we get:

$$\tau_s = \frac{1}{\sqrt{\frac{4\mu\dot{\gamma}_s}{\tau_0}}+1} G_0 \frac{\gamma_0}{\frac{1}{\left(\sqrt{\frac{4\mu\dot{\gamma}_s}{\tau_0}}+1\right)^2}} + \mu\dot{\gamma}_s = \left(\sqrt{\frac{4\mu\dot{\gamma}_s}{\tau_0}}+1\right) G_0\gamma_0 + \mu\dot{\gamma}_s \overset{G_0\gamma_0=\tau_0}{\Leftrightarrow}$$

$$\tau_s = \tau_0 + 2\mu^{1/2}\dot{\gamma}_s^{\,1/2}\tau_0^{\,1/2} + \mu\dot{\gamma}_s \;\Leftrightarrow\; \tau_s^{\,1/2} = \tau_0^{\,1/2} + \mu^{1/2}\dot{\gamma}_s^{\,1/2}. \text{ Casson Eq.} \tag{A9}$$

ii. If $\frac{\gamma_0}{\lambda^2} > \gamma_\infty \Rightarrow \gamma_{max_s} = \gamma_\infty$

Similarly, combining the information from the respective equations, Eq. (A.1)-(A.3) and Eq. (A.7)-(A.8), we get in this case:

$$\tau_s = \frac{1}{\sqrt{\frac{4\mu\dot{\gamma}_s}{\tau_0}+1}} G_0\gamma_\infty + \mu\dot{\gamma}_s = \frac{G_0\gamma_0}{\sqrt{\frac{4\mu\dot{\gamma}_s}{\tau_0}+1}} \frac{\gamma_\infty}{\gamma_0} + \mu\dot{\gamma}_s \overset{G_0\gamma_0=\tau_0}{\Leftrightarrow}$$

$$\tau_s = \frac{\tau_0}{\sqrt{\frac{4\mu\dot{\gamma}_s}{\tau_0}+1}} \frac{\gamma_\infty}{\gamma_0} + \mu\dot{\gamma}_s \tag{A.10}$$

Eq. (A.9) and (A.10) can be collectively represented to give the steady state predictions of the thixotropic model as:

$$\sqrt{\tau_s} = \begin{cases} \sqrt{\tau_0} + \sqrt{\mu}\sqrt{\dot{\gamma}_s}\,; & \sqrt{\frac{4\mu\dot{\gamma}_s}{\tau_0}} \le \sqrt{\frac{\gamma_\infty}{\gamma_0}} - 1 \\ \sqrt{\left(\frac{\tau_0}{\sqrt{\frac{4\mu\dot{\gamma}_s}{\tau_0}+1}} \frac{\gamma_\infty}{\gamma_0} + \mu\dot{\gamma}_s\right)}\,; & \sqrt{\frac{4\mu\dot{\gamma}_s}{\tau_0}} > \sqrt{\frac{\gamma_\infty}{\gamma_0}} - 1 \end{cases} \tag{A11}$$

Appendix B

DEVELOPMENT OF SIMULANT MODEL FOR THE PATHOLOGICAL LEFT CORONARY ARTERY (LCA)

B.1 Summary

Appendix A summarizes the development and application of the simulant model for the pathological geometry examined in Chapter 5 (blockage in LAD artery, causing an 82% occlusion). The geometrical analysis required for the development of the simulant model, as well as the Matlab code wherein the model is implemented, are presented.

B.2 Methodology

Following the description of Section 5.2.3.1, the development of the simulant model for the pathological geometry requires that the pressure differential along the occluded artery, LAD, be determined by:

$$P_{j,2} - P_{j,1} = -\frac{8\mu Q_j(t)}{\pi}\left[\int_{0}^{stenosis,downstream} \frac{dz}{\left(R_j(z)\right)^4} + \int_{sten.,downstr}^{sten.,upstr} \frac{dz}{\left(R_{hyd,j}(z)\right)^4} + \int_{sten.,upstr}^{L_j} \frac{dz}{\left(R_j(z)\right)^4}\right] \quad \text{(B.1)}$$

The complexity rises from the calculation of the second integral on the right hand side of Eq. (B.1). The particular term denotes the pressure drop along the stenosis site and requires, due to the irregular shape that results from the stenosis development, the calculation of a hydraulic radius. This radius is used to estimate the unobstructed area. Both the hydraulic radius and the level of occlusion are dependent

on the position along the LAD centerline. Fig. B.1 demonstrates the geometry of the particular problem.

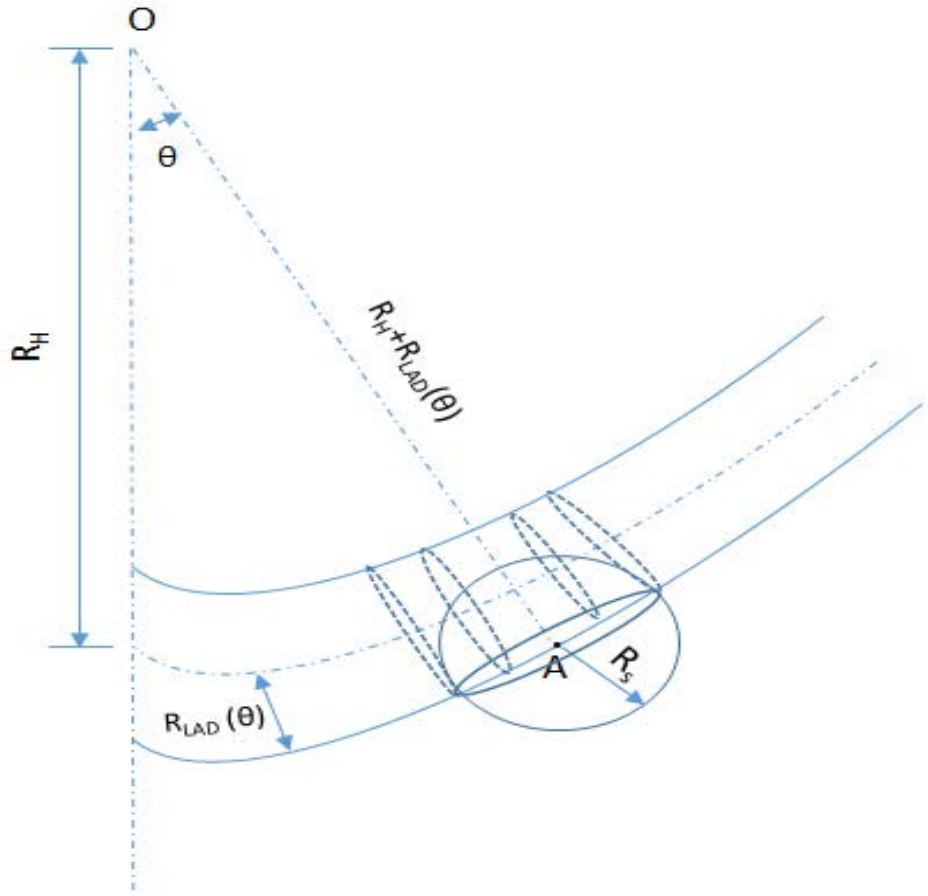

Figure B.1: Geometrical representation of the pathological LAD artery. The stenosis is modeled as a sphere of radius R_S. R_{LAD}, the local radius of the LAD (dotted circles), decreases from left to right due to the tapering of the vessel, while RH, the radius of the heart, is constant. A is the center of the stenosis-sphere and O is the origin.

In order to facilitate our calculations of the hydraulic radius and the obstructed area, we need to consider the intersections between the local LAD cross-sections

(dotted circles in Fig. B.1) and the stenosis sphere, for incremental changes of the angle θ that occur within the length of the lower branch of the LAD artery that is span from the stenosis. The geometrical information required for this analysis, such as lengths and angles, are shown in Fig. B.2, where we consider an arbitrary intersection between the stenosis-sphere and one of the LAD cross-sections.

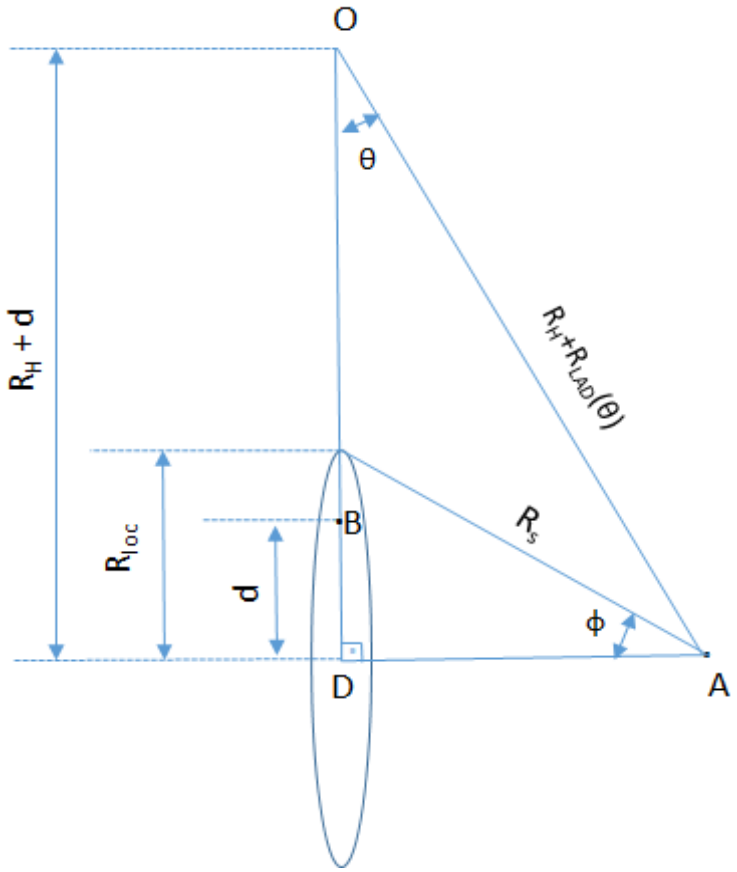

Figure B.2: Geometrical analysis of the intersection between a random LAD cross-section and the stenosis. Rloc is the radius of the projected stenosis sphere on the arbitrary LAD cross-section. Points A and D are the centers of the stenosis sphere and the projected sphere, respectively. Point B lies on the LAD centerline.

From the illustration of Fig. B.2, the main geometrical lengths of interest are the radii R_{loc}, R_{LAD}, and the distance d. Based on these three parameters, a list of all possible intersection configurations that could emerge, as we integrate from the beginning to the end of the stenosis site, has been constructed. The logical diagram that accounts for all configurations is shown in Fig. B.3.

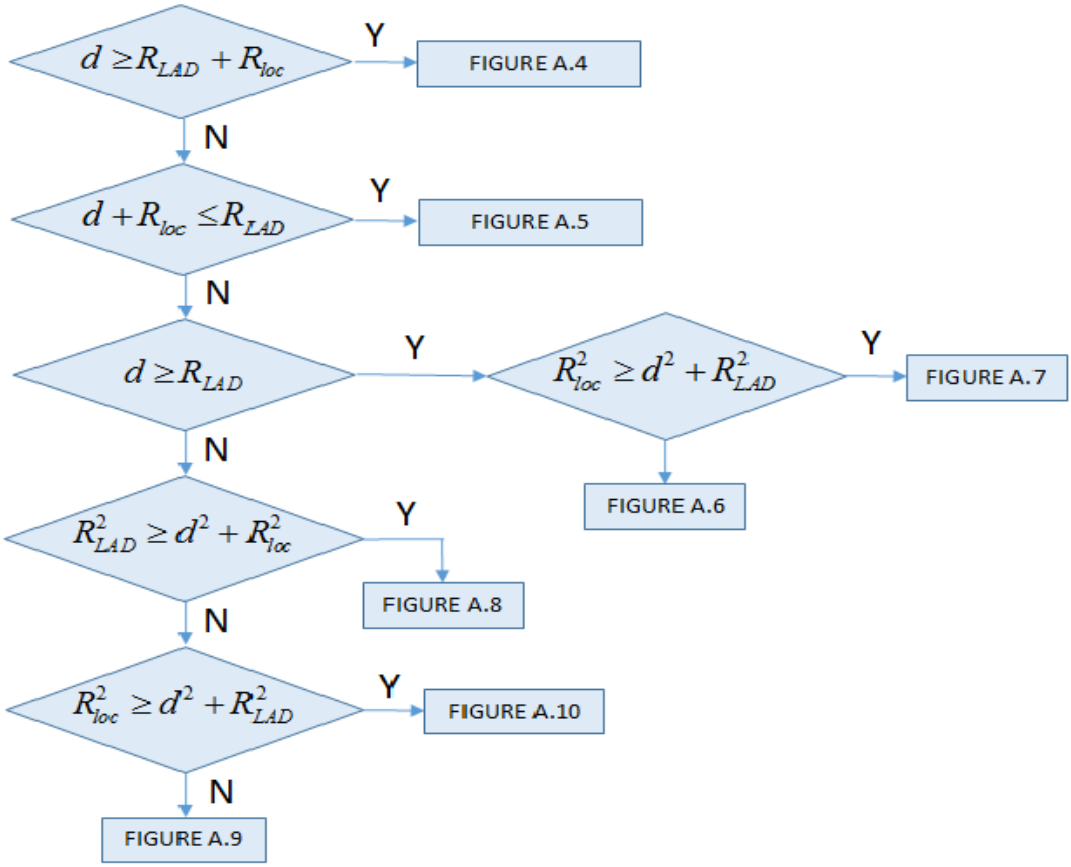

Figure B.3: Logical diagram accounting for all possible configurations of the stenosis-sphere projection on the local LAD cross-section.

The different configurations, corresponding to the algorithm of Fig. B.3, are shown in Figs. B.3-B.9.

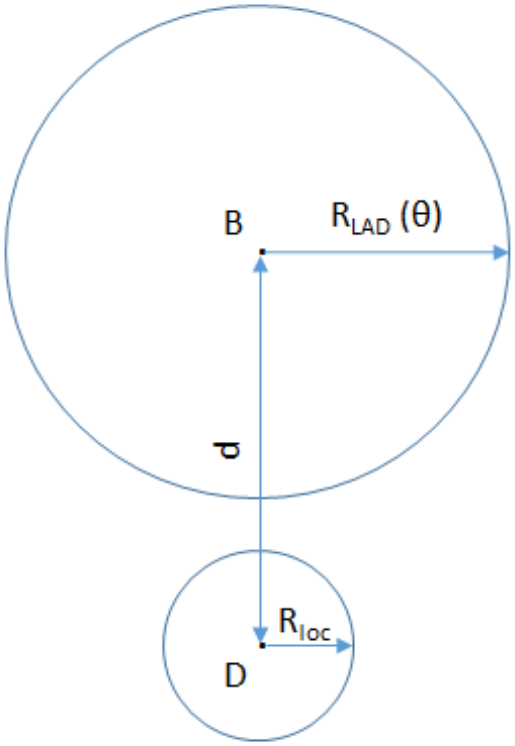

Figure B.4

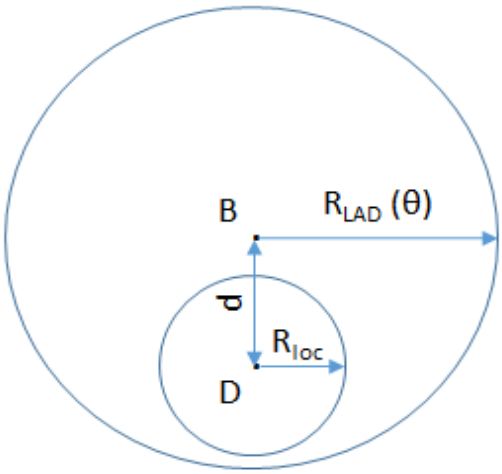

Figure B.5

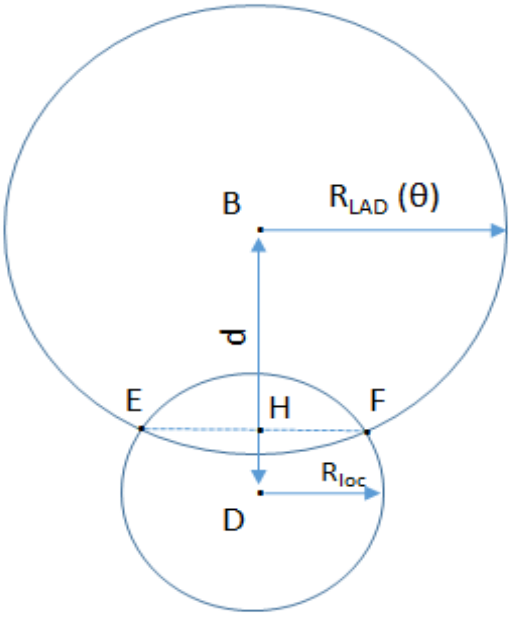

Figure B.6

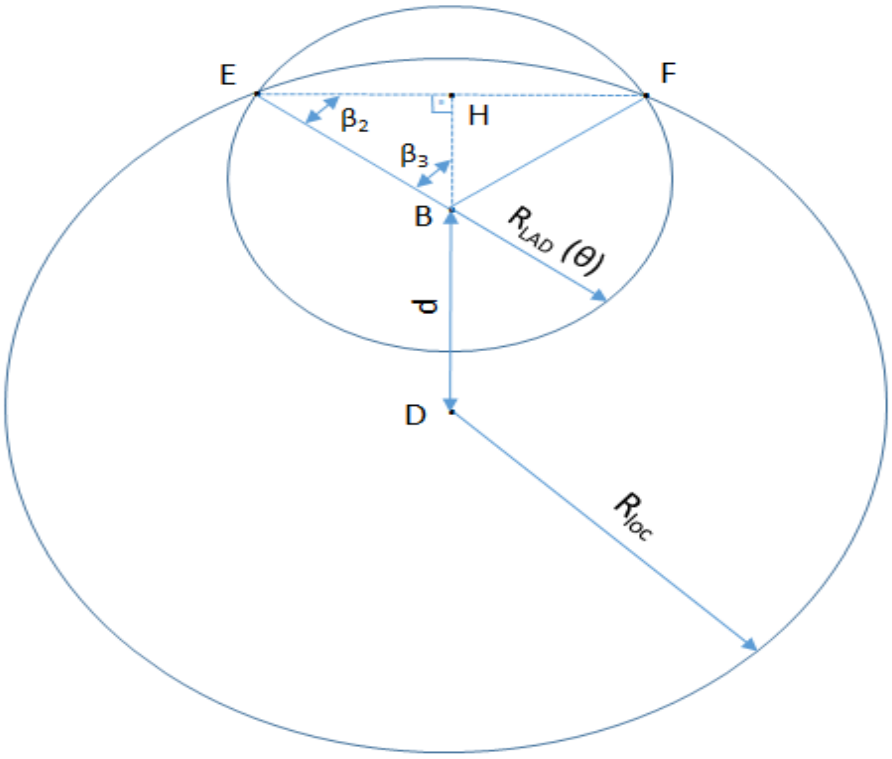

Figure B.7

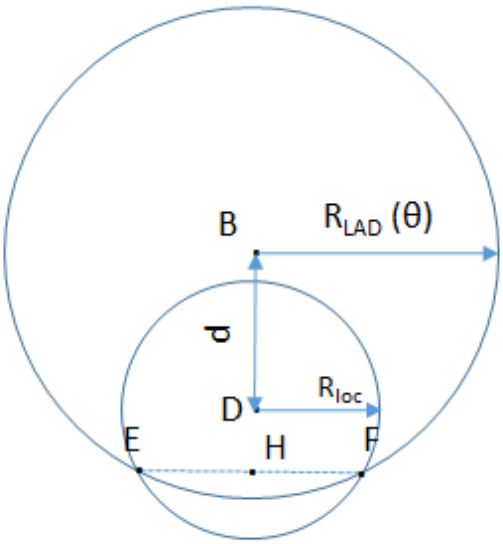

Figure B.8

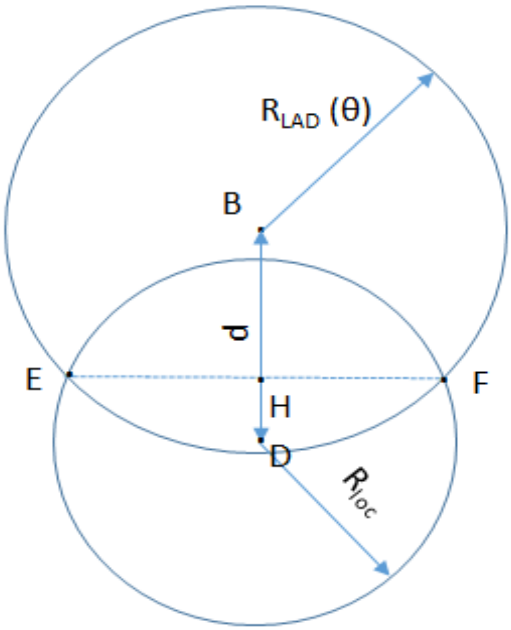

Figure B.9

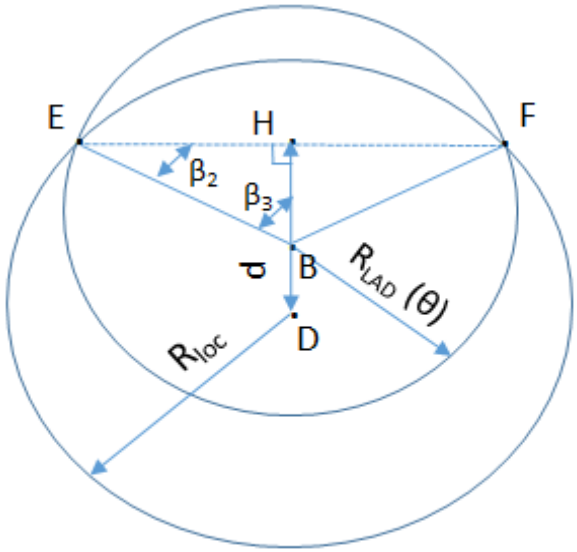

Figure B.10

B.3 Matlab implementation

```
function
[R_Hydr,R_LAD_local,R_loc,OD,lamda,Area_of_flow,Wet_Perimeter,DH,EH,
        EH2,theta,m,H,phi,beta,beta2,beta3,gamma,BH] = ...
        Hydraulic_Diameter_Stenosis(m,R,R_s)

    % This function yields the hydraulic diameter (and therefore
the area % of  flow) for every incremental change in the angle theta
```

```
(which is % directly related to the coefficient m that was used in
ICEMANSYS to % build the mesh geometry).  The code accounts for all
possible      % configurations of the projected stenosis-sphere on
the local LAD     % cross-section.
      %


      for i=1:length(m)
          R_LAD_local(i)=(1.85*0.93^m(i))/1000; % [m]
          theta(i)=abs((pi/2.*3/16)-(pi/2.*m(i)/16));
          H(i)=(sin(theta(i))).*(R+((1.85*0.93.^3)/1000)); % H =
distance     between points A & D
          if H(i)>R_s
              H(i)=R_s;
          end
          phi(i)=acos(H(i)/R_s);
          R_loc(i)=sin(phi(i))*R_s;
          OD(i)=cos(theta(i))*(R+((1.85*0.93.^3)/1000));
          lamda(i)=OD(i)-R;
          if (R_loc(i)^2+lamda(i)^2)-R_LAD_local(i)^2<0
              DH(i)=(R_LAD_local(i)^2-R_loc(i)^2-
lamda(i)^2)/2/lamda(i);
          else
              DH(i)=(R_loc(i)^2-
R_LAD_local(i)^2+lamda(i)^2)/(2*lamda(i));
          end
              if lamda(i)> R_loc(i)+R_LAD_local(i)  % No
instersection
                  % Case 1: No intersection between sphere projection
and
                  % local LAD circle
                  count2=count2+1;
                  BH(i)=0;
                  EH(i)=0;
                  DH(i)=0;
```

```
                Area_of_flow(i)=0;
                Wet_Perimeter(i)=0;
                R_Hydr(i)=0;
            else
                if lamda(i)+R_loc(i)<=R_LAD_local(i)
                    % Case 2: All of the sphere projection in LAD
circle
                    BH(i)=0;
                    EH(i)=0;
                    DH(i)=0;
                    Wet_Perimeter(i)=2*pi*(R_LAD_local(i));
                    Area_of_flow(i)=pi*(R_LAD_local(i)^2-
R_loc(i)^2);
                    R_Hydr(i)=2*Area_of_flow(i)/Wet_Perimeter(i);
                else
                    if lamda(i)>=R_LAD_local(i)
                        if R_loc(i)^2 >=
lamda(i)^2+R_LAD_local(i)^2
                            % Case 4: Chord EF above B & D
                            BH(i)=(DH(i)-lamda(i));
                            EH(i)=sqrt((R_LAD_local(i)^2-
(BH(i))^2));
                            EH2(i)=sqrt(R_loc(i)^2-DH(i)^2);
                            gamma(i)=asin(EH(i)/R_loc(i));
                            beta2(i)=asin(BH(i)/R_LAD_local(i));
                            beta3(i)=pi-pi/2-beta2(i);
                            beta(i)=pi-beta3(i);
                            Area_of_flow(i)=pi*R_LAD_local(i)^2-
beta(i)*R_LAD_local(i)^2-(gamma(i)*R_loc(i)^2-EH(i)*DH(i))-
EH(i)*BH(i);

Wet_Perimeter(i)=2*R_LAD_local(i)*beta3(i)+2*R_loc(i)*gamma(i);

R_Hydr(i)=2*Area_of_flow(i)/Wet_Perimeter(i);
                        else
```

```
                                % Case 3: Chord EF between B & D
                                BH(i)=(lamda(i)-DH(i));
                                EH(i)=sqrt((R_LAD_local(i)^2-
(BH(i))^2));
                                beta(i)=asin(EH(i)/R_LAD_local(i));
                                gamma(i)=asin(EH(i)/R_loc(i));
                                Area_of_flow(i)=pi*R_LAD_local(i)^2-
(gamma(i)*R_loc(i)^2-EH(i)*DH(i))-beta(i)*R_LAD_local(i)^2-
EH(i)*BH(i));
                                Wet_Perimeter(i)=2*R_LAD_local(i)*(pi-
beta(i))+2*R_loc(i)*(gamma(i));

R_Hydr(i)=2*Area_of_flow(i)/Wet_Perimeter(i);
                            end
                        else
                            if R_LAD_local(i)^2 >=
R_loc(i)^2+lamda(i)^2
                                % Case 5: Chord EF below B & D
                                DH(i)=(R_LAD_local(i)^2-R_loc(i)^2-
lamda(i)^2)/2/lamda(i);
                                DH(i)=(R_LAD_local(i)^2-R_loc(i)^2-
lamda(i)^2)/2/lamda(i);
                                BH(i)=lamda(i)+DH(i);
                                EH(i)=sqrt((R_LAD_local(i)^2-BH(i)^2));
                                beta(i)=asin(EH(i)/R_LAD_local(i));
                                gamma(i)=asin(EH(i)/R_loc(i));
                                Wet_Perimeter(i)=2*(pi-
beta(i))*R_LAD_local(i)+2*(pi-gamma(i))*R_loc(i);
                                Area_of_flow(i)=pi*R_LAD_local(i)^2-
(pi*R_loc(i)^2-(gamma(i)*R_loc(i)^2-EH(i)*DH(i)-
(beta(i)*R_LAD_local(i)^2-EH(i)*BH(i))));

R_Hydr(i)=2*Area_of_flow(i)/Wet_Perimeter(i);
                            else
```

```
                            if R_loc(i)^2 >=
lamda(i)^2+R_LAD_local(i)^2
                                % Case 7: Chord EF above B & D
                                BH(i)=(DH(i)-lamda(i));
                                EH(i)=sqrt((R_LAD_local(i)^2-
(BH(i))^2));
                                EH2(i)=sqrt(R_loc(i)^2-DH(i)^2);
                                gamma(i)=asin(EH(i)/R_loc(i));

beta2(i)=asin(BH(i)/R_LAD_local(i));
                                beta3(i)=pi-pi/2-beta2(i);
                                beta(i)=pi-beta3(i);

Area_of_flow(i)=pi*R_LAD_local(i)^2-beta(i)*R_LAD_local(i)^2-
(gamma(i)*R_loc(i)^2-EH(i)*DH(i))-EH(i)*BH(i);

Wet_Perimeter(i)=2*R_LAD_local(i)*beta3(i)+2*R_loc(i)*gamma(i);

R_Hydr(i)=2*Area_of_flow(i)/Wet_Perimeter(i);
                            else
                                % Case 6: D inside LAD circle,
chord EF between B & D
                                BH(i)=(lamda(i)-DH(i));
                                EH(i)=sqrt((R_LAD_local(i)^2-
(BH(i))^2));
                                beta(i)=asin(EH(i)/R_LAD_local(i));
                                gamma(i)=asin(EH(i)/R_loc(i));

Area_of_flow(i)=pi*R_LAD_local(i)^2-(gamma(i)*R_loc(i)^2-
EH(i)*DH(i))-(beta(i)*R_LAD_local(i)^2-EH(i)*BH(i));

Wet_Perimeter(i)=2*R_LAD_local(i)*(pi-beta(i))+2*R_loc(i)*(gamma(i));
                        R_Hydr(i)=2*Area_of_flow(i)/Wet_Perimeter(i);
                            end
                        end
```

```
                    end
                end
            end
        end
```